5-2007

Numerical and Physical Modeling of Turbulent Shear Flows

John Raiford
Clemson University, raiford@clemson.edu

NUMERICAL AND PHYSICAL MODELING OF TURBULENT SHEAR FLOWS

A Dissertation
Presented to
the Graduate School of
Clemson University

In Partial Fulfillment
of the Requirements for the Degree
Doctor of Philosophy
Civil Engineering

---

by
John Phillip Raiford
May 2007

Accepted by:
Abdul A. Khan, Committee Chair
Nadim M. Aziz
Benjaman L. Sill
Firat Y. Testik

ABSTRACT

This dissertation is an evaluation of popular turbulence schemes; both three dimensional and depth-averaged, and also includes an experimental study on shallow near bed jets. The three dimensional $k-\varepsilon$ and RNG turbulent closure schemes are evaluated for free and bounded shear flows. For free shear flows (circular and plane turbulent jets), the $k-\varepsilon$ scheme with standard coefficient performs equally well and in some cases better than the renormalized group $k-\varepsilon$ scheme in predicting growth rate, decay of centerline velocity and longitudinal velocity profiles. For turbulent kinetic energy across the jet, the inner region is better predicted by the RNG scheme.

The second case used to evaluate the three dimensional schemes was a submerged hydraulic jump. This flow included a free surface and solid boundary creating larger shearing forces than in a free jet. The results showed the longitudinal velocity profiles and their maximum values, in vertical direction, were estimated better by the RNG scheme. The turbulent kinetic energy was overestimated in both magnitude and elevation of its maximum position in the flow. The elevation of the recirculation region was also over predicted by both schemes; however, its longitudinal extent was predicted well.

A two-dimensional, depth-averaged flow model with the depth-averaged parabolic eddy viscosity, mixing length, and $k-\varepsilon$ turbulent closure schemes was used to simulate flow patterns downstream of lock and dam structures. The

mixing length scheme was modified and performed as well as the $k-\varepsilon$ scheme in predicting the location and size of the recirculation zones, as well as the velocity profiles across the channel.

Experimental measurements on shallow near bed jets are performed. For low submergence, the horizontal growth rates have two distinct regions, with the downstream region having a higher growth rate. The longitudinal velocity profiles in the horizontal plane are self-similar. The centerline decay was slower than that of a free jet.

ACKNOWLEDGMENTS

The author would like to thank the Dean's Graduate Scholars Award Committee for their financial support without which the research would not have been possible.

In addition the author would like to acknowledge Dr. Abdul Khan for his mentoring and guidance. Soon to be Dr. David N. Powell for his assistance in data collection and solving the many challenges that arose during the experimental portion of this research, and finally all of the people who brought me food and company during the weeks and weeks of data collection. Danny Metz and Scott Kauffman also deserve acknowledgment for their assistance in constructing the physical model.

TABLE OF CONTENTS

Table of Contents (Continued)

LIST OF TABLES

LIST OF FIGURES

List of Figures (Continued)

List of Figures (Continued)

Figure Page

List of Figures (Continued)

List of Figures (Continued)

CHAPTER 1
INTRODUCTION

Shear flows are one of the most common classes of fluid flows. A wide range of applications and phenomena can be classified as a shear flow and ranges from a submerged hydraulic jump, smoke plume rise, to the behavior of jet engine exhaust over a runway. A shear flow occurs when a fluid is released with some relative initial momentum or buoyancy into an ambient fluid. The released fluid creates a shear layer causing the ambient fluid to be entrained and mixed with the released flow. The most studied example of this is a free turbulent jet.

A free turbulent jet occurs when a fluid is released into a stagnant ambient fluid of infinite extent. This type of shear flow has many interesting properties such as self similarity of velocity and concentration profiles as well as conservation of momentum. While analytical solutions may exist for free shear flows, very few bounded shear flows have analytical solutions and one must rely on physical or numerical models to determine their behavior. Since most shear flows are turbulent, the choice of a turbulence scheme is integral to the accuracy of the numerical simulation.

Turbulence schemes simulate the effects of turbulence on the mean flow. These turbulence schemes provide the extra equations needed to close the Reynolds-averaged Navier-Stokes system of equations. Most of these models are semi-empirical and require determination of coefficients for a particular flow situation. Through a large number of control tests, standard values for these

coefficients are established by the ASCE Task Committee on Turbulence Modeling in Hydraulic Computations (1988). This research is an evaluation of how a few of the most popular turbulence closure schemes behave using a set of standard coefficients. Also included are the new results of an experimental study on a confined shear flow, specifically a shallow near bed jet.

Two of the most popular turbulence schemes are the $k-\varepsilon$ and RNG $k-\varepsilon$ schemes. An evaluation of their performance when modeling different flow geometries and conditions can highlight what specific aspects of shear flows they capture well when using standard coefficient values. Two well documented shear flows are used to evaluate the three dimensional forms of the standard $k-\varepsilon$ and RNG schemes in this research. The first shear flow is that of a free turbulent jet. A free turbulent jet is free of any boundaries and therefore the schemes only have to deal with fluid shear. Two nozzle geometries, plane and circular, are used. Well documented experimental and analytical solutions exist for both these geometries to provide a solid basis for comparison between the two closure schemes. Results from both the schemes are compared to longitudinal and transverse velocity profiles, centerline velocity decay, growth rate, and turbulent kinetic energy profiles for both nozzle geometries.

The second flow geometry used in this research is a submerged hydraulic jump. In this shear flow geometry, not only is a large recirculation region produced but a free surface and solid boundary are also present. Submerged hydraulic jumps dissipate a large amount of energy over a short distance through a higher level of turbulence than is seen in the free jet cases.

The data used to evaluate the performance of the two turbulence schemes is taken from the extensive experiments of a submerged hydraulic jump performed by Long (1991). The experimental results for velocity profiles of both the longitudinal and vertical velocities are compared to the results from the two turbulence schemes at different locations along the jump. Comparisons of water surface profiles and turbulent kinetic energy profiles are also made.

In many situations when modeling large rivers, a two-dimensional depth-averaged model is employed. These models use various depth-averaged turbulence closure schemes to predict the flow behavior. One such flow situation is that downstream of a lock and dam. When the power house releases water to generate electricity, the lock on the other side of the channel is affected by a large recirculation zone created by the shearing effects of the power house flow release. This shear flow is bounded and takes up the full depth of the channel making a depth-averaged model appropriate. The turbulence schemes under consideration in this research are the parabolic eddy viscosity scheme, mixing length scheme, and depth-averaged $k-\varepsilon$ scheme. Modifications are made to the mixing length scheme to improve its performance. The different turbulent closure schemes are evaluated using the measured data for velocity profiles, eddy size, and eddy location taken by Bravo (1990). The validated model is then applied to a case study using data obtained at the J.H. Overton Dam on the Red River, Louisiana.

Another type of shear flow which shares some commonalities with the submerged hydraulic jump is a shallow near bed jet. The hydraulic jump has been modeled as a limiting case of this type of jet for the plane nozzle geometry, as the

nozzle is adjacent to the floor. Submerged hydraulic jumps have even been modeled as a plane jet under an adverse pressure gradient (Rajaratnam, 1965). In this research experiments are conducted with a circular jet entering a shallow ambient fluid. The jet issues from a circular nozzle above a flat plate. The jet nozzle submergence and height off the floor are equal. At each floor/submergence level three flow rates are used. Longitudinal velocity profiles in the horizontal and vertical directions are taken along the planes of local maximum velocity for x/d locations from 6 to 50 using a pitot tube, where x is the distance from the nozzle in the downstream direction and d is the nozzle diameter (0.5 inch). Horizontal profiles are examined for self similarity, growth rate and velocity decay. Vertical profiles are fit to a power law near the bed, and the free surface is modeled as a plane of symmetry using a modified Reichardt's hypothesis. Surface disturbances are evaluated qualitatively from photographs of the wave field.

One objective of this research is to evaluate the behavior of popular turbulence closure schemes, both three dimensional and depth averaged, using standard coefficient values by comparing their results to well documented shear flows that introduce the models to both fluid shearing and shearing forces produced in the presence of free surface and wall boundaries. Another objective is to evaluate the modifications made to the mixing length scheme, and finally to analyze the data obtained from experiments with a shallow near bed jet using circular nozzle geometry. By examining the performance of turbulence schemes

and making improvements upon them, it may become possible to decide whether the standard schemes will be sufficient, saving the time and cost of a physical model. Also the experimental results may provide future researchers with the data to evaluate these and other turbulence schemes.

CHAPTER 2
NUMERICAL SIMULATION OF FREE TURBULENT JETS

Turbulent jets are the primary means through which waste is discharged into the environment. The performance of a jet in these circumstances relies on the orifice geometry, characteristics of the discharged and ambient fluid, and the physical environment into which a jet is discharged. A jet is considered free when any boundaries are far enough away that any effects they have on the jet are insignificant. Classical self-similar solutions of free jet flow are based on three assumptions. These assumption are (1) that the jet is slender, dividing the flow into two regions, the jet mixing layer and the flow induced by entrainment, (2) the initial velocity is maintained for a large distance away from the jet compared to the exit diameter or height (in the potential core) so that the flow (in the ZEF) depends only on the kinematic momentum flux and (3) the momentum flux inside the jet is conserved (Schneider, 1985).

The velocity profiles at different sections along the jet for both plane and circular jets are self similar when normalized by the appropriate velocity and length scales. Two classical solutions for the velocity profiles in free plane jets are the Tollmien solution and Goertler's solution. The Tollmien solution uses Prandtl's mixing length equation to solve the equations of motion for a plane turbulent jet. Goertler's solution assumes a constant eddy viscosity exchange coefficient across the flow (Rajaratnam, 1976). Experimental observations, made by Heskestad (1965) and Albertson (1950), for plane turbulent jets observed that

the Tollmien solution is preferred in the outer region of the jet where as the Goertler solution provides better approximation near the centerline of the jet. Similar solutions can be applied to circular turbulent jets with similar preference given to each solution in the inner and outer regions (Wygnanski and Fiedler, 1969).

In most cases, the jet interacts with solid boundaries and/or a free surface for which analytical or empirical solutions may not be available. In such cases, either physical model or numerical model studies are relied upon. In recent years, numerical models have been increasingly adopted for studying complicated flow scenarios. In modeling turbulent flows, one of the key elements is the choice of a turbulent closure scheme. The $k-\varepsilon$ and the Renormalized Group $k-\varepsilon$ (RNG) schemes are the two most popular schemes. While both these models can provide accurate results, their accuracy depends on empirical coefficients which must be adjusted to calibrate these schemes. For example, the standard coefficients of the $k-\varepsilon$ scheme were determined by computer optimization of laboratory shear flows (ASCE Task Committee on Turbulence Models in Hydraulic Computations, 1988).

The standard coefficients determined for the turbulent closure schemes are not universal. Corrections to these coefficients have been established for different flows to achieve better agreement with the laboratory or analytical results. For example, the standard coefficients are modified to simulate circular turbulent jets and achieve better accuracy with established results (ASCE Task Committee on Turbulence Models in Hydraulic Computations, 1988). However, in cases where

the jets may interact with boundaries, surface, or other flows, the appropriate modifications may not be available and standard values of these coefficients may have to be used.

Mathematical Details

The three-dimensional Reynolds-averaged Navier-Stokes equations representing mass and momentum equations for turbulent flows are given by

$$\frac{\partial U_i}{\partial x_i} = 0 \tag{2.1}$$

$$\frac{\partial U_i}{\partial t} + U_j \frac{\partial U_i}{\partial x_j} = -\frac{1}{\rho}\frac{\partial P}{\partial x_i} + \frac{\partial}{\partial x_j}\left[\nu \frac{\partial U_i}{\partial x_j} - \overline{u_i u_j}\right] \tag{2.2}$$

where i and j are indices representing x, y, z directions in the Cartesian coordinates, x_i represents coordinate directions ($i = 1$ to 3 for x, y, z directions, respectively), U_i is the time-averaged velocity component, t represents time, ρ is the fluid density, P is the piezometric pressure, ν is the kinematic viscosity of the fluid, and $\overline{u_i u_j}$ represent turbulent normal and shear stresses. Turbulent closure schemes are required to model turbulent normal and shear stresses.

The $k-\varepsilon$ and the RNG turbulent closure schemes use Boussinesq's eddy viscosity assumption to relate turbulent normal and shear stresses to the mean flow velocity gradients as follows

$$-\overline{u_i u_j} = \nu_t\left(\frac{\partial U_i}{\partial x_j} + \frac{\partial U_j}{\partial x_i}\right) - \frac{2}{3}k\delta_{ij} \tag{2.3}$$

where ν_t is the turbulent eddy viscosity, δ_{ij} is the Kronecker delta, and $k\left(=0.5\overline{u_i u_i}\right)$ is the turbulent kinetic energy per unit mass. The turbulent eddy viscosity is computed as

$$\nu_t = c_\mu \frac{k^2}{\varepsilon} \tag{2.4}$$

where c_μ is an empirical coefficient and ε is the dissipation rate per unit mass of turbulent energy. The $k-\varepsilon$ and RNG turbulent closure schemes use the above equation to determine turbulent eddy viscosity which relates the turbulent shear and normal stresses to the time averaged velocity gradients. To close the system, transport equations for k and ε are needed.

In case of standard $k-\varepsilon$ turbulent closure scheme, the transport equations for kinetic energy and dissipation rate per unit mass are given by

$$\frac{\partial k}{\partial t} + U_i \frac{\partial k}{\partial x_i} = \frac{\partial}{\partial x_i}\left(\frac{\nu_t}{\sigma_k}\frac{\partial k}{\partial x_i}\right) + \nu_t\left(\frac{\partial U_i}{\partial x_j} + \frac{\partial U_j}{\partial x_i}\right)\frac{\partial U_i}{\partial x_j} - \varepsilon \tag{2.5}$$

$$\frac{\partial \varepsilon}{\partial t} + U_i \frac{\partial \varepsilon}{\partial x_i} = \frac{\partial}{\partial x_i}\left(\frac{\nu_t}{\sigma_\varepsilon}\frac{\partial \varepsilon}{\partial x_i}\right) + c_{1\varepsilon}\frac{\varepsilon}{k}\nu_t\left(\frac{\partial U_i}{\partial x_j} + \frac{\partial U_j}{\partial x_i}\right)\frac{\partial U_i}{\partial x_j} - c_{2\varepsilon}\frac{\varepsilon^2}{k} \tag{2.6}$$

In the above equations, c_μ, $c_{1\varepsilon}$, $c_{2\varepsilon}$, σ_k, and σ_ε are empirical coefficients. The standard values of these coefficients are 0.09, 1.44, 1.92, 1.0, and 1.3, respectively (Rhodi, 1984). The first two terms on the left hand side of the k and ε equations represent rate of change and advection of the respective quantities. The first term on the right hand side represents diffusion in both cases. The two remaining terms represent the generation and destruction of stress, and energy, respectively.

Another turbulence scheme similar to the $k-\varepsilon$ scheme is the Renormalized Group $k-\varepsilon$ model (RNG). The RNG scheme handles the k and ε transport equations differently than the standard $k-\varepsilon$ scheme and was developed for use with strong shear flows or low intensity turbulence. In the RNG scheme the length scale of turbulent eddies vary from the area of flow to the scale at which eddies can be dissipated by viscosity. Energy cascades down this scale and at some eddy size the energy produced equals the energy being dissipated. The Renormalization Group technique uses this equilibrium eddy size or scale to describe all the other length scales. This produces a model that is statistically equivalent to the original Navier-Stokes equations but only describes a single scale of turbulence. This scale is of an order that can be efficiently handled by current computer technology. The Renormalized Group k and ε transport equations, as given by Bischof and Bucker (2003), are:

$$\frac{\partial k}{\partial t}+U_i\frac{\partial k}{\partial x_i}=\frac{\partial}{\partial x_i}\left[\left(\frac{\nu_{eff}}{P_{rk}}\right)\frac{\partial k}{\partial x_i}\right]+\nu_t\Lambda^2-\varepsilon \tag{2.7}$$

$$\frac{\partial \varepsilon}{\partial t}+U_i\frac{\partial \varepsilon}{\partial x_i}=\frac{\partial}{\partial x_i}\left[\left(\frac{\nu_{eff}}{P_{r\varepsilon}}\right)\frac{\partial \varepsilon}{\partial x_i}\right]+c_{1\varepsilon}\frac{\varepsilon}{k}\nu_t\Lambda^2-c_{2\varepsilon}\frac{\varepsilon^2}{k}-R \tag{2.8}$$

where P_{rk} and $P_{r\varepsilon}$ are Prandtl numbers for k and ε, respectively, Λ represents the mean rate of strain, and ν_{eff} is a combination of fluid kinematic viscosity and turbulent viscosity and is given by

$$\nu_{eff} = \nu_t \left(1 + \sqrt{\frac{\nu}{\nu_t}} \right)^2 \tag{2.9}$$

The term R on the right hand side of the transport equation for the dissipation rate is the major difference between this and the $k-\varepsilon$ scheme and is given by

$$R = \frac{c_\mu \eta^3 (1 - \eta/\eta_o)}{1 + \beta \eta^3} \frac{\varepsilon^2}{k} \tag{2.10}$$

where η_o and β are constants having standard values of 4.38 and 0.012, respectively, and $\eta = \Lambda k/\varepsilon$. The standard values of constants c_μ, $c_{1\varepsilon}$, and $c_{2\varepsilon}$ used in the RNG scheme are 0.0845, 1.42, and 1.68, respectively.

Both the $k-\varepsilon$ and RNG schemes have been extensively used with the RNG model employed for high shear and high Reynolds number flows. A sensitivity analysis of both schemes showed that the $k-\varepsilon$ scheme is less sensitive to c_μ than the RNG scheme. It was further found that the $k-\varepsilon$ scheme is more sensitive to $c_{1\varepsilon}$, and $c_{2\varepsilon}$ than RNG scheme. The RNG scheme is found to be more sensitive to the rate of strain because of the presence of the source term R (Bischof et al., 2003).

Numerical Model and Setup

A three-dimensional flow model called Flow-3D, developed by Flow Science, Inc., is used to simulate various jet geometries and flow conditions. The model solves the Reynolds-averaged Navier-Stokes equations using a finite volume/finite difference method in an Eulerian rectangular or cylindrical grid. The boundaries are determined independent of the grid generation process using

the Fractional Area/Volume Obstacle Representation (FAVOR) method, thus avoiding the "saw-tooth" representation of boundaries (Rodriguez et al., 2003).

The geometries used were a circular orifice of 5-mm in diameter for the circular jet and a slot width of 5-mm for the plane turbulent jet. Both jets flowed into a simulated tank 580-cm on a side. The tank was large enough in extent so that the jets could be considered free from the effects of boundaries and water surface. A uniform velocity of 200 cm/s was applied across the nozzle for the two jets. At tank boundaries, the normal and tangential components of velocities were set to zero. At the outflow section, a continuative boundary condition was applied that forced the normal derivatives of all the variables at the boundary to zero. At the wall, a smooth boundary was assumed by specifying a roughness height of zero. Initial conditions of zero velocity and hydrostatic pressure distribution were assumed inside the tank. Diagrams of the computational mesh used for plane and circular turbulent jets are given in Appendix F.

To enable an accurate comparison of the two turbulent closure schemes, the computational mesh as well as initial and boundary conditions for the simulation of jets with the $k-\varepsilon$ and RNG turbulent closure schemes were exactly the same. However, the mesh for the circular turbulent and plane turbulent jets differed in order to appropriately capture the nozzle geometry. The computed results, at the center of each cell, were the velocity components in the x, y, and z directions, pressure, turbulent kinetic energy per unit mass, and turbulent dissipation rate.

Turbulent Jets

The details of a circular turbulent or plane turbulent jet are shown in Fig. 2.1. For the plane turbulent jet, $2b_o$ represents the width of the nozzle, and d is the diameter of the nozzle for circular turbulent jet. The initial uniform velocity of the jet exiting the nozzle is given by u_o. The virtual origin is at a distance $\bar{x}$ from the nozzle, and the centerline velocity at any position x (distance along the jet) is given by u_m. The velocity varies from the centerline value, u_m, to zero at the edge of the jet. For linear scale and growth of jets, length b is commonly used. Distance b is measured along y or r (for plane turbulent or circular turbulent jets, respectively) coordinate direction to a point where $u = 0.5u_m$.

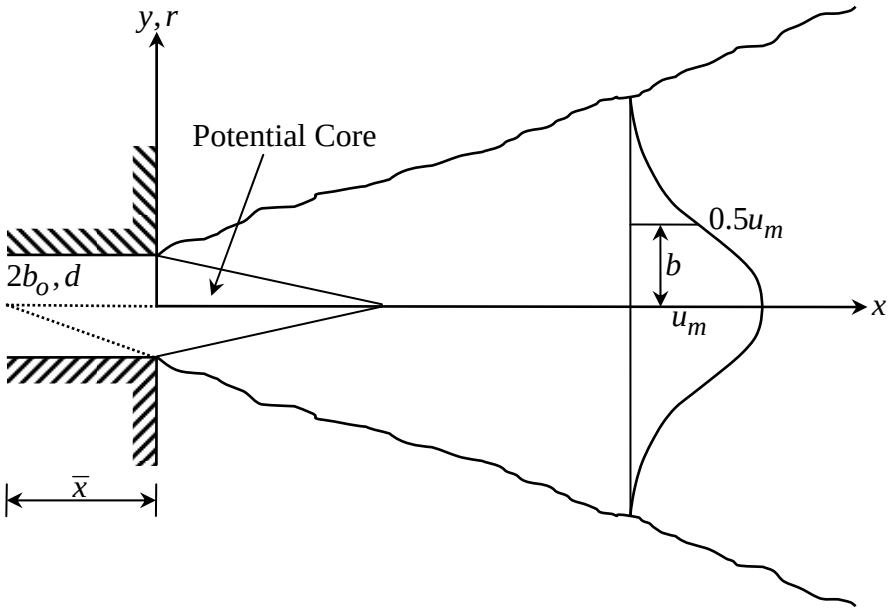

Fig. 2.1: Definition Sketch of Free Turbulent Jet

The growth rates of the free plane and circular jets are given by

$$b/b_o = A_1\left(x+\bar{x}\right)/b_o \tag{2.11a}$$

$$b/d = A_2\left(x+\bar{x}\right)/d \tag{2.11b}$$

where A_1 and A_2 are coefficients for plane and circular turbulent jets, respectively. The value of 0.097 for A_1 was found as a best fit the experimental data (Rajaratnam, 1976). Abramovich (1963) recommended a value of 0.097 for A_2. The virtual origin ranged from 0 to $2.4b_o$ behind the nozzle for plane turbulent jets, and from $0.6d$ to $2.2d$ behind the nozzle for circular jets (Rajaratnam, 1976).

The decay of the centerline velocities for the plane and circular turbulent jets are given by the following equations

$$\frac{u_m}{u_o} = \frac{A_3}{\sqrt{x/b_o+\alpha_1}} \tag{2.12a}$$

$$\frac{u_m}{u_o} = \frac{A_4}{x/d+\alpha_2} \tag{2.12b}$$

where A_3 and A_4 are given by 3.5 and 6.3, respectively. The values α_1 and α_2 represent correction for the virtual origin. The velocity profiles across the jet are found to be similar and can be approximated by a Gaussian curve of the form (Rajaratnam, 1976)

$$\frac{u}{u_m} = \exp\left(-0.693\lambda^2\right) \tag{2.13}$$

where λ is given by y/b or r/b for plane or circular turbulent jet, respectively.

Simulation Results for Plane Turbulent Jet

To determine the accuracy of the simulated results for the plane jet, the growth rate, the decay of the centerline longitudinal velocity, the longitudinal and vertical velocity profiles across the jet, and the turbulent kinetic energy profile are compared with experimental data and accepted empirical equations. Relative error plots are given in Appendix D to further quantify the results. The relative error is given by the difference between the computed and expected value divided by the expected value. The growth rates of the plane turbulent jet based on $k-\varepsilon$ and RNG schemes are found to be 0.11 and 0.12, respectively, which compare well with the value given by Eq. (2.11a). The virtual origin for $k-\varepsilon$ and RNG schemes are found to be $5.96b_o$ and $1.32b_o$, respectively.

Figs. 2.2 and 2.3 show the decay of the centerline longitudinal velocity along the jet using $k-\varepsilon$ and RNG schemes, respectively. For reference, the decay of the centerline velocity given by Eq. (2.12a) is also provided in these figures. Although both schemes satisfactorily predict the decay of the centerline longitudinal velocity, the $k-\varepsilon$ scheme provides a better estimate of the decay. The RNG scheme predicts lower centerline velocity immediately after the potential core and in the lower half of the jet with a maximum error of -0.056.

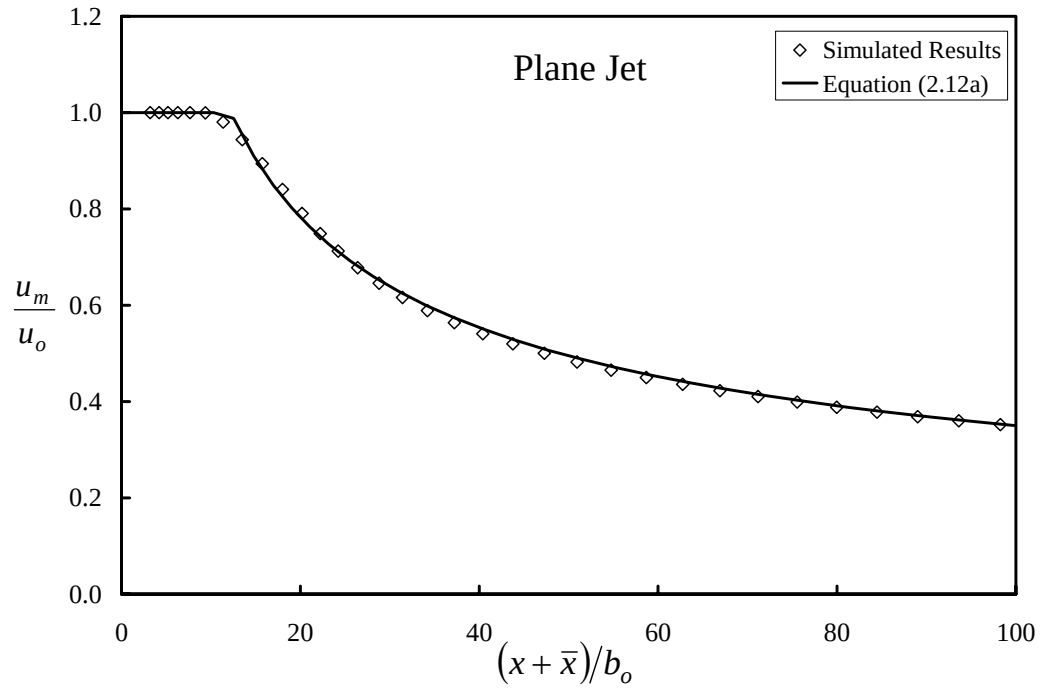

Fig. 2.2: Centerline Velocity Decay of Plane Jet ($k-\varepsilon$ Scheme)

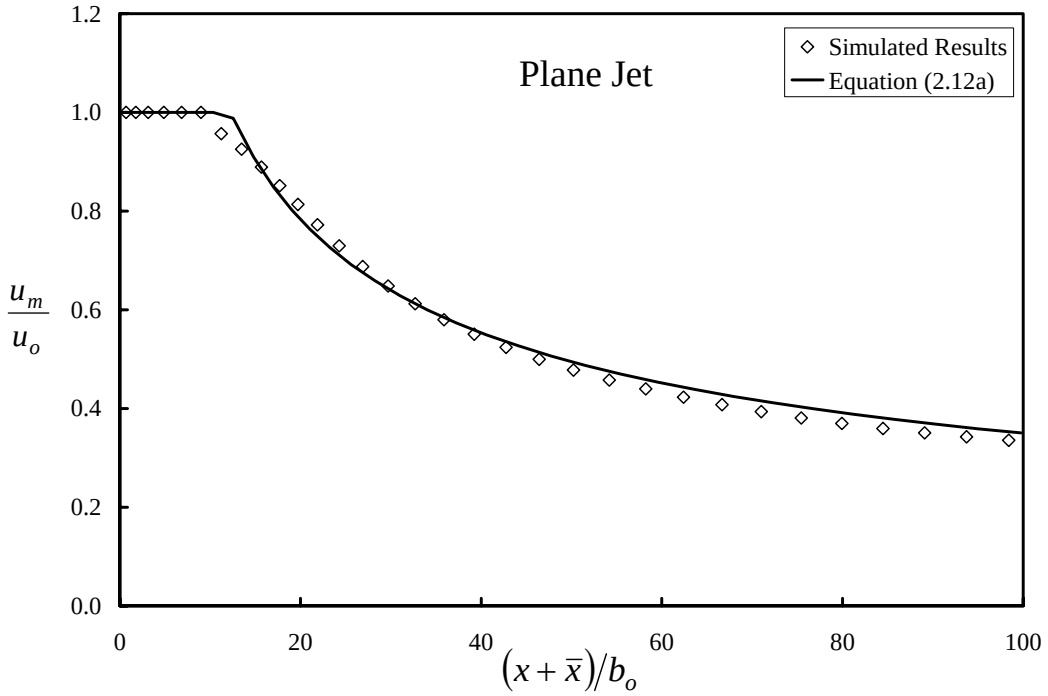

Fig. 2.3: Centerline Velocity Decay of Plane Jet (RNG Scheme)

The similarity of longitudinal velocity profiles across the jet at different locations is tested by comparing the predicted velocity profiles with Eq. (2.13). The velocity profiles obtained using the $k-\varepsilon$ and RNG schemes are shown in Figs. 2.4 and 2.5, respectively, along with Eq. (2.13). Though the velocity profile immediately after the potential core is poorly predicted by both schemes, the RNG scheme is the worse of the two predictors. The relative error of the RNG scheme increases to -0.5 when y/b is 0.5 while the $k-\varepsilon$ scheme stays within 0.1. The velocity profiles further away from the potential core follow the Gaussian curve more closely.

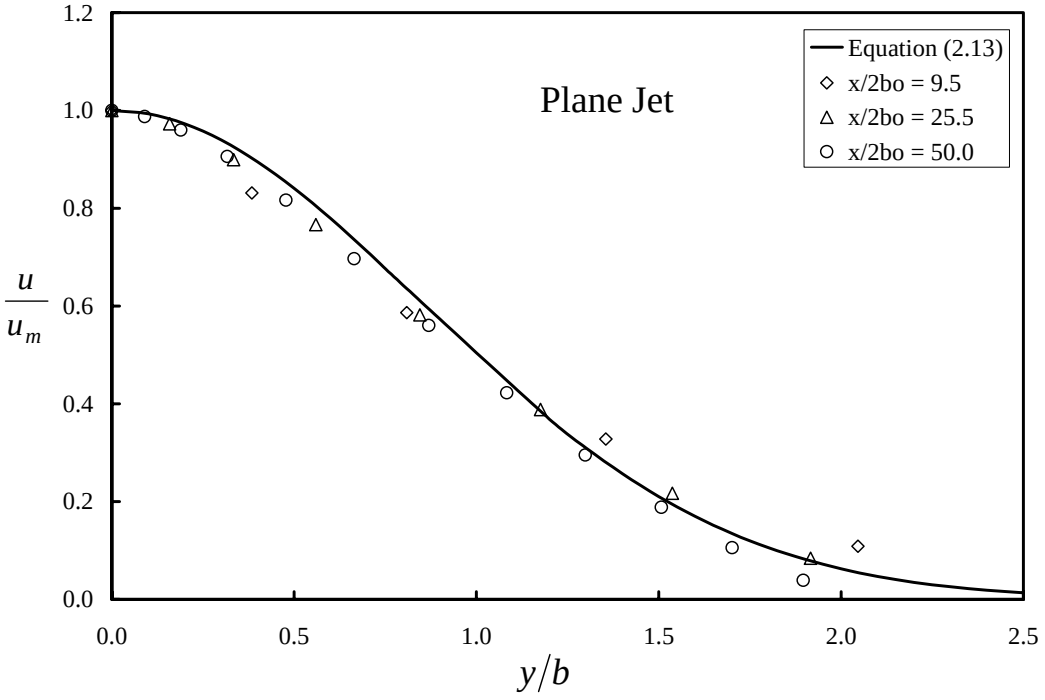

Fig. 2.4: Similarity of Longitudinal Velocity ($k-\varepsilon$ Scheme)

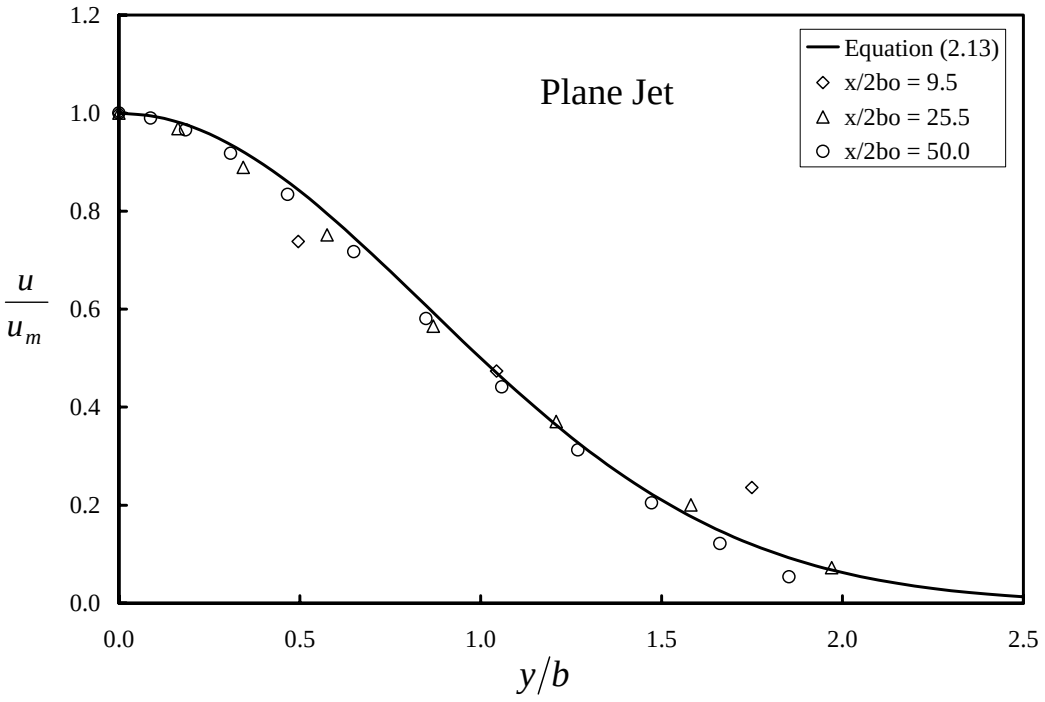

Fig. 2.5: Similarity of Longitudinal Velocity (RNG Scheme)

The vertical velocity profiles across the jet predicted by the $k-\varepsilon$ and RNG schemes are compared to Goertler's solution (Rajaratnam, 1963) in Figs. 2.6 and 2.7, respectively. The Goertler's solution is given by

$$\frac{v}{u_m} = \frac{1}{\alpha}\left(\frac{\alpha y}{x} - \frac{\alpha y}{x}\tanh^2\left(\frac{\alpha y}{x}\right) - 0.5\tanh\left(\frac{\alpha y}{x}\right)\right) \tag{2.14}$$

where α has a value of 7.67, v is the vertical velocity (y-direction). The velocity profiles predicted by the two schemes compare well with the theoretical profile.

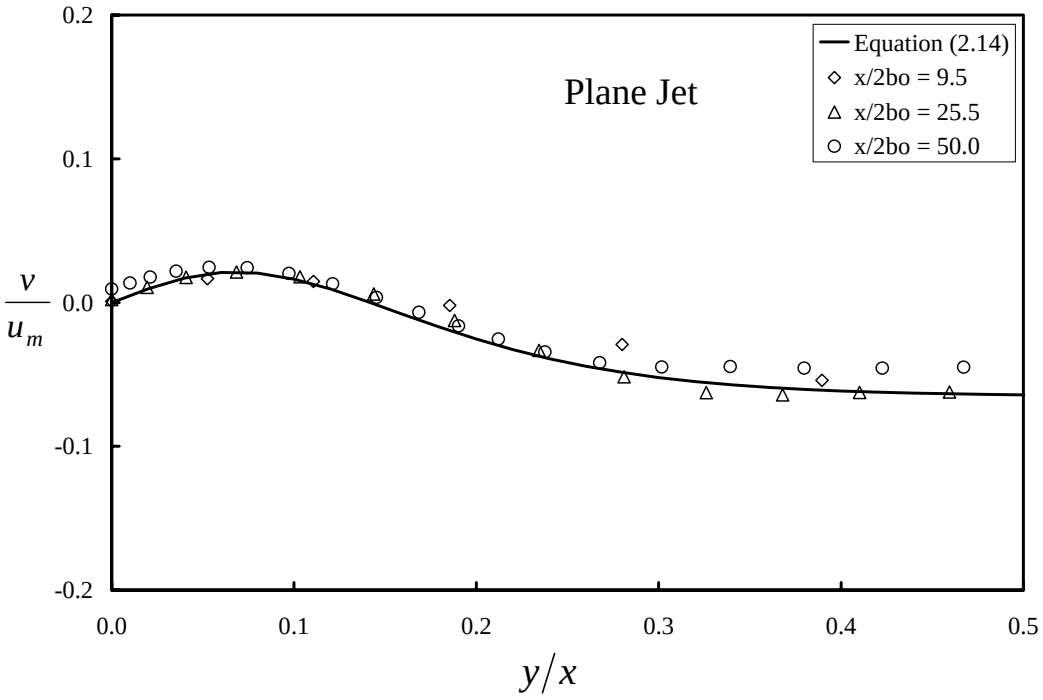

Fig. 2.6: Similarity of Vertical Velocity ($k-\varepsilon$ Scheme)

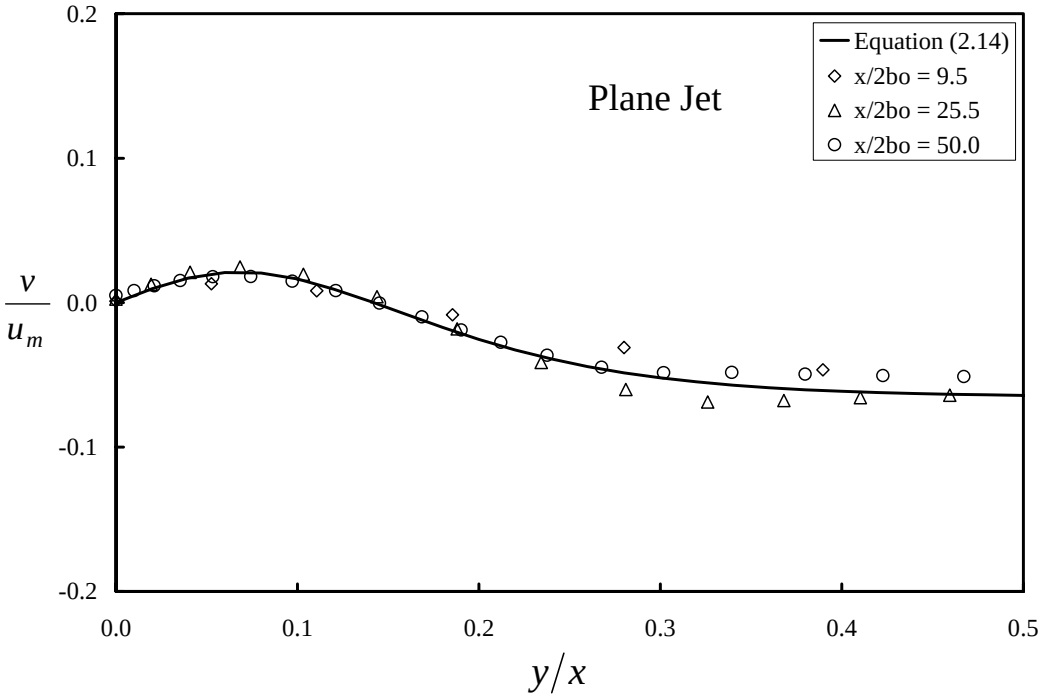

Fig. 2.7: Similarity of Vertical Velocity (RNG Scheme)

Figs. 2.8 and 2.9 show the profiles of kinetic energy per unit mass at $x/2b_0 = 50$ obtained using $k-\varepsilon$ and RNG schemes, respectively. These profiles are compared with the physical model data of Heskestad (1965) at the same location. The results from the $k-\varepsilon$ scheme do not conform to the experimental data near the centerline of the jet, while the RNG scheme predicts a slightly higher k value throughout.

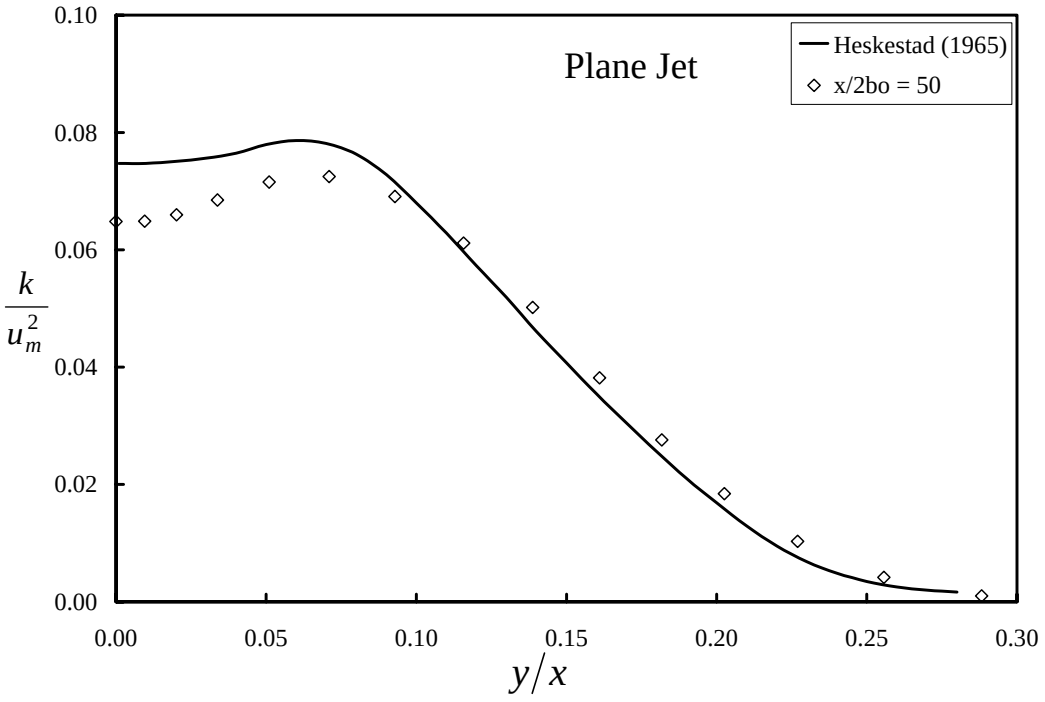

Fig. 2.8: Profile of Turbulent Kinetic Energy ($k-\varepsilon$ Scheme)

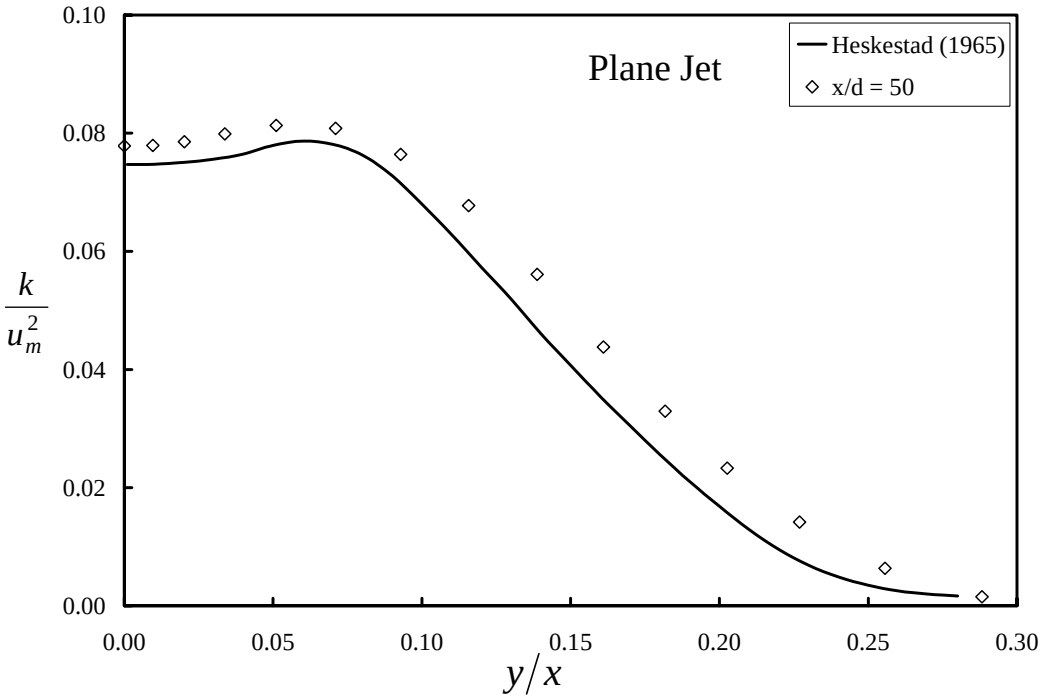

Fig. 2.9: Profile of Turbulent Kinetic Energy (RNG Scheme)

From the above discussion, it is clear that the $k-\varepsilon$ scheme performs slightly better than the RNG scheme for predicting the growth rate, similarity of longitudinal and vertical velocity profiles, and centerline velocity decay of the plane turbulent jet. On the other hand, the RNG scheme can more accurately predict the kinetic energy per unit mass across the plane jet.

Simulation Results for Circular Turbulent Jet

For the circular turbulent jet, the same set of comparisons, as described for the plane turbulent jet, are conducted. The growth rates for the circular turbulent jet using $k-\varepsilon$ and RNG schemes are 0.1 and 0.14, respectively, and the corresponding virtual origins are located at $5.56d$ and $0.86d$. The growth rate

based on the RNG scheme is higher than the generally accepted value of 0.097, while the $k-\varepsilon$ turbulent closure scheme accurately predicts the growth rate.

The decay of the centerline longitudinal velocity obtained using $k-\varepsilon$ and RNG schemes are compared with Eq. (2.12b) in Figs. 2.10 and 2.11, respectively. The RNG scheme predicts lower centerline velocity immediately following the potential core and the trend continues for almost the entire length investigated. The results from the $k-\varepsilon$ scheme compare well with Eq. (2.12b).

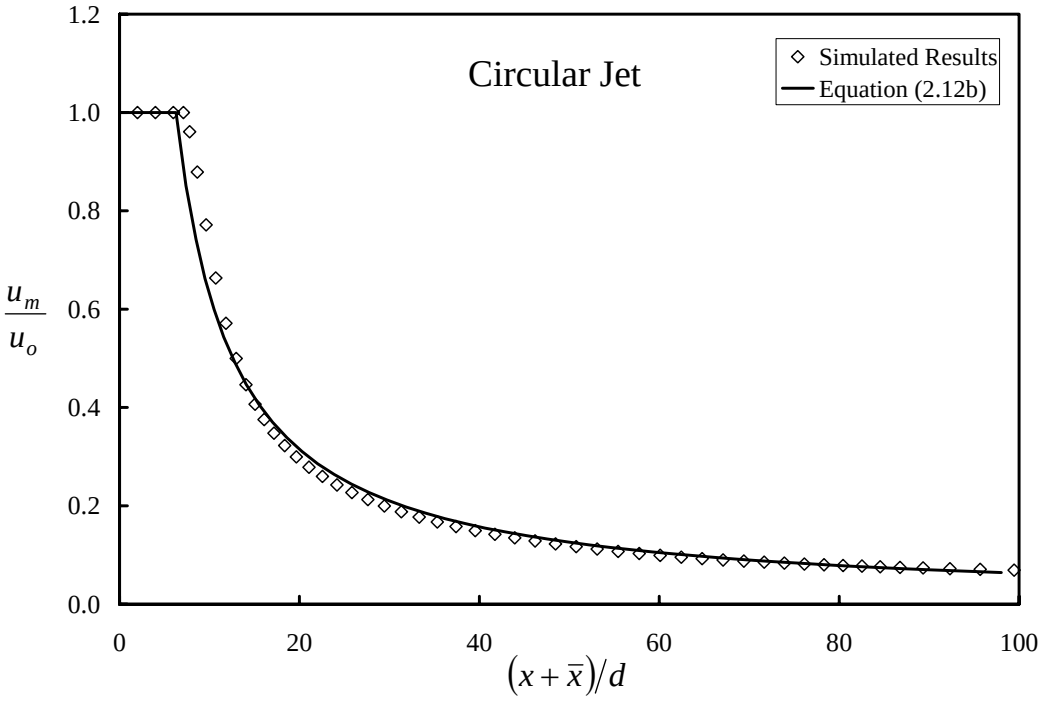

Fig. 2.10: Centerline Velocity Decay of Plane Jet ($k-\varepsilon$ Scheme)

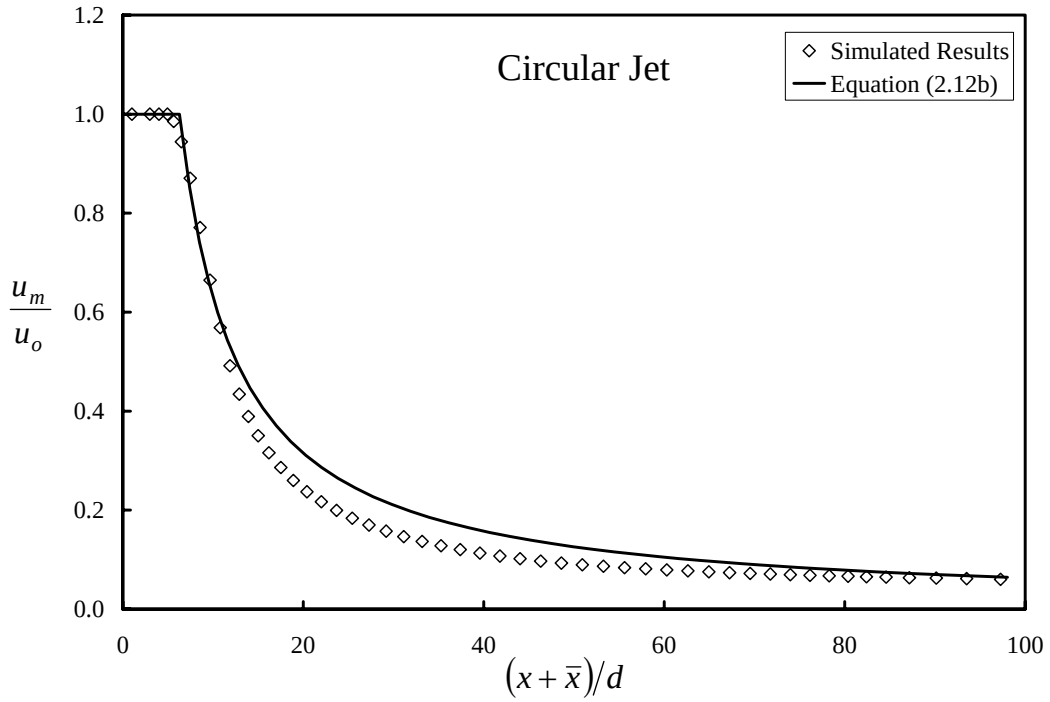

Fig. 2.11: Centerline Velocity Decay of Plane Jet (RNG Scheme)

Eq. (2.13) is used to test the similarity characteristics of the longitudinal velocity profiles obtained from the two turbulent closure schemes. Figs. 2.12 and 2.13 show the velocity profiles from the $k-\varepsilon$ and RNG schemes, respectively. Although the overall agreement of the velocity profiles at different locations is satisfactorily predicted by the two schemes, the RNG scheme shows a discrepancy in predicting the velocity profile immediately following the potential core.

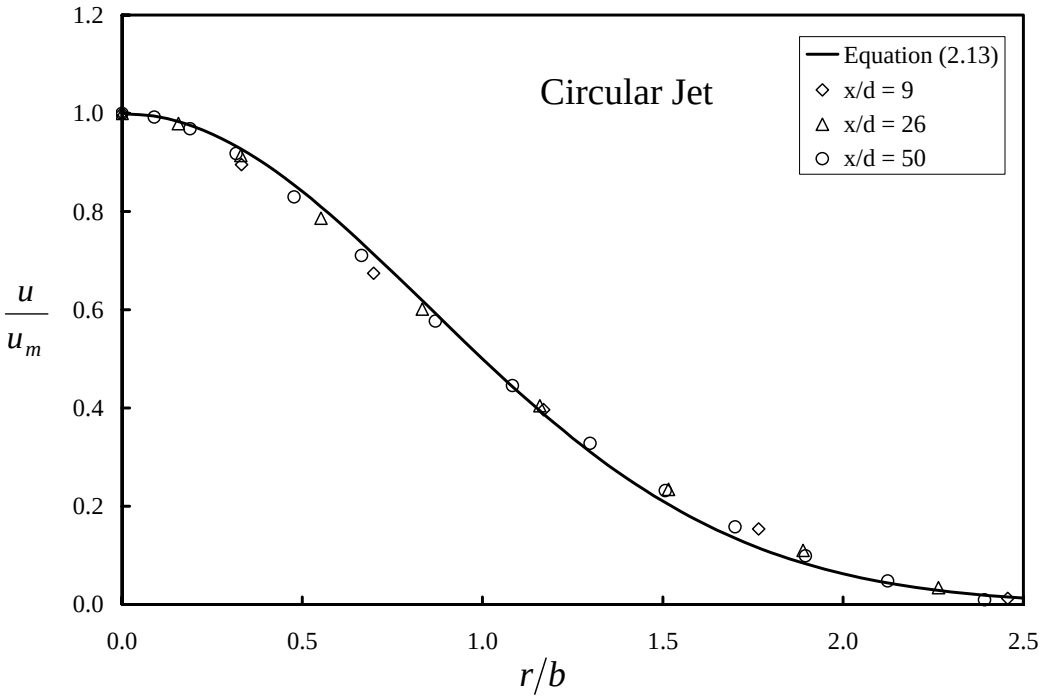

Fig. 2.12: Similarity of Longitudinal Velocity ($k-\varepsilon$ Scheme)

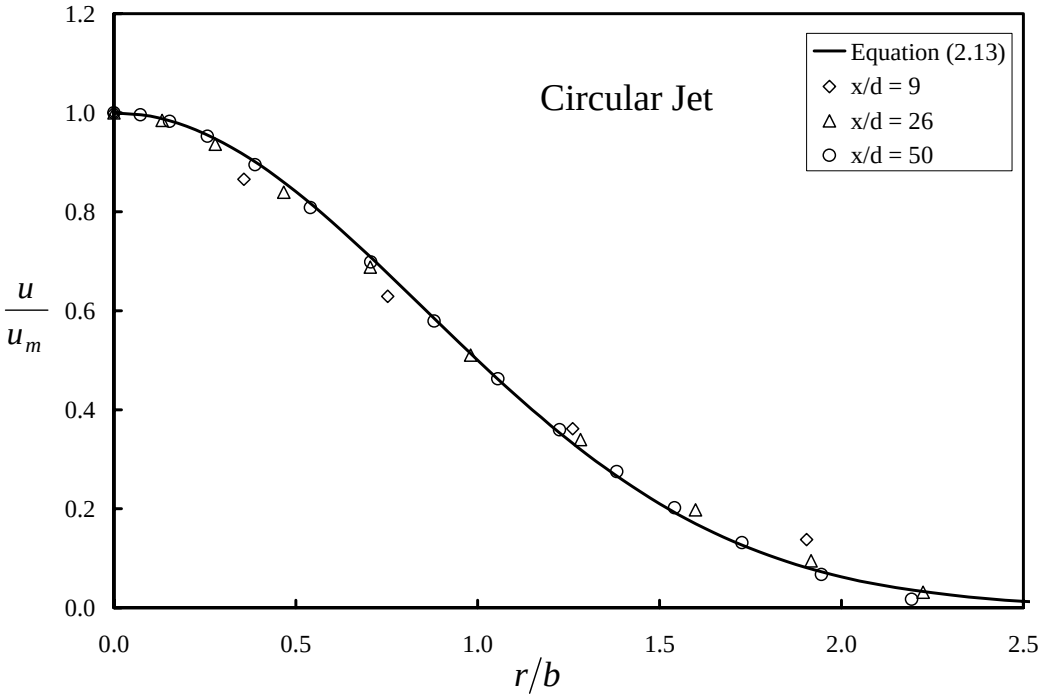

Fig. 2.13: Similarity of Longitudinal Velocity (RNG Scheme)

The radial velocity profiles at different locations obtained using $k-\varepsilon$ and RNG schemes are compared with the vertical velocity profile given by Tollmien's solution up to r/x of 3.1 (Abramovich, 1963) in Figs. 2.14 and 2.15, respectively. Although both schemes perform well in predicting the vertical velocity profiles, the results from the $k-\varepsilon$ scheme are slightly better.

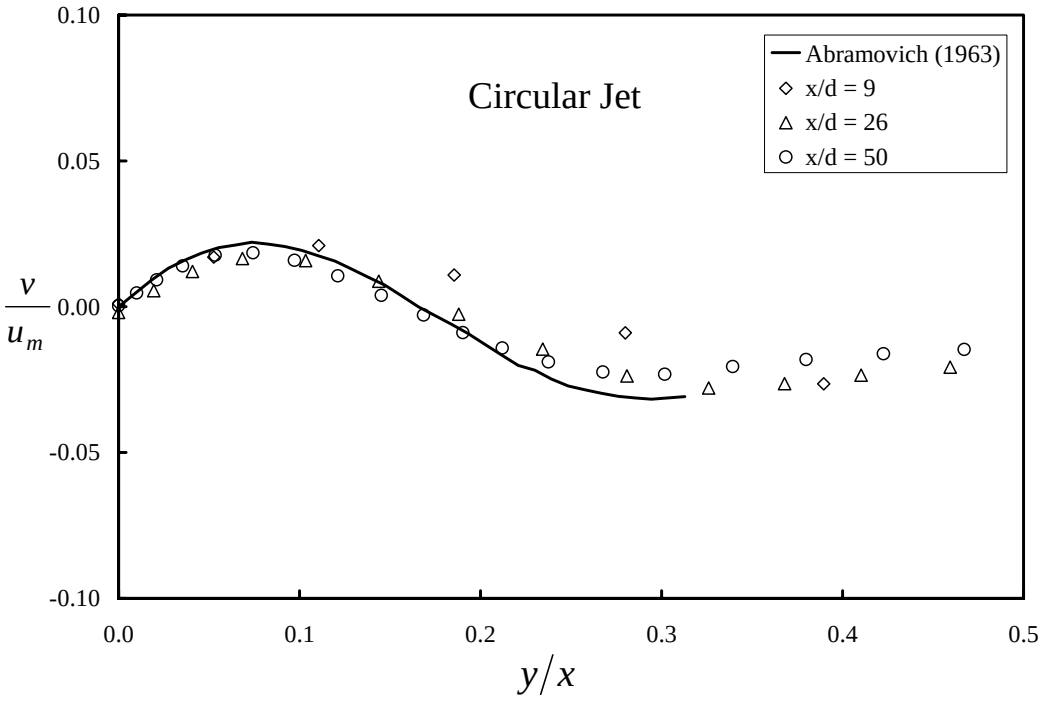

Fig. 2.14: Similarity of Vertical Velocity ($k-\varepsilon$ Scheme)

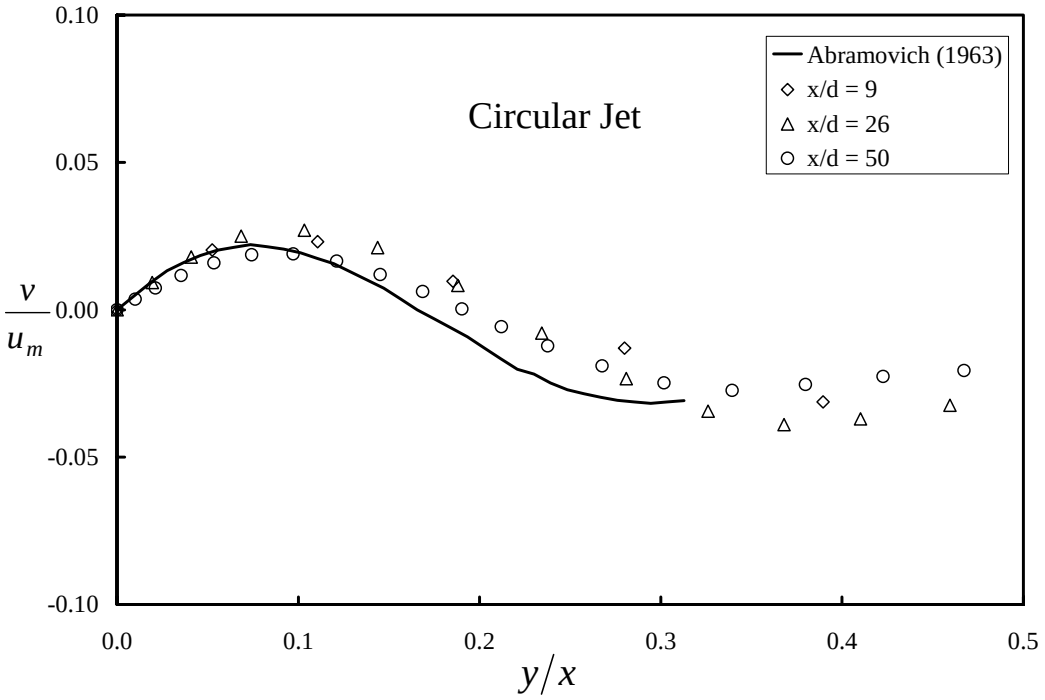

Fig. 2.15: Similarity of Vertical Velocity (RNG Scheme)

The kinetic energy per unit mass predicted by the two schemes at $x/d = 61.5$ is compared with the experimental data of Wygnanski and Fiedler (1969). The comparisons for the $k-\varepsilon$ and RNG schemes are shown in Figs. 2.16 and 2.17. Though both schemes perform poorly in predicting the kinetic energy per unit mass, the $k-\varepsilon$ scheme performs better on average than the RNG scheme.

For the circular turbulent jet, the $k-\varepsilon$ scheme clearly performs better for predicting the growth rate and the decay of the centerline longitudinal velocity. Both schemes adequately predict the similarity of longitudinal and radial velocity profiles at different locations along the jet. However, the two schemes, especially the RNG scheme, are unable to predict the kinetic energy per unit mass profile.

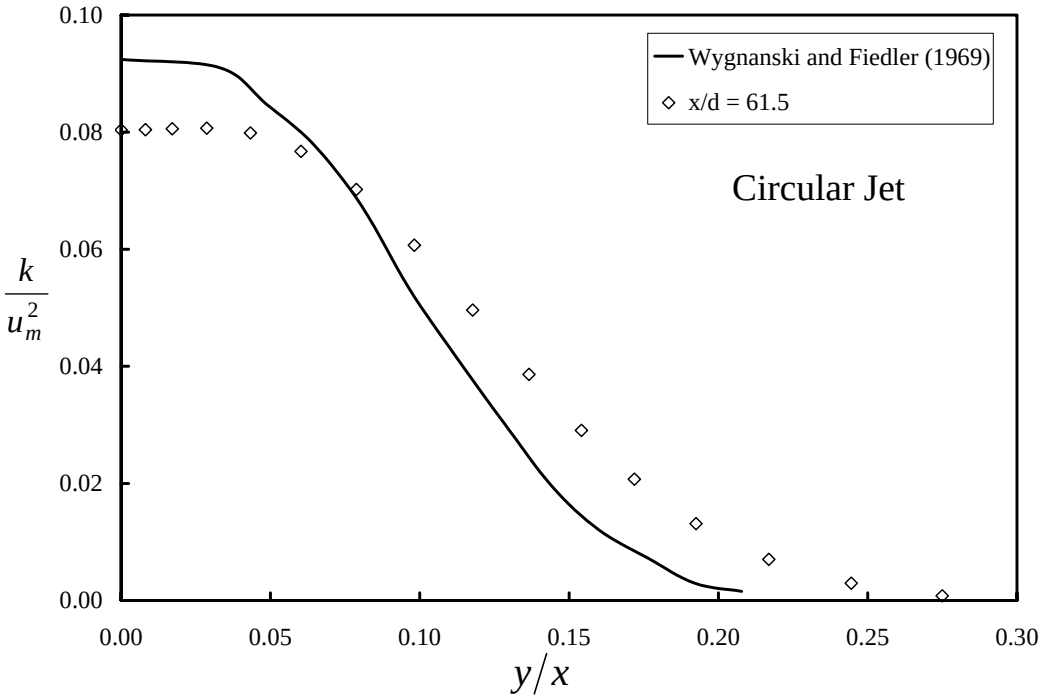

Fig. 2.16: Profile of Turbulent Kinetic Energy ($k-\varepsilon$ Scheme)

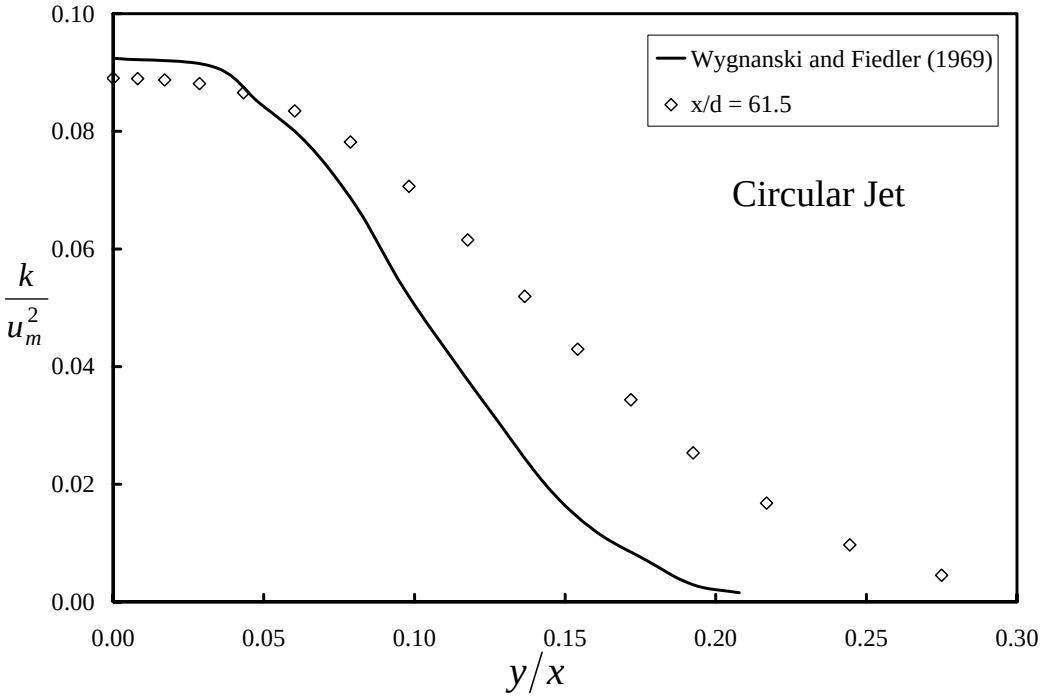

Fig. 2.17: Profile of Turbulent Kinetic Energy (RNG Scheme)

Summary and Conclusions

The $k-\varepsilon$ and RNG schemes, employed in a three-dimensional turbulent flow model (FLOW-3D), with standard coefficients are evaluated for predicting the characteristics of both the free plane and circular turbulent jets. In particular, the growth rate, the decay of the centerline longitudinal velocity, the similarity of longitudinal and vertical velocity profiles at different locations along the jet, and profiles of kinetic energy per unit mass are compared with the available experimental data and theoretical analysis.

The results show that the $k-\varepsilon$ scheme provides a better estimation of growth rates and decay of the centerline longitudinal velocity both for plane and circular turbulent jets. Both schemes satisfactorily predict the similarity of longitudinal and vertical or radial velocity profiles, however, the $k-\varepsilon$ scheme provides slightly better results. The estimation of kinetic energy per unit mass by both schemes incurs appreciable error especially in the case of the circular jet. From the simulation results of ideal circular and plane turbulent jets, it is clear that the $k-\varepsilon$ turbulent closure scheme with standard coefficients, although simpler, can be used to effectively predict the characteristics of plane and circular turbulent jets.

CHAPTER 3
MODELING SUBMERGED HYDRAULIC JUMP

Hydraulic jumps (free and submerged) are commonly used for energy dissipation downstream of spillways and sluice gates. These flow features also exist in natural streams, especially in mountainous regions and downstream of free overfalls. Submerged jumps are also common features downstream of curtain walls within pump intakes. The energy dissipation in hydraulic jumps occurs through the formation of a turbulent shear layer observed as a large roller. A hydraulic jump forms when flow changes from the upstream supercritical state to the downstream subcritical state. The depths immediately before and after the free hydraulic jumps are called sequent depths. Given the upstream or downstream depth, the corresponding sequent depth can be determined using Ballenger's equation, which is based on the momentum conservation principle across a hydraulic jump. A free hydraulic jump forms when subcritical sequent depth occurs downstream of the supercritical region. The roller is on the water surface and unsubmerged. If the downstream depth is greater than the sequent depth required for the supercritical flow immediately downstream of a sluice gate, as shown in Fig. 3.1, the inlet is drowned thus forming a submerged hydraulic jump with a roller that is drowned or submerged. The submerged jump is characterized by a submergence factor, S , and is given by

$$S = \frac{y_t - y_2}{y_2} \tag{3.1}$$

where y_t is the downstream depth and y_2 is the subcritical sequent depth for the supercritical flow at the inlet (Long, 1991).

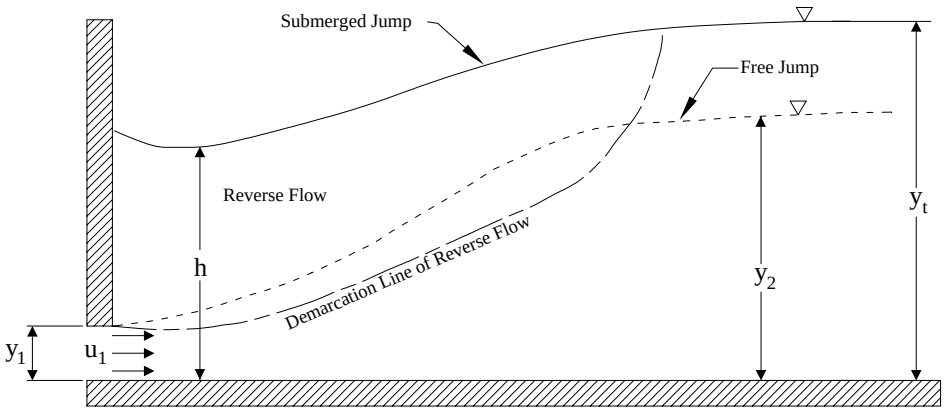

Figure 3.1: Definition Sketch of a Hydraulic Jump

Many researchers have investigated hydraulic jumps. However, Rouse (1958) was the first to measure the turbulence structure within a free hydraulic jump using a hot wire technique. The experimental results showed that turbulence was generated rapidly in the first half length of the roller and was dissipated a short distance downstream. The turbulence data measured were then used to integrate the momentum and energy equations over a control volume to determine various flow characteristics, such as surface profile and jump length. Madsen and Svendsen (1983) also developed an integral method to model free hydraulic jumps using an algebraic turbulence closure scheme. A simplified $k-\varepsilon$ model was also presented but an algebraic closure scheme was found to be just as accurate. The results showed that the surface profile was not sensitive to

the form of the velocity profile assumed and that the smaller the upstream Froude number the steeper the hydraulic jump. Rajaratnam (1965) showed that the velocity profiles below the roller, in both submerged and free jumps, resembled those of a turbulent wall jet under an adverse pressure gradient. Long (1991) performed experiments on submerged hydraulic jumps downstream of a sluice gate and measured mean and turbulent flow characteristics using a Laser Doppler Velocimeter (LDV). The measured data were compared to that predicted from a two-dimensional flow model. The flow model with the standard $k-\varepsilon$ scheme was developed using an offset control volume method. By using this computational model, Long (1991) made turbulence part of the predictive solution instead of an assumption as with the most previous integral techniques. Long (1991) found that the recirculating region of the jump was three dimensional and the $k-\varepsilon$ model results over predicted the water surface profiles at higher inlet Froude numbers in this region. It was reported that the normal turbulent stress in the longitudinal direction and the reverse flow velocities were underestimated by the $k-\varepsilon$ model. Gunal and Narayanan (1998) used a two dimensional flow model with a $k-\varepsilon$ turbulent closure scheme to simulate submerged hydraulic jumps. The model results were compared to the experimental data of Long (1991). The two dimensional model was developed using a boundary-fitted coordinate system to map the complicated boundaries of a submerged hydraulic jump onto a rectangular computational plane. Gunal and Narayanan (1998) considered the prediction of turbulent normal stress in the longitudinal direction to be poor when compared with experimental data and was attributed to the

assumption of isotropic normal stresses by the $k-\varepsilon$ model. The data of turbulent normal stress in the vertical direction and shear stress showed better agreement with the experimental data in the downstream portion of the jump.

With advances in computer technology, the use of two- and three-dimensional flow models to investigate complicated turbulent flow problems is becoming increasingly feasible. One of the major components of these models is the turbulent closure scheme. In recent years, the Renormalized Group (RNG) $k-\varepsilon$ turbulent closure scheme has been found to model the shear flows better than the original $k-\varepsilon$ scheme (Bischof et al., 2003). In this study, the accuracy of the $k-\varepsilon$ and RNG turbulent closure schemes employed in a three-dimensional flow model is assessed in simulating the submerged hydraulic jump.

Experimental Setup and Computational Model

The experimental results of Long (1991) are used for validating the simulated results obtained from a three-dimensional flow model where $k-\varepsilon$ and RNG turbulent closure schemes with standard coefficients are employed. The geometry and numerical mesh are copied as closely as possible from Long (1991). The computational model Flow-3D was used to simulate various scenarios of submerged hydraulic jump. A more in-depth description of the computational model is given in Chapter 2. However, it should be mentioned here that a modified volume of fluid method is used by the model to predict the location of the free surface during the solution.

The simulations were performed using a horizontal rectangular channel as used in laboratory tests. The channel was 7.5 m long, 0.467 m wide and 0.515 m deep. A diagram of the computational mesh used is given in Appendix F. Three different flow geometries were examined. The gate opening, y_1, the inlet Froude number, $F_1 = u_1 / \sqrt{g y_1}$, and downstream flow depth, y_t, were varied for each case. The upstream boundary condition was a uniform inlet velocity, u_1, and the downstream boundary condition was the tailwater depth, y_t, as measured by Long (1991). Mean and turbulent flow quantities were measured using a Laser Doppler Velocimeter by Long (1991) in the vertical plane of $z/w = 0.36$ or 168 mm from the river right wall, where z is the distance measured from the right wall and w is the width of the channel. The flow parameters of each test are shown in Table 3.1.

Table 3.1: Flow Conditions for Simulated Tests

Test Number	y_1 (mm)	u_1 (m/s)	y_t (mm)	F_1	S
1	25	1.58	187	3.19	0.85
2	25	2.72	299	5.49	0.63
3	15	3.14	206	8.19	0.24

The computed and measured quantities compared are normalized longitudinal velocity profiles, vertical velocity profiles, vertical profiles of turbulent kinetic energy per unit mass, and maximum longitudinal velocity along the length of the channel. Comparisons of water surface profiles are also presented. The velocities are normalized with u_1, kinetic energy with u_1^2 and the

lengths with y_1. Relative error plots of representative locations are given in Appendix E.

Discussion of Results

The computed and measured water surface profiles for the three tests are shown in Figs. 3.2, 3.3, and 3.4, respectively. The $k-\varepsilon$ and RNG schemes provide similar results for the water surface profiles for the three tests. The difference between the computed and measured water surface profiles increases as the inlet Froude number increases. The large dip shown in the experimental results of test 3 is not captured by either model; however the RNG results show a more defined dip than the $k-\varepsilon$ results. It was mentioned by Long (1991) that the measurements of water surface profiles with a point gauge at higher inlet Froude numbers were not as accurate due to water surface fluctuations (as much as 10 mm in some cases). The water surface levels downstream of the recirculation zones are accurately predicted in all three cases.

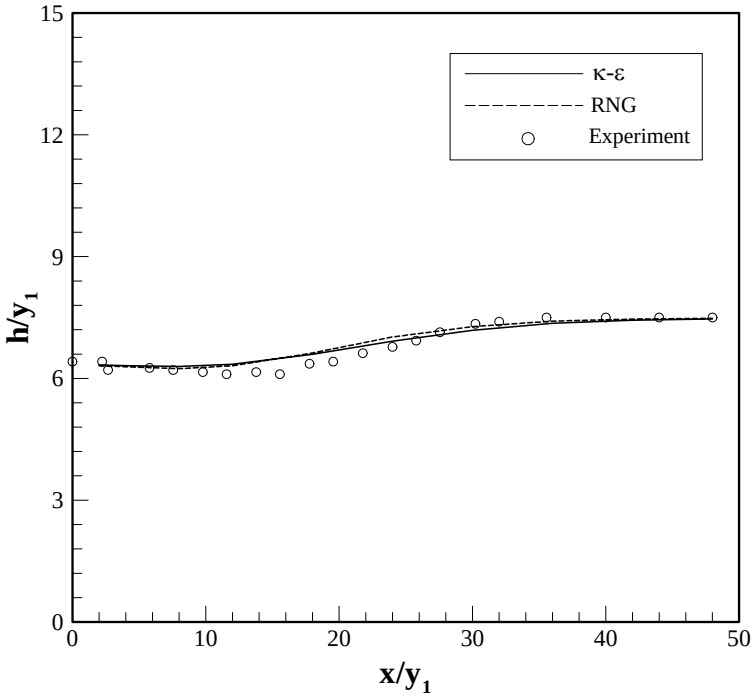

Figure 3.2: Water Surface Profile for Test 1 ($F_1 = 3.19$, $S = 0.85$)

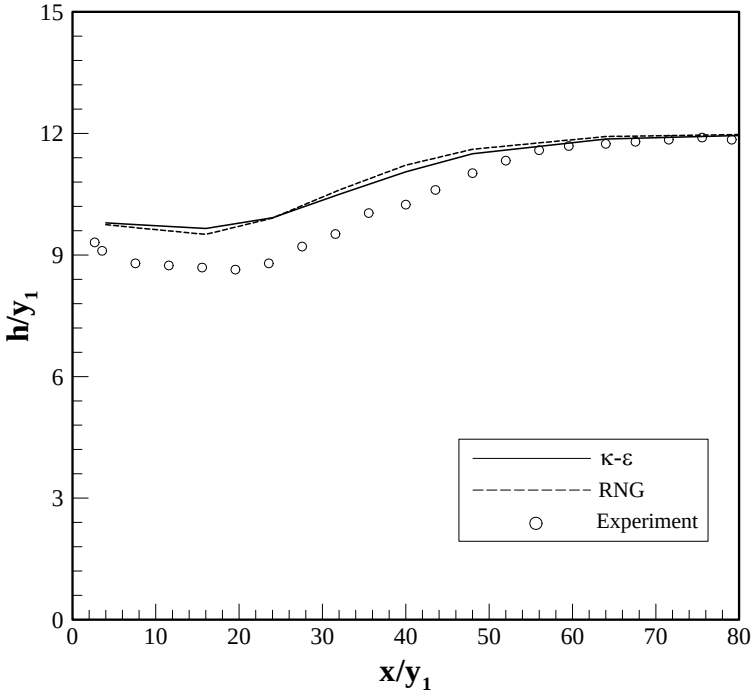

Figure 3.3: Water Surface Profile for Test 2 ($F_1 = 5.49$, $S = 0.63$)

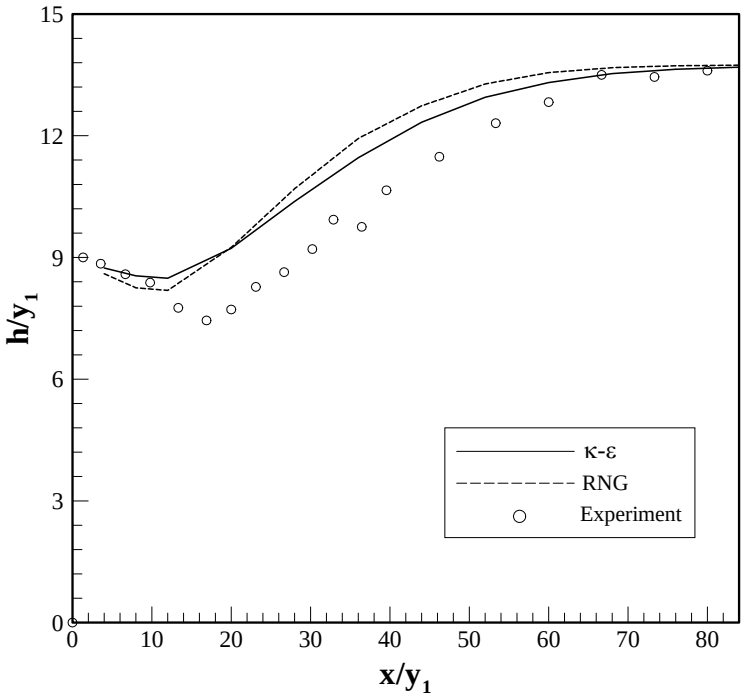

Figure 3.4: Water Surface Profile for
Test 3 ($F_1 = 8.19, S = 0.24$)

The computed and measured profiles of maximum longitudinal velocity occurring in the vertical direction along the length of the jump are shown in Figs. 3.5, 3.6, and 3.7 for the three tests. In all three cases, the RNG scheme performs better than the $k-\varepsilon$ scheme in predicting the maximum longitudinal velocity. The $k-\varepsilon$ scheme over predicts the maximum velocity, especially for higher Froude numbers.

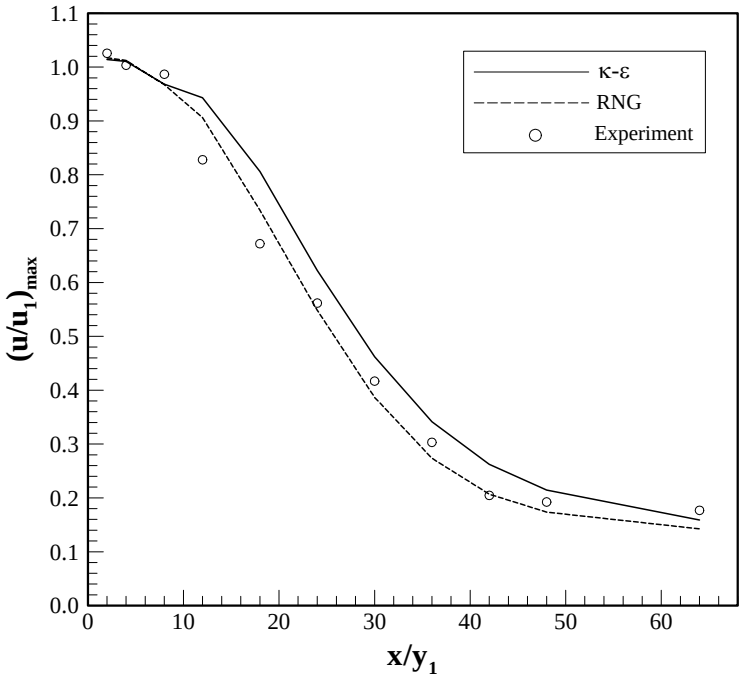

Figure 3.5: Maximum Longitudinal Velocity for Test 1 ($F_1 = 3.19, S = 0.85$)

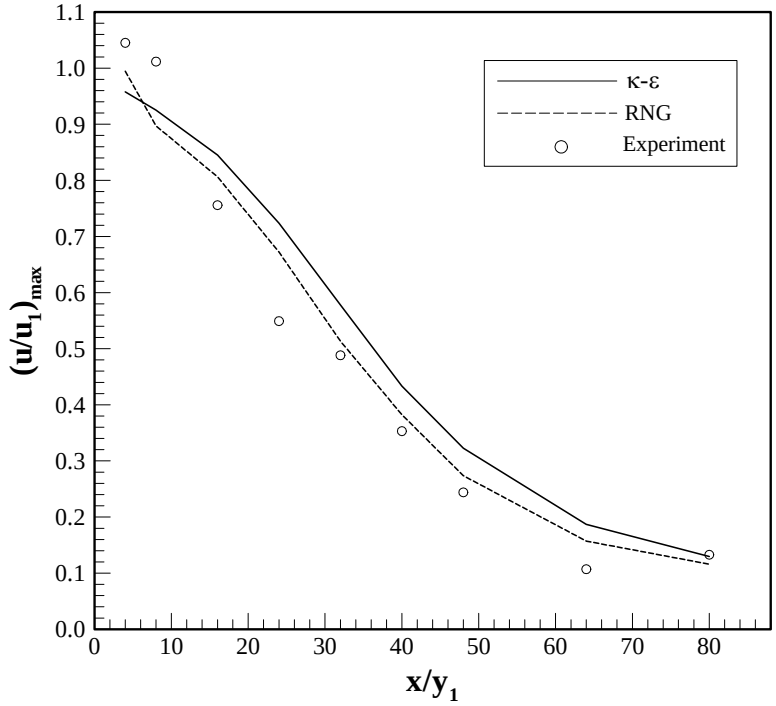

Figure 3.6: Maximum Longitudinal Velocity for Test 2 ($F_1 = 5.49, S = 0.63$)

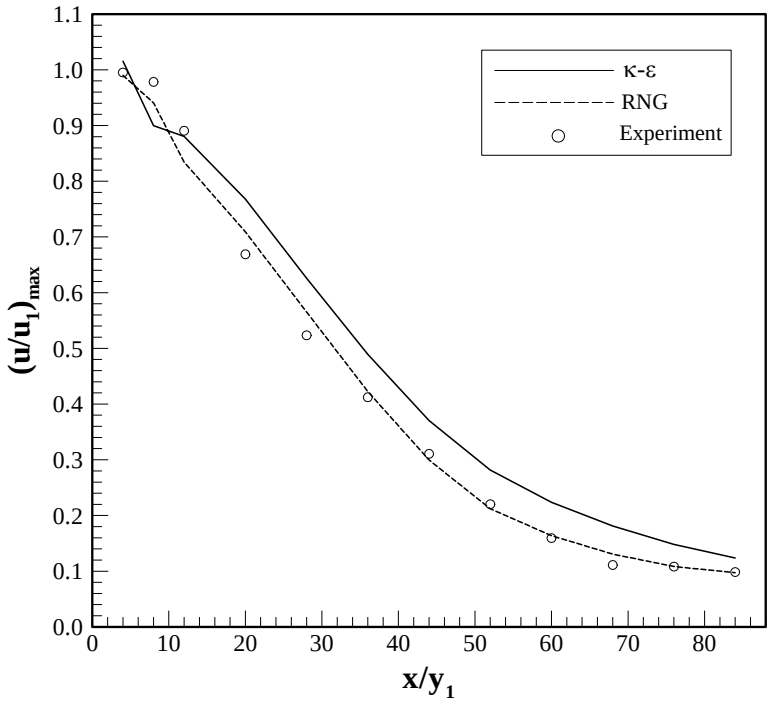

Figure 3.7: Maximum Longitudinal Velocity
for Test 3 ($F_1 = 8.19, S = 0.24$)

Figures 3.8 – 3.13 show computed and measured longitudinal velocity profiles in the vertical direction at various locations along the channel. The longitudinal velocities in the shear layers (zones between the gate and reverse velocity), are over estimated within x/y_1 of 12, especially for the low Froude number in the first test. This overestimation also raises the point where the longitudinal velocity changes from positive and negative. The computed velocity profiles beyond x/y_1 of 12 match the measured profiles accurately across the whole flow depth. However, it is clear that the RNG scheme performs better than the $k-\varepsilon$ scheme near the bed and predicts the location and magnitude of maximum velocity more accurately. The length of recirculation zone is predicted accurately by the both schemes.

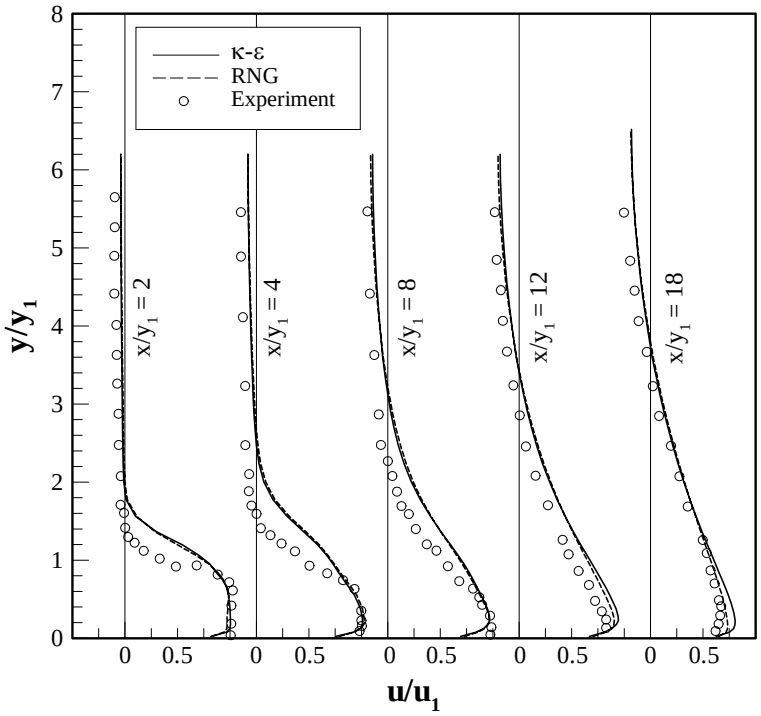

Figure 3.8: Longitudinal Velocity Profiles for Test 1
for $x/y_1 = 2 - 18$ ($F_1 = 3.19, S = 0.85$)

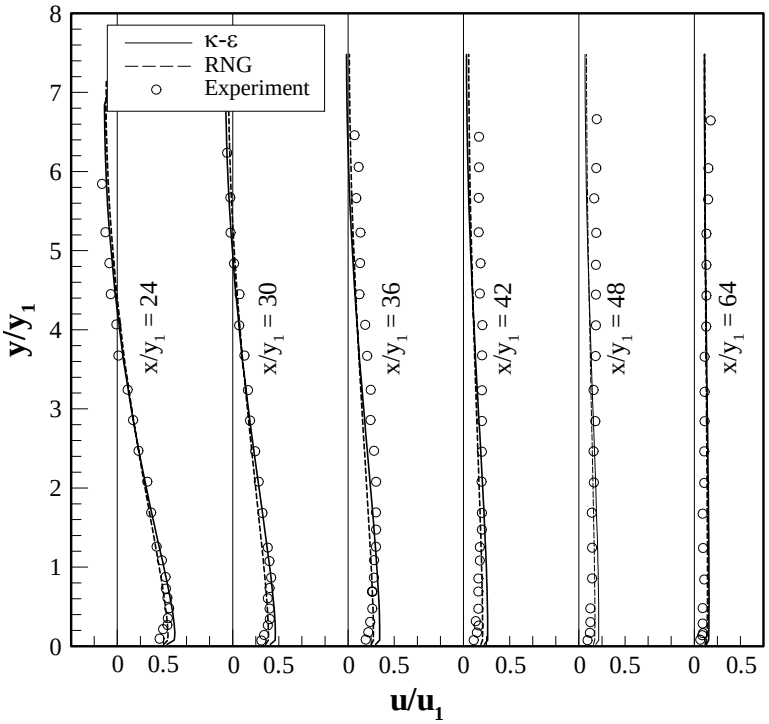

Figure 3.9: Longitudinal Velocity Profiles for Test 1
for $x/y_1 = 24 - 64$ ($F_1 = 3.19, S = 0.85$)

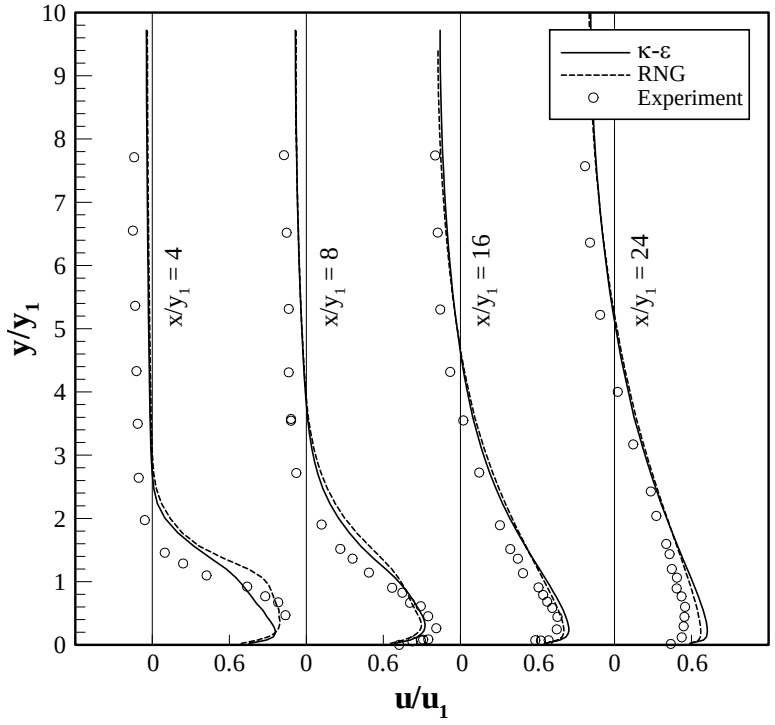

Figure 3.10: Longitudinal Velocity Profiles for Test 2
for $x/y_1 = 4 - 24$ ($F_1 = 5.49, S = 0.63$)

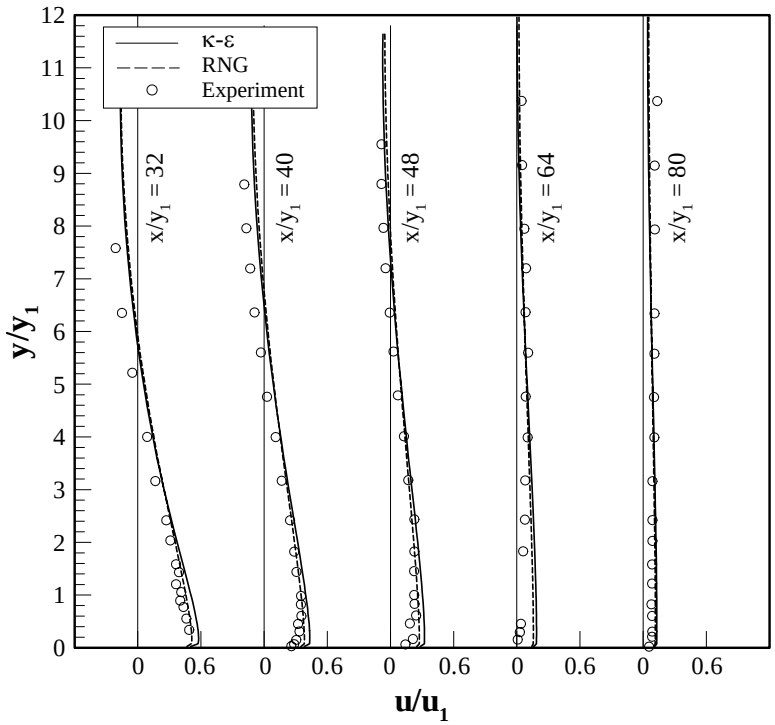

Figure 3.11: Longitudinal Velocity Profiles for Test 2
for $x/y_1 = 32 - 80$ ($F_1 = 5.49, S = 0.63$)

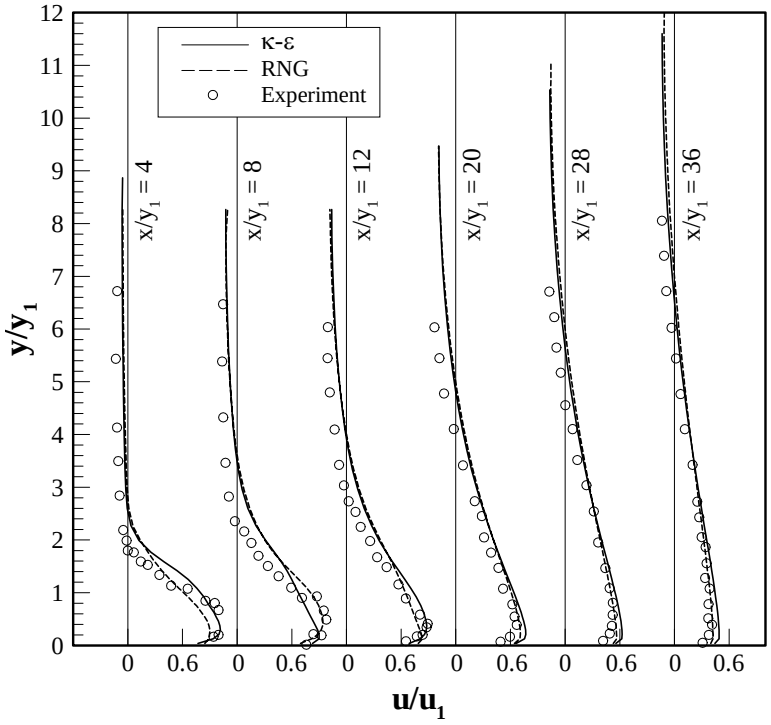

Figure 3.12: Longitudinal Velocity Profiles for Test 3 for $x/y_1 = 4 - 36$ ($F_1 = 8.19$, $S = 0.24$)

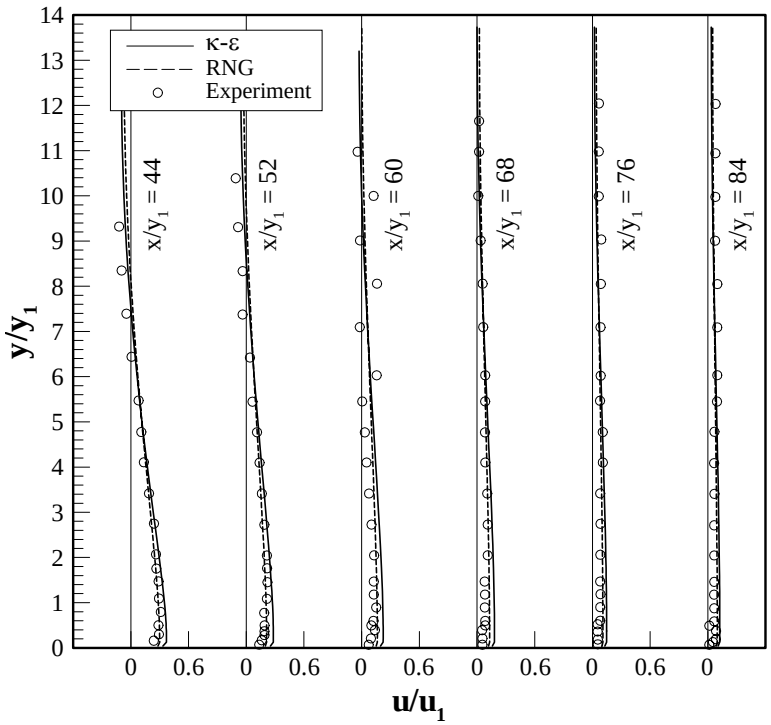

Figure 3.13: Longitudinal Velocity Profiles for Test 3 for $x/y_1 = 44 - 84$ ($F_1 = 8.19$, $S = 0.24$)

Next, the computed and measured results of vertical velocity profiles across the flow depth at various locations along the channel are shown in Figs. 3.14 – 3.19 for the three test cases. The computed results for the vertical velocity profiles do not follow the experimental data accurately near the gate (x/y_1 less than 24). In some cases, computed and measured data have opposite sign in this region. However, it should be realized that the magnitude of the vertical velocity is small within this zone. Also, Long (1991) pointed out that there could be as much as 100% error in the vertical velocity measurements and the flow at the gate had slightly downward velocity. These factors may contribute to large discrepancy between the computed and measured vertical velocity profiles near the gate.

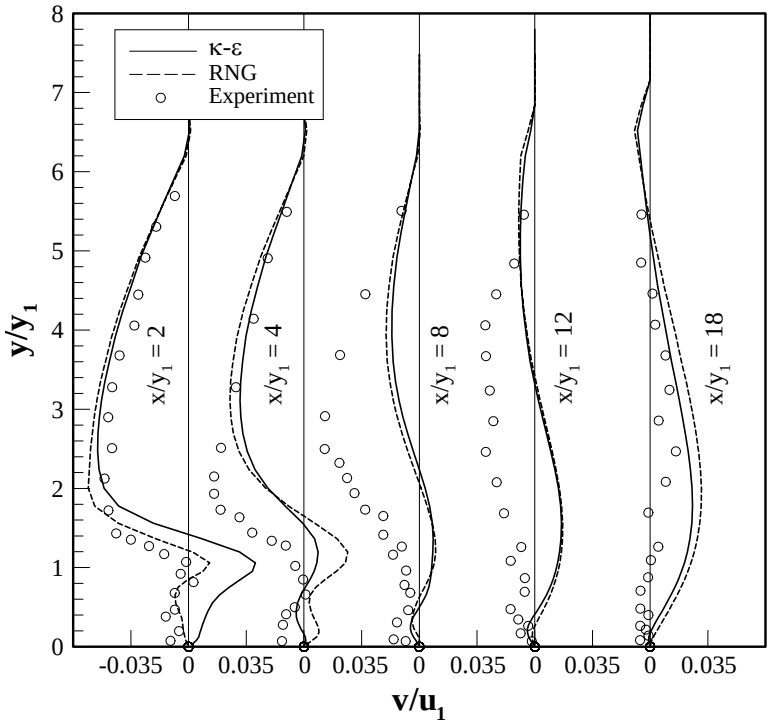

Figure 3.14: Vertical Velocity Profiles for Test 1
for $x/y_1 = 2 - 18$ ($F_1 = 3.19, S = 0.85$)

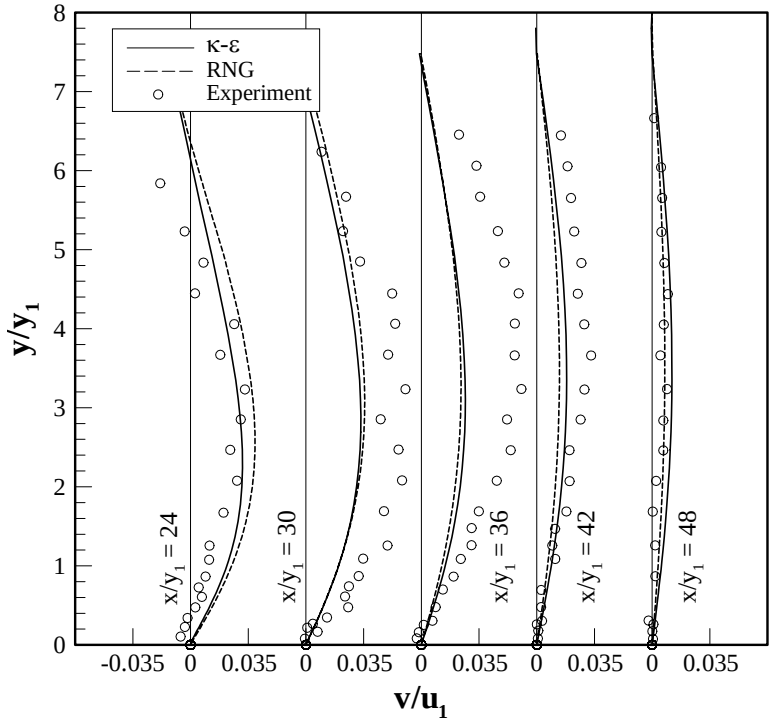

Figure 3.15: Vertical Velocity Profiles for Test 1
for $x/y_1 = 24 - 48$ ($F_1 = 3.19, S = 0.85$)

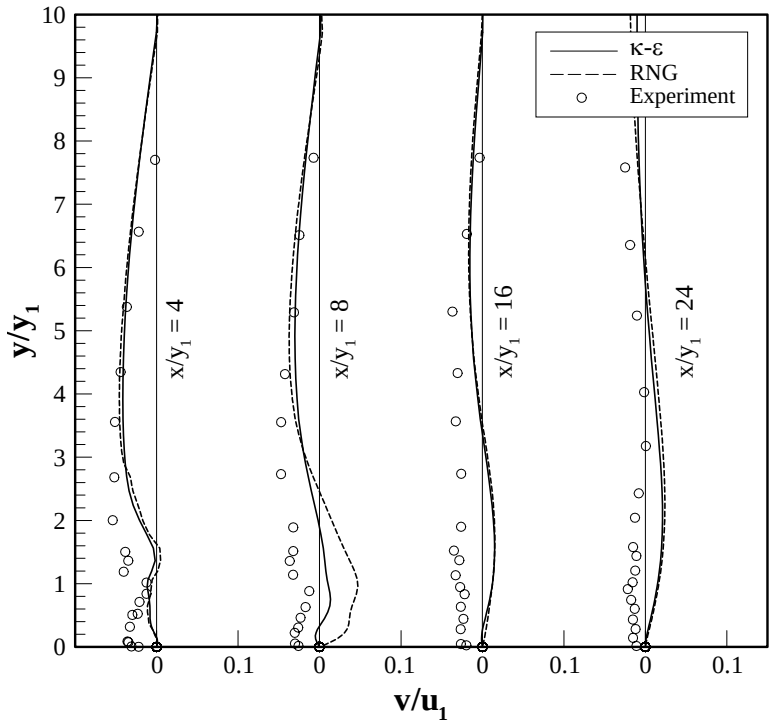

Figure 3.16: Vertical Velocity Profiles for Test 2
for $x/y_1 = 4 - 24$ ($F_1 = 5.49, S = 0.63$)

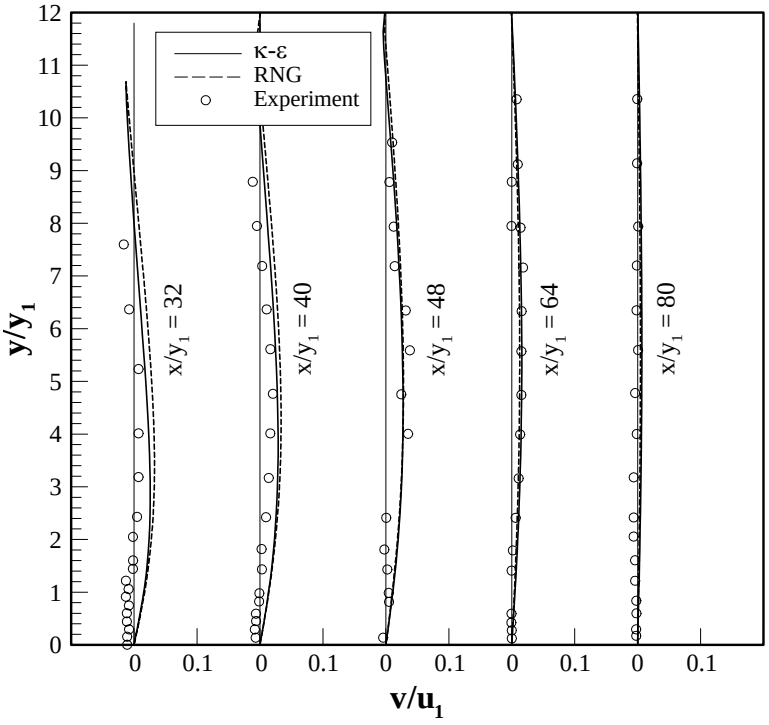

Figure 3.17: Vertical Velocity Profiles for Test 2
for $x/y_1 = 32 - 80$ ($F_1 = 5.49, S = 0.63$)

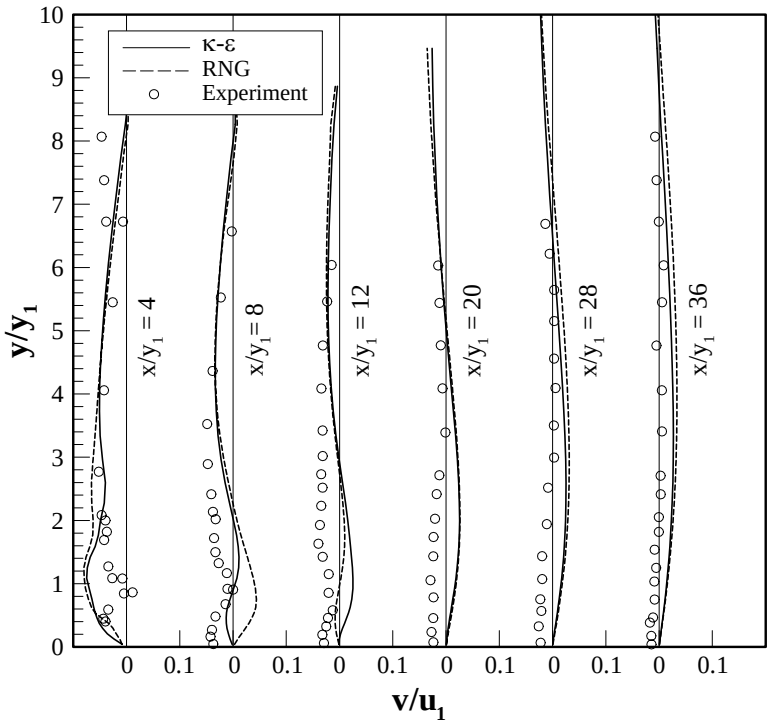

Figure 3.18: Vertical Velocity Profiles for Test 3
for $x/y_1 = 4 - 36$ ($F_1 = 8.19, S = 0.24$)

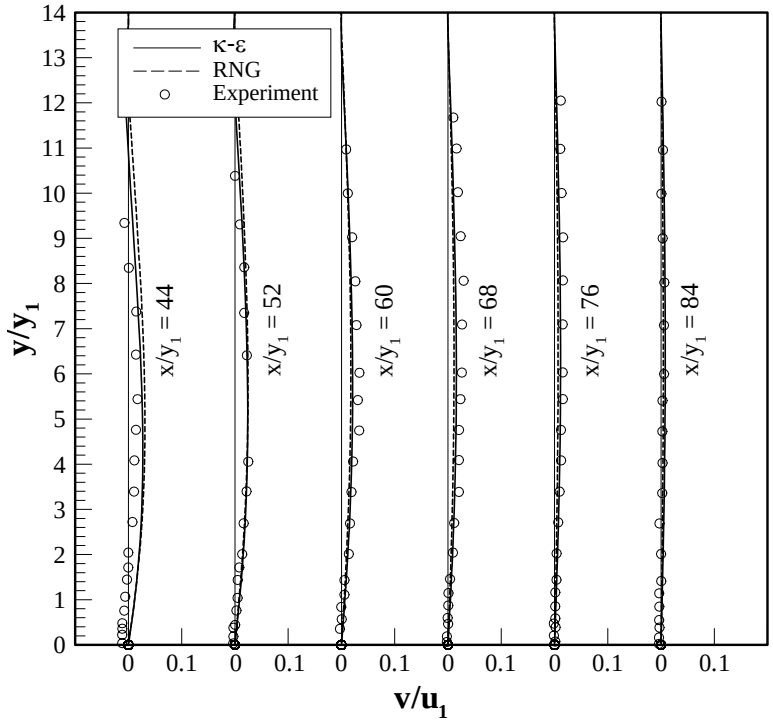

Figure 3.19: Vertical Velocity Profiles for Test 3
for $x/y_1 = 44 - 84$ ($F_1 = 8.19$, $S = 0.24$)

Comparisons of computed and measured vertical profiles of kinetic energy per unit mass at different locations along the channel length are shown in Figs. 3.20 – 3.25. Near the gate, the computed locations of maximum kinetic energy are higher than the measured locations, although, the computed and measured kinetic energy profiles show similar trend. In the downstream region, the computed kinetic energy profiles are accurately predicted by the two turbulent closure schemes throughout the whole depth.

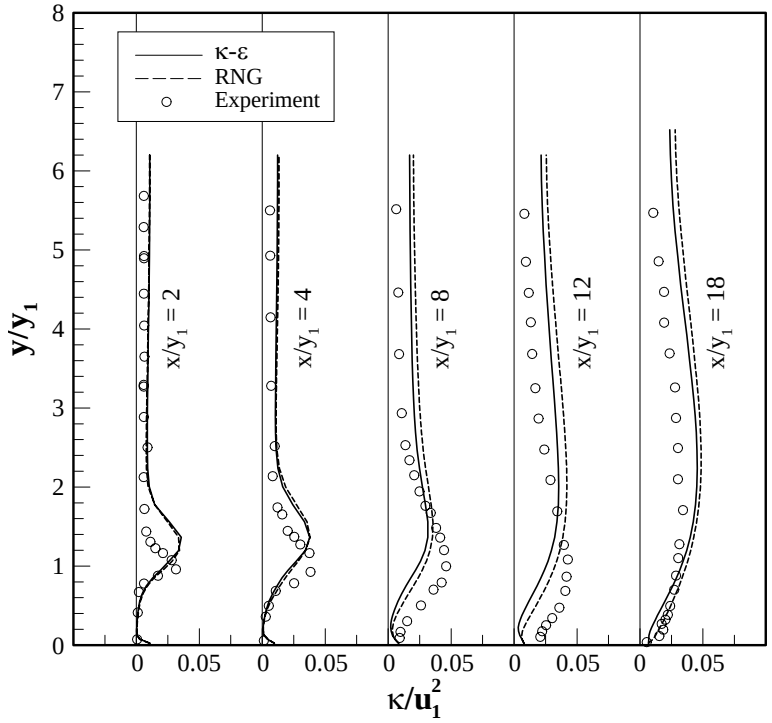

Figure 3.20: Turbulent Kinetic Energy Profiles for Test 1 for $X/Y_1 = 2 - 18$ ($F_1 = 3.19$, $S = 0.85$)

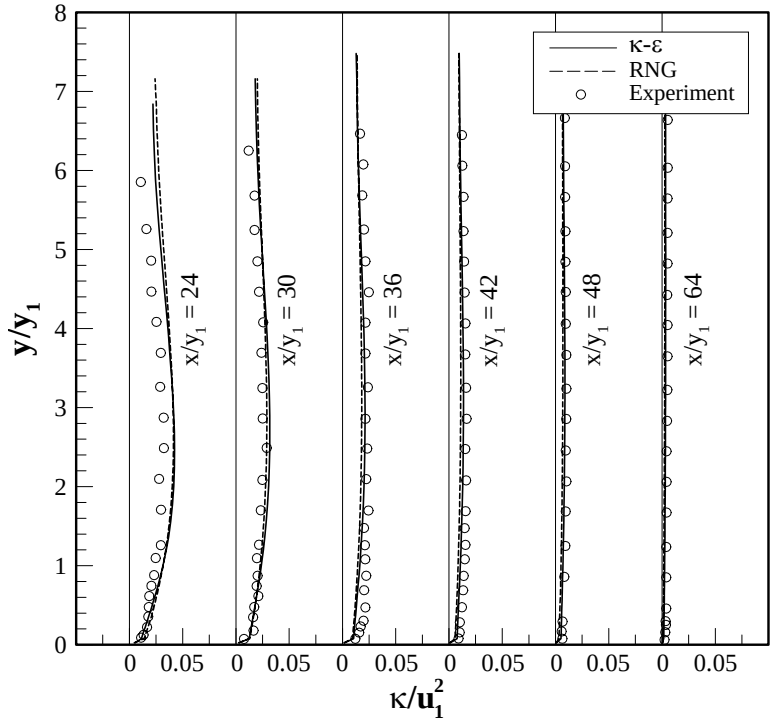

Figure 3.21: Turbulent Kinetic Energy Profiles for Test 1 for $X/Y_1 = 24 - 64$ ($F_1 = 3.19$, $S = 0.85$)

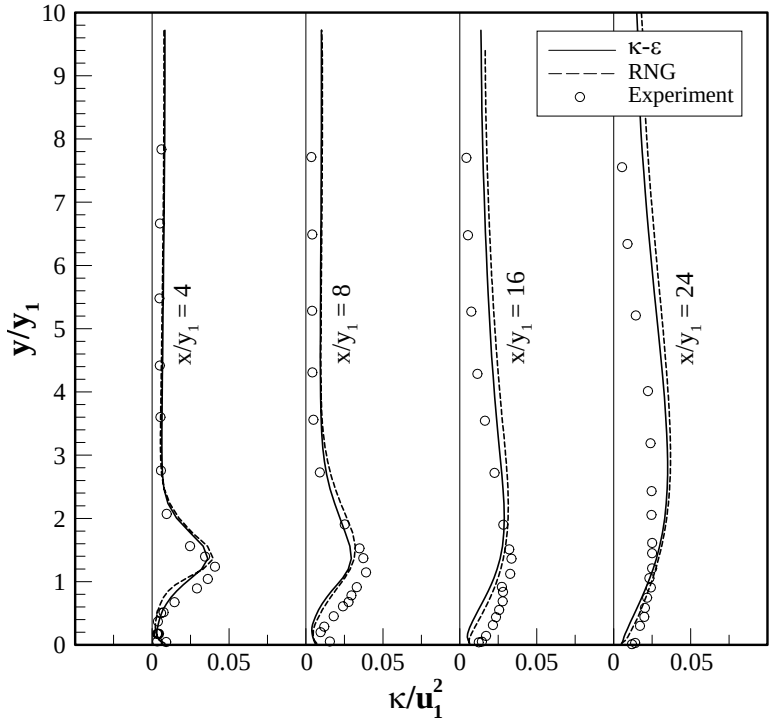

Figure 3.22: Turbulent Kinetic Energy Profiles for Test 2 for $X/Y_1 = 4 - 24$ ($F_1 = 5.49$, $S = 0.63$)

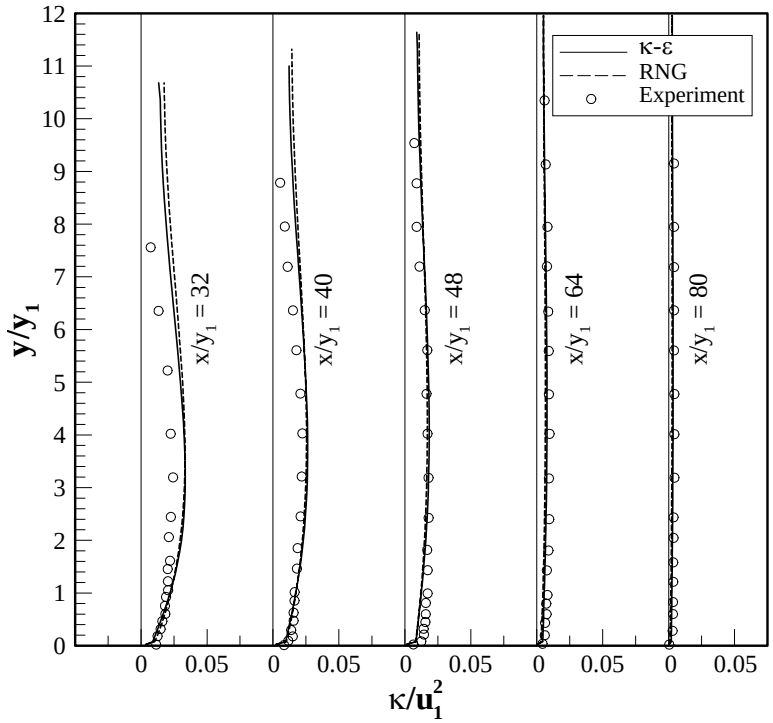

Figure 3.23: Turbulent Kinetic Energy Profiles for Test 2 for $x/y_1 = 32 - 80$ ($F_1 = 5.49$, $S = 0.63$)

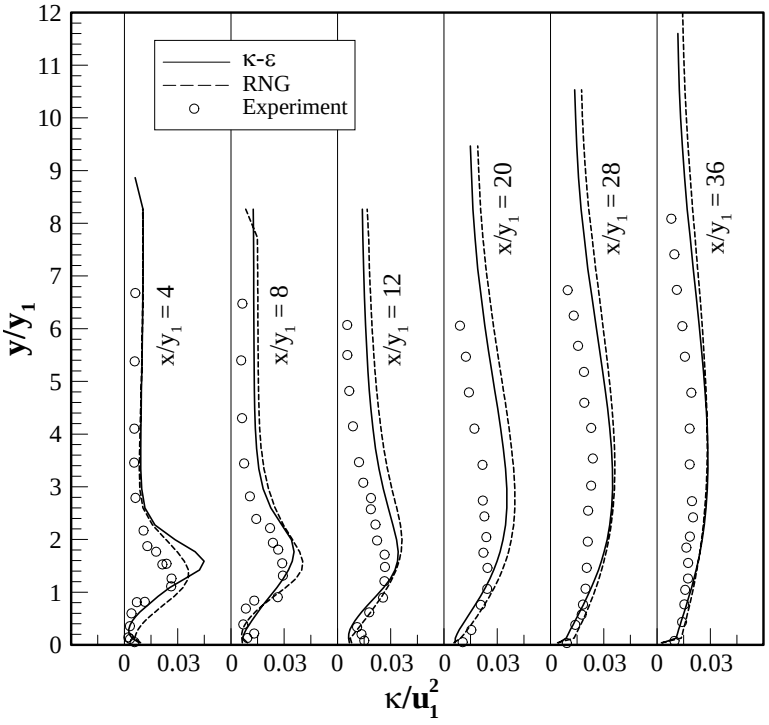

Figure 3.24: Turbulent Kinetic Energy Profiles Profiles for Test 3 for $x/y_1 = 4 - 36$ ($F_1 = 8.19$, $S = 0.24$)

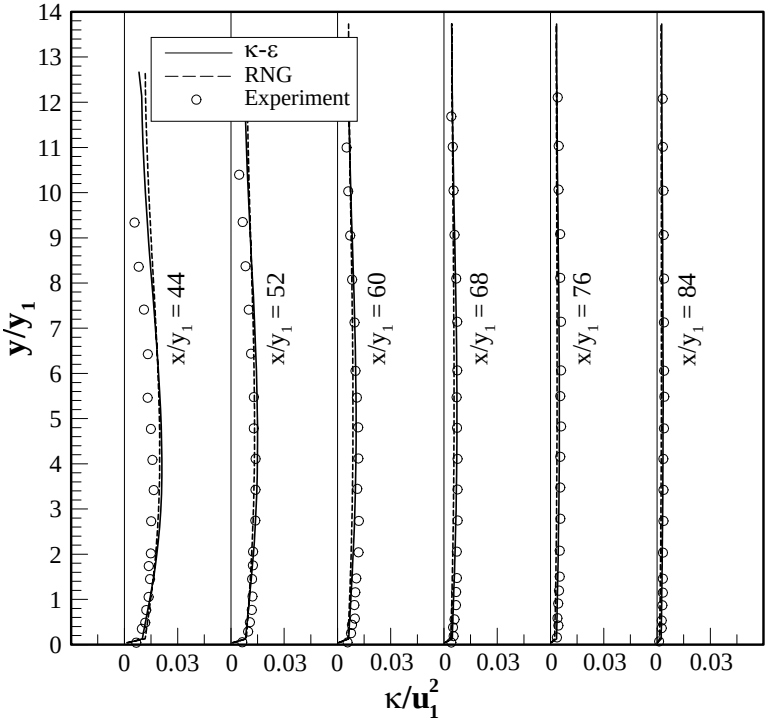

Figure 3.25: Turbulent Kinetic Energy Profiles for Test 3 for $x/y_1 = 44 - 84$ ($F_1 = 8.19$, $S = 0.24$)

Conclusions

The accuracy of the $k-\varepsilon$ and RNG turbulent closure schemes (with standard coefficients) in modeling a submerged hydraulic jump is assessed by comparing the computed mean and turbulent flow properties with the measured data of Long (1991). A three-dimensional flow model, Flow-3D, which has options for these two closure schemes is used to simulate three different cases of submerged hydraulic jump. The three test cases involve increasing Froude number and reducing submergence ratio. The computed water surface profile is accurately predicted by both schemes for the low Froude number and high submergence. However, the computed results over predict the measured water surface profiles for the higher Froude numbers. In all cases, the water surface profiles downstream of jumps are predicted accurately by both schemes.

The location and magnitude of maximum longitudinal velocity is predicted more accurately by the RNG scheme. Also the RNG scheme provides better estimate of the longitudinal velocities near the bed. The velocities in the shear layer above the gate and the depths at which the reverse velocities begin are over predicted by both schemes, especially for the lowest Froude number. The computed longitudinal velocity profiles are predicted accurately over the whole depth beyond x/y_1 of 12. The magnitude and longitudinal extent of the reverse velocities are computed accurately by both schemes.

The accuracy of the computed vertical velocity profiles could not be ascertained due to measurement errors and downward velocity component at the inlet. The computed kinetic energy per unit mass profiles in the vertical direction

agrees well with the measured data downstream of the jump. Near the inlet, although the trend is computed accurately, the magnitude of the computed kinetic energy and its location above the bed are higher than the measured data.

The comparison the $k-\varepsilon$ and RNG turbulent closure schemes for the submerged hydraulic jump shows that RNG scheme performs better in predicting the mean flow properties of the flow. Both schemes perform similarly in predicting the turbulent flow properties. In general, the three-dimensional model performs better in predicting turbulent kinetic energy per unit mass and reverse velocities compared to the two-dimensional models used previously.

CHAPTER 4
NUMERICAL SIMULATION OF FLOW DOWNSTREAM OF LOCK AND DAM

A lock and dam structure is built for creating a reservoir and producing hydroelectricity while allowing movement of barge tows across the dam. Navigation is a major part of river usage throughout the world and provides economical means for transport of goods. However, flow releases from either the spillway or the power generating units of the dam may have an adverse effect on navigation, especially barge tows moving upstream. The J. H. Overton Lock and Dam located in the Red River, Louisiana, is shown in Fig. 4.1 as an example of a typical lock and dam structure. The major features downstream of a lock and dam structure include the inside wall or river wall (a rock pile in this case), the outside or guide wall, and the bed topography. The rock pile divides the channel into two, the left channel acts as an approach to the lock while the flow from the dam moves down the main channel on the right. A guide wall is located to the left of the rock pile and defines the other boundary of the approach channel to the lock. Under certain flow and water surface level conditions an eddy, and in some cases a series of eddies may form at the left side of the main channel near the entrance to the approach channel (Bravo, 1989; Khan and Wang, 2001). For example, the J. H. Overton Lock and Dam located in the Red River, Louisiana, has been plagued with navigation problems. The rotating current encountered by barge tows approaching the lock and dam have caused numerous delays and accidents

(some fatal). If the reverse flow is strong enough, sediment may be moved and deposited near the mouth of the lock entrance and can cause barge tows to run aground.

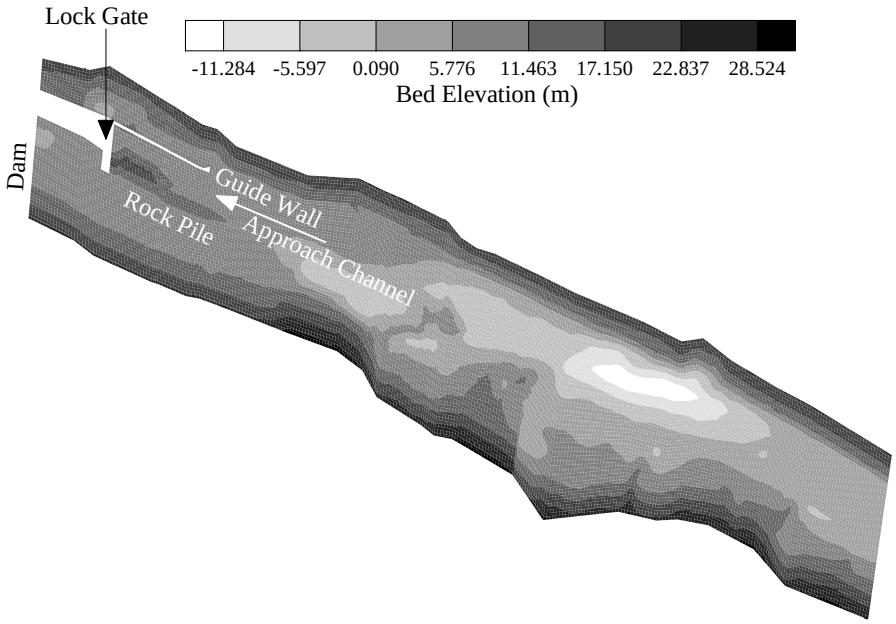

Figure 4.1: Layout of the J. H. Overton Lock and Dam.

The flow pattern downstream of a lock and dam structure can be investigated using physical models or computational models. Since each lock and dam structure has a unique bed topography, width of the approach channel, width of the main channel, length of the inside and outside walls bounding the approach channel, and outflow conditions from the dam, a physical model study is required for each scenario. Thus, it is necessary to study the flow pattern downstream of each lock and dam structure through a physical model or a computational model. A computational model that can accurately predict the flow pattern downstream

of a lock and dam can prove useful both during the design phase of a new structure and for the assessment of flow conditions downstream of existing structures. In addition, a computational model can be used to investigate the impact of the proposed training structures that may be employed to improve the flow pattern.

Bravo (1989) performed a detailed set of laboratory experiments on a 1:70 scale model of a lock and dam structure with gated spillway and powerhouse units. Flow patterns for various configurations of outflow and main channel width downstream of the structure were investigated. The impact of flow on the maneuverability of a barge tow model was also quantified. Various flow training structures were utilized to improve the flow conditions in the vicinity of the approach channel. Bravo and Holly (1996) reported a two dimensional, depth-averaged, turbulent flow model for simulation of flow conditions downstream of a lock and dam structure. The turbulent eddy viscosity was approximated using two different methods. As a first method, a constant eddy viscosity value was specified for the whole domain; a depth-averaged $k-\varepsilon$ scheme (two-equation model) was used as a second method. Both methods were found to be accurate with respect to the size and shape of the major recirculation zone. However, the magnitude of the reverse flow was not computed accurately (Bravo, 1989). Bravo and Holly (1996) preferred the use of $k-\varepsilon$ scheme as it eliminated the need of finding an appropriate value of eddy viscosity for every case.

In this study, CCHE2D, a two-dimensional, depth-averaged, free surface, turbulent flow model is used to simulate the flow pattern downstream of a lock

and dam structure. The eddy viscosity in the model is evaluated using three different closure schemes. The turbulent closure schemes evaluated are the depth-averaged parabolic eddy viscosity scheme, mixing length scheme, and $k-\varepsilon$ scheme. The computational model with various closure schemes is verified using the physical model data reported by Bravo and Holly (1996). The model is then used to simulate flow downstream of J. H. Overton Lock and Dam located in the Red River, Louisiana.

Governing Equations

The two-dimensional, depth-averaged mass and momentum conservation equations used in the CCHE2D model are

$$\frac{\partial h}{\partial t}+\frac{\partial hu}{\partial x}+\frac{\partial hv}{\partial y}=0 \tag{4.1}$$

$$\frac{\partial u}{\partial t}+u\frac{\partial u}{\partial x}+v\frac{\partial u}{\partial y}+g\frac{\partial \eta}{\partial x}=\frac{1}{\rho h}\frac{\partial h\tau_{xx}}{\partial x}+\frac{1}{\rho h}\frac{\partial h\tau_{xy}}{\partial y}-\frac{\tau_{bx}}{\rho h}+f_{cor}v \tag{4.2}$$

$$\frac{\partial v}{\partial t}+u\frac{\partial v}{\partial x}+v\frac{\partial v}{\partial y}+g\frac{\partial \eta}{\partial y}=\frac{1}{\rho h}\frac{\partial h\tau_{yx}}{\partial x}+\frac{1}{\rho h}\frac{\partial h\tau_{yy}}{\partial y}-\frac{\tau_{by}}{\rho h}+f_{cor}u \tag{4.3}$$

where h is the depth of flow, u and v are the depth-averaged velocities in the x and y directions, x and y are coordinate directions, t is time, ρ is the density of water, g is the gravitational acceleration, η is the water surface elevation from a reference level, τ_{xx} and τ_{yy} are the normal stresses in the x and y directions, τ_{xy} and τ_{yx} are the shear stresses in the x and y directions, τ_{bx} and τ_{by} are the bed shear stresses in the x and y directions, and f_{cor} is the Coriolis parameter.

The turbulent normal and shear stresses are evaluated using Boussinesq's assumption as follows

$$\tau_{xx} = 2\rho\nu_t \frac{\partial u}{\partial x} \tag{4.4}$$

$$\tau_{yy} = 2\rho\nu_t \frac{\partial v}{\partial y} \tag{4.5}$$

$$\tau_{xy} = \tau_{yx} = \rho\nu_t \left(\frac{\partial u}{\partial y} + \frac{\partial v}{\partial x} \right) \tag{4.6}$$

where ν_t is the depth-averaged turbulent kinematic eddy viscosity (eddy viscosity).

Turbulent Closure Schemes

Three different turbulent closure schemes are used to evaluate the depth-averaged turbulent eddy viscosity. The first turbulent closure scheme is based on the assumption of a parabolic vertical distribution of eddy viscosity (assuming a logarithmic velocity distribution), the depth-averaged eddy viscosity is given by

$$\nu_t = 0.17\kappa u_* h \tag{4.7}$$

where κ is the von Karman constant and u_* is the bed shear velocity. A depth-averaged mixing length scheme, as given by Rodi (1984), is modified as a second turbulent closure scheme and is given below

$$\nu_t = \ell^2 \left[2\left(\frac{\partial u}{\partial x} \right)^2 + 2\left(\frac{\partial u}{\partial y} + \frac{\partial v}{\partial x} \right)^2 + 2\left(\frac{\partial v}{\partial y} \right)^2 + \left(\frac{\alpha u_*}{\kappa h} \right)^2 \right]^{0.5} \tag{4.8}$$

where ℓ is the depth-averaged mixing length (equal to $0.267\kappa h$). The last term in the equation is added to retrieve the depth-averaged eddy viscosity value in cases where velocity gradients are zero and accounts for the turbulence generated from the bed. The coefficient α is chosen to retrieve Eq. 4.7 when the velocity gradients are zero. The variation of mixing length from the solid boundary is assumed to be parabolic (Jia and Wang, 1998). At the solid boundary the mixing length is zero and increases with the distance from the wall to a maximum value of $0.267\kappa h$ (a depth-averaged mixing length value assuming logarithmic velocity profile in vertical direction).

The last turbulent closure scheme investigated is the depth-averaged $k-\varepsilon$ scheme. It is a two-equation model, the equations, as given by Rodi (1984), are described below

$$\frac{\partial k}{\partial t}+u\frac{\partial k}{\partial x}+v\frac{\partial k}{\partial y}=\frac{\partial}{\partial x}\left(\frac{\nu_t}{\sigma_k}\frac{\partial k}{\partial x}\right)+\frac{\partial}{\partial y}\left(\frac{\nu_t}{\sigma_k}\frac{\partial k}{\partial y}\right)+P_h+P_{kV}-\varepsilon \tag{4.9}$$

$$\begin{aligned}&\frac{\partial \varepsilon}{\partial t}+u\frac{\partial \varepsilon}{\partial x}+v\frac{\partial \varepsilon}{\partial y}=\frac{\partial}{\partial x}\left(\frac{\nu_t}{\sigma_s}\frac{\partial \varepsilon}{\partial x}\right)+\frac{\partial}{\partial y}\left(\frac{\nu_t}{\sigma_s}\frac{\partial \varepsilon}{\partial y}\right)\\&+C_{1s}\frac{\varepsilon}{k}P_h\nu-C_{2s}\frac{\varepsilon^2}{k}\end{aligned} \tag{4.10}$$

where

$$P_h=\nu_t\left[2\left(\frac{\partial u}{\partial x}\right)^2+2\left(\frac{\partial v}{\partial y}\right)^2+\left(\frac{\partial u}{\partial y}+\frac{\partial v}{\partial x}\right)^2\right] \tag{4.11}$$

$$P_{kV}=C_k\frac{u_*^3}{h};\quad P_{\varepsilon V}=C_\varepsilon\frac{u_*^4}{h^2} \tag{4.12}$$

$$C_k = \frac{h^{1/6}}{n\sqrt{g}}; \quad C_\varepsilon = 3.6\frac{h^{1/4}}{n^{3/2}g^{3/4}}C_{2\varepsilon}\sqrt{C_\mu} \tag{4.13}$$

$$\nu_t = C_\mu \frac{k^2}{\varepsilon} \tag{4.14}$$

n is the Manning's roughness coefficient, u_* is the resultant shear velocity based on bed shear stresses τ_{bx} and τ_{by}, and $\sigma_k, \sigma_\varepsilon, C_{1\varepsilon}, C_{2\varepsilon}, C_\mu$ are empirical constants and are given by Rodi (1984) as 1.0, 1.3, 1.44, 1.92, and 0.09, respectively.

Numerical Scheme

The CCHE2D model employs the efficient element, implicit, numerical scheme to solve the momentum equations. The scheme requires a quadrilateral, non-orthogonal, structured mesh system. A diagram of the computational mesh used is given in Appendix F. A working element is formed around each node and consists of a central node (the node at which the variables are calculated) and eight surrounding nodes. Quadratic interpolation functions are used to approximate the variation of variables and its derivatives. The continuity equation is solved for water surface elevation by drawing a control volume around the central node of each element and using the control volume approach to approximate the mass fluxes entering and leaving the control volume. The method guarantees mass conservation through the computational domain. Complete details of the scheme are given by Wang and Hu (1992) and Jia and Wang (1999).

Model Validation

The CCHE2D model with three turbulent closure schemes is validated against the measured velocity in a physical model study of a lock and dam (geometric scale ratio of 1:70) conducted by Bravo (1989). The setup of the test is shown in Fig. 4.2. The complete details of the test (labeled as A-A-6-9-400-0) are provided by Bravo (1989). A spillway 146.3-m (480-ft) long is located in the middle of the channel at the upstream end. The spillway crest is at 18.29-m (60-ft) elevation and the base of the spillway is at 13.41-m (44-ft) elevation. There are 6 power generating units at the right side of the spillway and 2 power generating units at the left side of the spillway. Each unit is 18.29-m (60-ft) wide and 9.14-m (30-ft) high. The downstream trapezoidal channel is 121.92-m (400-ft) wide at the base. Two walls are located at the left side of the channel. The inside wall separates the main channel from the lock and is 249.94-m (820-ft) long and the outside wall is 432.82-m (1,420-ft) long. The channel bed elevation and side slope of the channel walls are shown in Fig. 4.2.

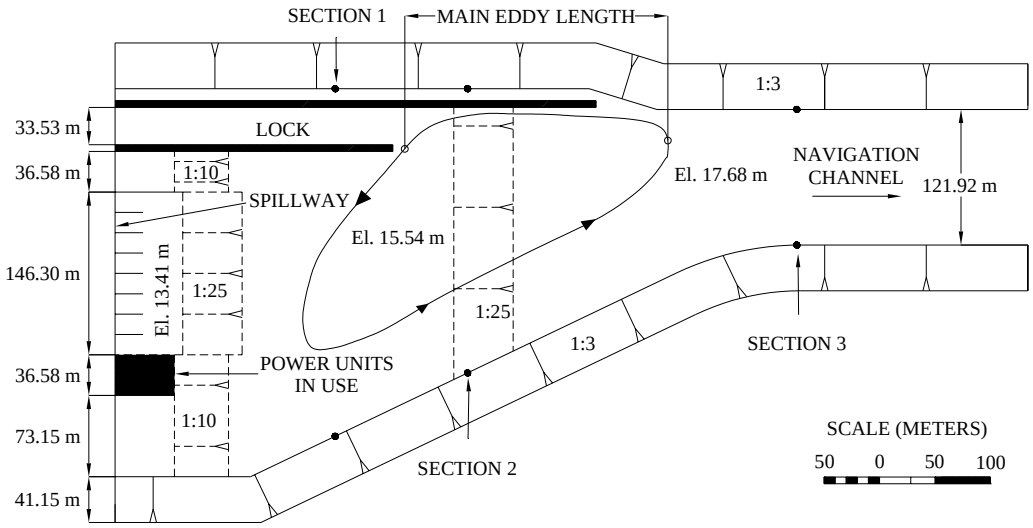

Figure 4.2: Layout of the Physical Model

At the upstream end, a flow rate of 652.93 cubic meters per second (23,058 cfs) was prescribed and was equally divided between the first two power units to the right of the spillway. A tail gate was used to control the downstream depth and was set at 2.74 m (9 feet). The channel bed and side walls were finished with cement mortar and Strickler's friction coefficient of 40 was used.

Three major recirculation zones (eddies) were observed in the physical model study. The first recirculation zone spanned across the entrance to the lock, the second eddy developed upstream of the first in the river near the inside wall, and the third eddy formed to the right of the discharging power units. The length of the first eddy measured from the downstream end up to the end of the inside wall was 165 m and the maximum reverse velocity was found to be 0.8 m/s. The velocity profiles were measured across the channel at three locations along the length of the channel. The locations of the measured velocity profiles are shown in Fig. 4.2.

The flow rate at the upstream end and the flow depth at the downstream end are applied to simulate the flow condition in the channel using the depth-averaged model. The Manning's roughness coefficient of 0.013 is used for the specified channel surface. The simulated velocity profiles using the three turbulent closure schemes are compared to the measured velocity profiles in Figs. 4.3, 4.4 and 4.5. The results show that the depth-averaged parabolic eddy viscosity scheme performs poorly in predicting both the extent and magnitude of the reverse flow, while the depth-averaged mixing length and $k-\varepsilon$ schemes perform satisfactorily. At the third section downstream of the recirculation zones, Fig. 4.5, all three schemes provide similar results. Figures 4.6 and 4.7 show the streamlines generated based on the results computed using the depth-averaged parabolic eddy viscosity and $k-\varepsilon$ schemes, respectively. Figure 4.6 shows that the eddy pattern and location are not computed accurately when the depth-averaged parabolic eddy viscosity scheme is used. Figure 4.7 shows that the $k-\varepsilon$ scheme is capable of simulating both the location and pattern of the main eddy. The length of the major eddy (an eddy spanning across the lock entrance) is found to be 170 m, which matches closely with the reported value of 165 m. In addition, a clockwise eddy upstream of the main eddy and a clockwise eddy on the right side of the inflow are predicted. These eddies are also reported by Bravo (1989). The depth-averaged mixing length scheme provides results very similar to the $k-\varepsilon$ scheme.

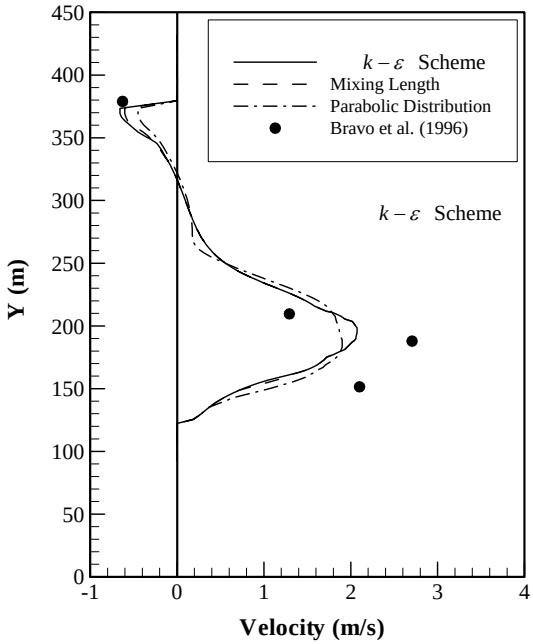

Figure 4.3: Comparison of Velocity Files at Section 1

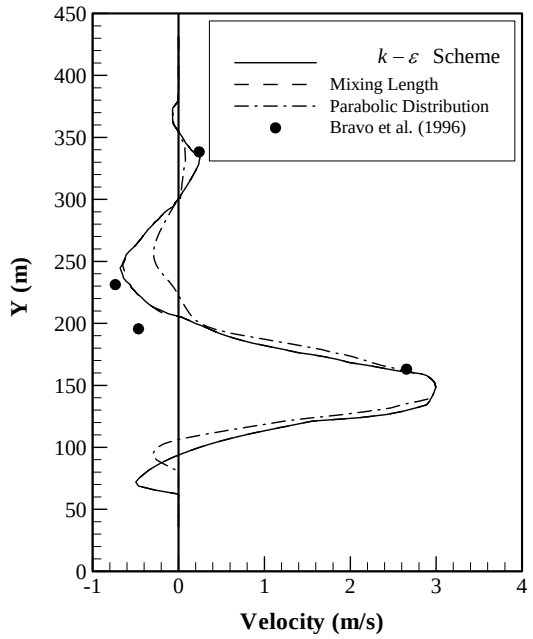

Figure 4.4: Comparison of Velocity Profiles at Section 2

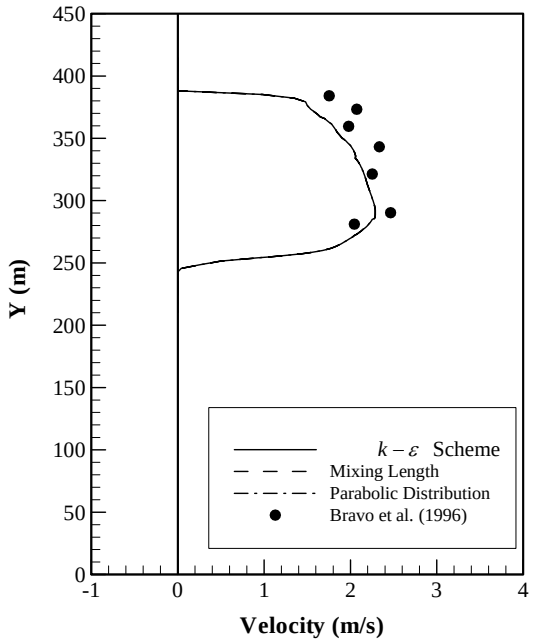

Figure 4.5: Comparison of Velocity Profiles at Section 3

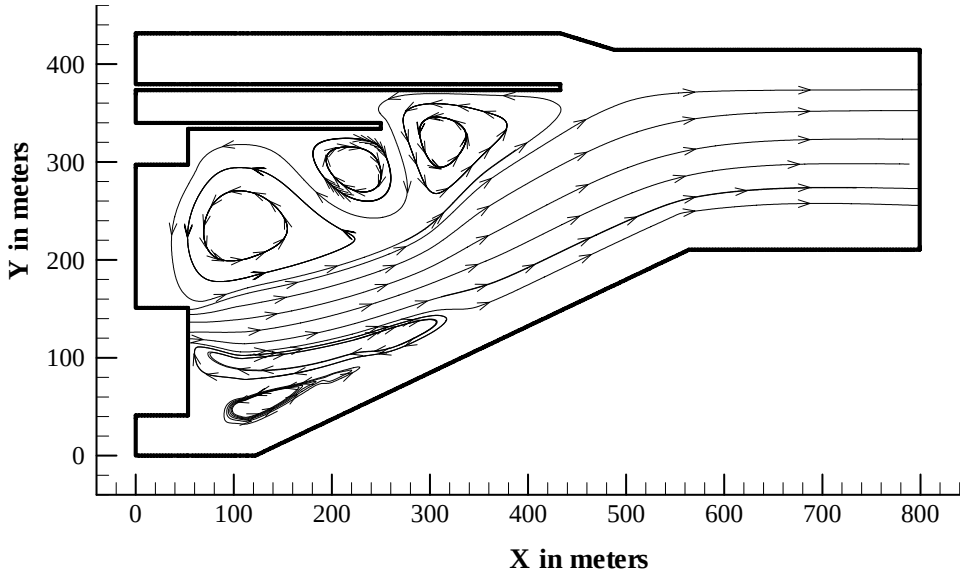

Figure 4.6: Streamlines Pattern using the Parabolic Eddy Viscosity Scheme

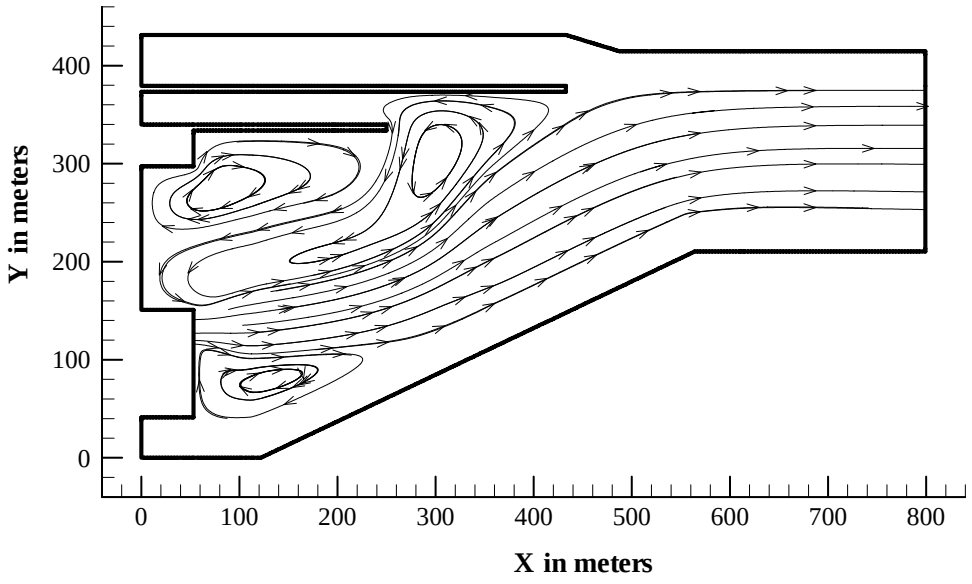

Figure 4.7: Streamlines Pattern using the $k-\varepsilon$ Scheme

The comparison of eddy viscosity profiles from the three turbulent closure schemes at the three locations marked in Fig. 4.2 are shown in Figs. 4.8, 4.9, and 4.10. At sections 1 and 2, the eddy viscosity results from the mixing length and the parabolic schemes differ from the $k-\varepsilon$ scheme in the recirculation zones. However in the main flow region, all three schemes provide similar results for the eddy viscosity. At section 3, the three schemes provide similar results for the eddy viscosity profile across the channel. From these results it is clear that the $k-\varepsilon$ scheme should be preferred; however, in some cases other lower order schemes may provide similar results and prove efficient, especially where long river reaches are to be modeled.

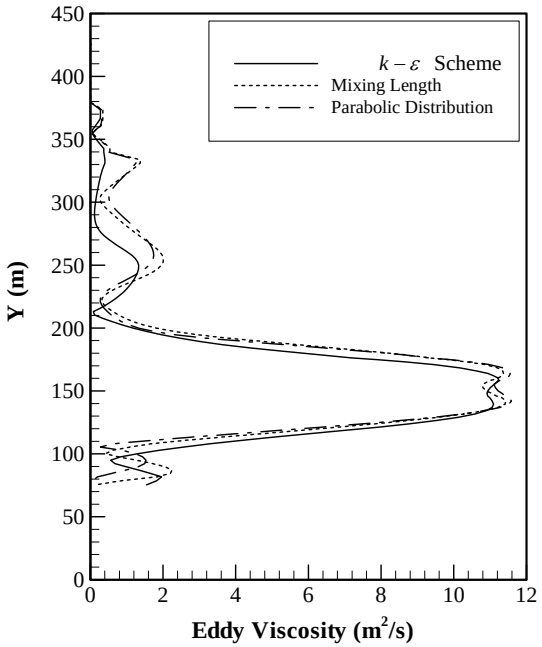

Figure 4.8: Comparison of Eddy Viscosity Profiles at Section 1

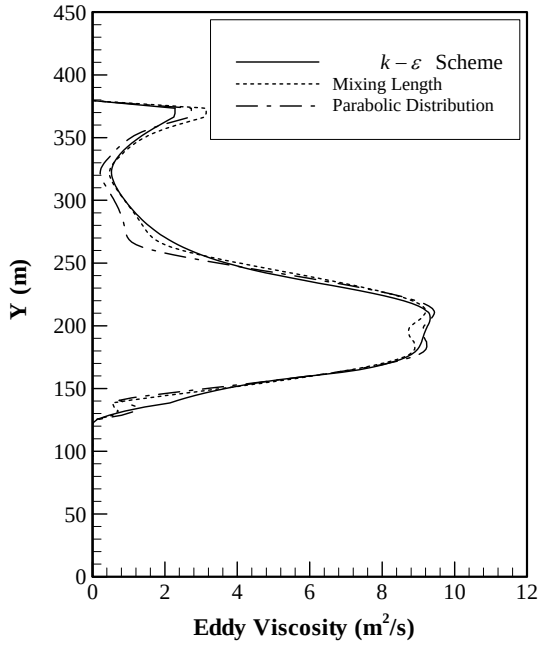

Figure 4.9: Comparison of Eddy Viscosity Profiles at Section 2

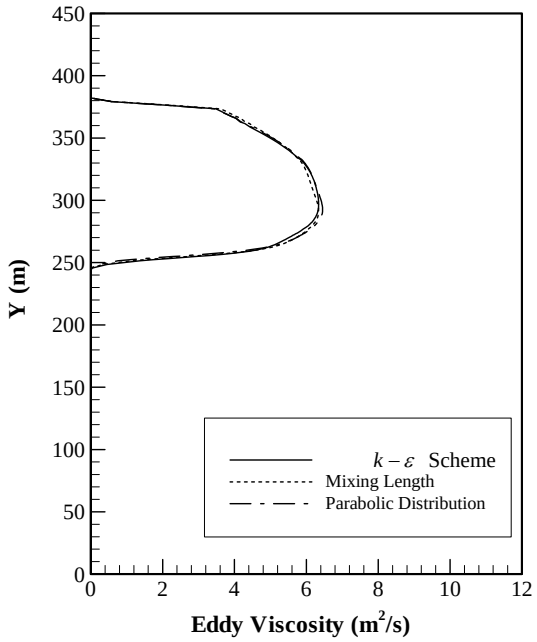

Figure 4.10: Comparison of Eddy Viscosity Profiles at Section 3

Field Test

The aim of this field test is to quantify the flow characteristics that are causing navigational problems downstream of J. H. Overton Lock and Dam in the Red River, Louisiana. The dam, lock channel, and the downstream channel along with the bed topography are shown in Fig. 4.1. The dam is located at the upstream end. The rock pile divides the channel into two, the channel on the left acts as an approach channel to the lock gate, while the flow from the dam moves down the right channel. The upstream half of the rock pile dike is always exposed, while the lower half has a crest elevation of 15.24 m (50 feet) and is submerged for the water surface elevation considered in this study. A guide wall is located to the left of the rock pile and defines the outer boundary of the approach channel. Two scour holes, one immediately downstream of the rock

pile and another further downstream, near the left bank, can be clearly identified and shows the path of the main flow.

Field observations found a recirculating flow reaching all the way upstream to the mouth of the lock approach channel. Several accidents, some fatal, have been reported as barge tows approach the lock hugging the left bank of the channel. A secondary problem is created by sediment build up in the quiescent zone and has caused barge tows to run aground.

Two different flow scenarios were simulated using the CCHE2D model. In the first case called the low flow condition, a downstream water surface level of 16.9 m (55.4 ft) was specified and a discharge of 2265.4 cubic meters per second (about 80,000 cfs) at the upstream end of the channel was applied as outflow from the dam. In the second case called the high flow condition, a water surface level of 18.38 m (60.3 ft) was specified at the downstream end and a discharge of 3058.22 cubic meters per second (about 108,000 cfs) was prescribed as an outflow from the dam. The low flow condition reflected the worst condition for navigation. The Manning's roughness coefficient of 0.03, based on the bed material size, was used for the simulation in both cases. Both the depth-averaged mixing length and $k-\varepsilon$ schemes were used to simulate the flow pattern in the channel.

The streamlines obtained from the results using the depth-averaged $k-\varepsilon$ model are shown in Figs. 4.11 and 4.12 for the low and high flow conditions, respectively. In both cases, a high velocity flow region through the downstream channel can be identified. The streamlines show the extent of the recirculation

zones with the main recirculation zone extending up to the mouth of the approach channel. The strength of the main eddy at five points, labeled in Figs. 4.11 and 4.12, are investigated for the high and low flow conditions. The five points are located at the same locations in the two cases. The velocities at points 1, 2, 3, 4, and 5 for the low flow condition are 0.56 m/s, 0.32 m/s, 0.08 m/s. 0.06 m/s, and 0.05 m/s, respectively. Under the high flow condition, the velocities are 0.71 m/s, 0.4 m/s, 0.12 m/s, 0.072 m/s, and 0.06 m/s. Point 1 represents the maximum velocity in the main eddy. It is clear that the strength of the eddy increases as the flow increases. However, the length (along the flow direction) and the width (across the flow) of the main eddy reduce as the flow increases. The length and width of the eddy being 712 m and 98 m under the low flow condition and 621 m and 90 m under the high flow condition.

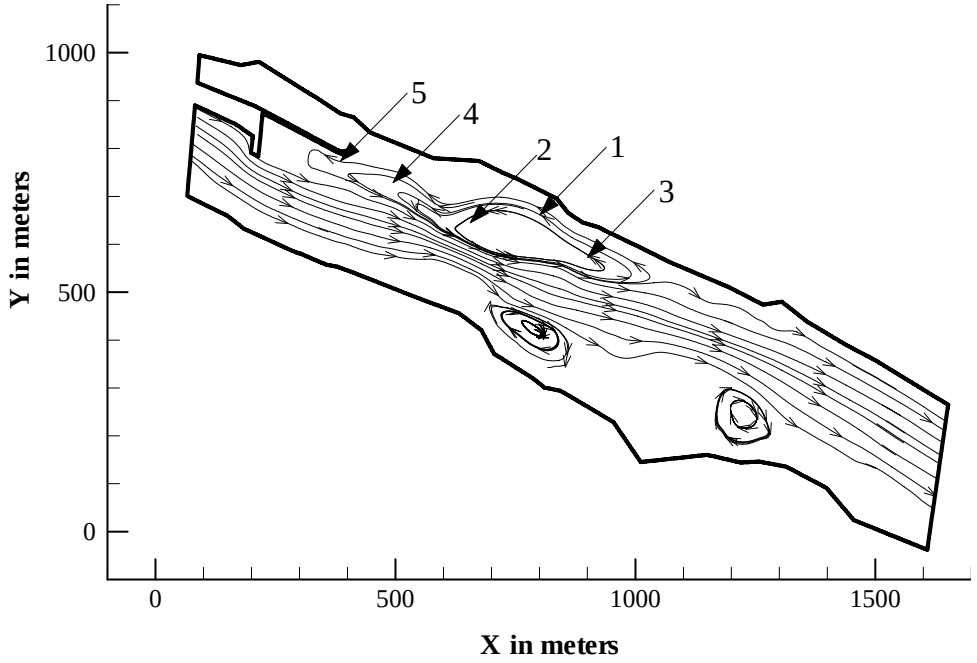

Figure 4.11: Streamlines Pattern for the Low Flow Condition
(J. H. Overton Lock and Dam)

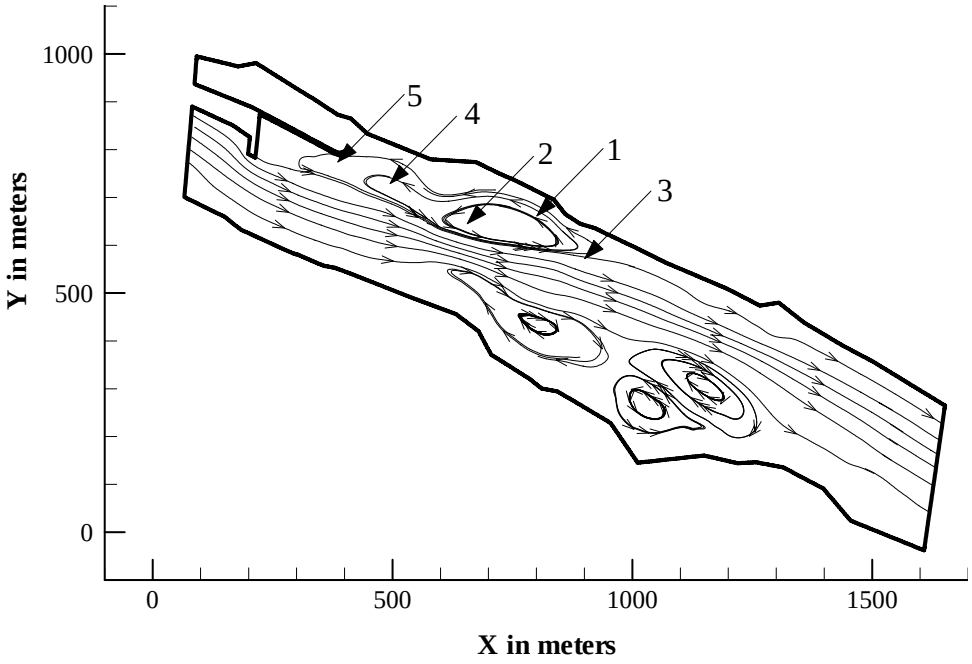

Figure 4.12: Streamlines Pattern for the High Flow Condition
(J. H. Overton Lock and Dam)

Under the low flow or worst navigation condition, the strength and size of the main eddy were measured with floats. It was found that the maximum strength of the eddy was 0.61 m/s and it extended up to the approach channel. In addition, the downstream extremity of the main eddy corresponds well with field observations. The results from the present study compare well with field observations.

The results show that the eddy on the left side of the channel is the main cause of the navigation problems encountered. A barge tow moving towards the approach channel along the left bank of the channel would suddenly experience a sharp velocity gradient at the junction of forward moving and recirculating flow zones, thus creating navigational hazard.

Summary and Conclusions

A two-dimensional, depth-averaged, turbulent flow model with three different turbulent closure schemes is used to simulate the flow conditions in channels downstream of lock and dams. The major emphasis is to evaluate the capability of the turbulent closure schemes in modeling the recirculation zones that develop in the downstream channel. The accuracy in determining the size and strength of the main eddy are the main parameters of validation. The depth-averaged parabolic eddy viscosity scheme, mixing length scheme, and $k-\varepsilon$ scheme are employed in this study. The results of the velocity profiles across the channel, at different locations along the channel, obtained using the three turbulent closure schemes are compared to the measured data from a physical model study of a lock and dam. The results show that the mixing length and $k-\varepsilon$ schemes perform well in predicting the velocity profiles. In addition, these two schemes accurately predict, the size, shape, and location of eddies found in the physical model study. However, the eddy viscosity profiles across the channel in the recirculation zone, computed using mixing length scheme, differ from that predicted using the $k-\varepsilon$ scheme.

The model is then applied to simulate flow patterns for the low and high flow conditions downstream of a lock and dam in the Red River, Louisiana. The results, using the mixing length and $k-\varepsilon$ schemes, show that the main features of the flow in the downstream channel can be satisfactorily simulated. The strength and length of the main eddy for the low flow condition compare well with observations made in the field. The results show that as the flow increases

the strength of the main eddy increases, however the length and width of the eddy reduce.

The results from the two tests conducted in this study show that the modified mixing length turbulent closure scheme, though simple, can be used to predict flow features in the channel downstream of a lock and dam. However, the results are specific to this study and the applicability of the mixing length model must be verified against the $k-\varepsilon$ scheme for other applications.

CHAPTER 5
EXPERIMENTAL MEASUREMENTS OF SHALLOW NEAR BED JETS

Many industries and municipalities release effluent into our lakes, streams and rivers. The releases can be broadly categorized as jets. If pollutants, in the form of heat or particulates, are released, some environmental regulations require them to be diluted within a certain distance downstream of the discharge point. Current dilution calculations assume that these releases mix with the ambient fluid and dilute in a way consistent with a free jet, or a jet in an ambient fluids of infinite extent. However, most effluent discharges enter shallow streams or rivers where boundaries may affect these mixing characteristics. A better understanding is needed of how the mixing characteristics of a jet are affected by the presence of boundaries. A large body of research has been performed on free jets, jets near or at the bed (wall jets), as well as on jets at or near the surface (surface jets). However few researchers have looked at the influence of both boundaries together. A definition sketch is shown in Fig. 5.1 of each of the four jet geometries.

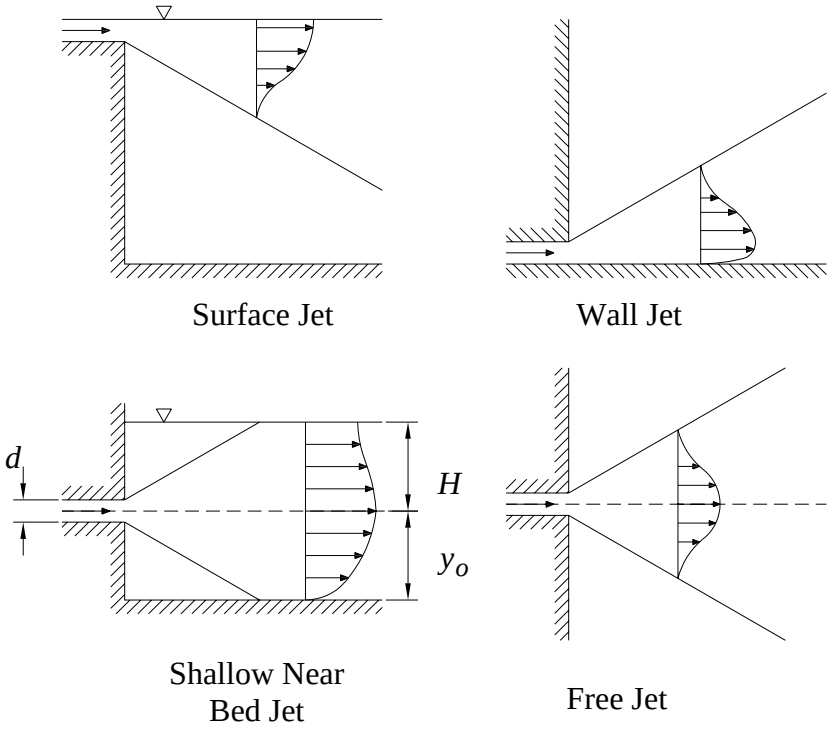

Figure 5.1: Schematic of Jet Geometries in Vertical Plane

Shallow near bed jets are normally classified based on their submergence ratio, H/d, offset ratio, y_o/d, and entrance Froude number, where H and y_o are defined in Fig. 5.1. One interesting property of these jets is their attachment to one boundary or the other causing the point of maximum velocity to deviate from the nozzle centerline. Johnston and Halliwell (1986) describe different attachment regimes that may be classified broadly as surface and bed attachment. In some cases both regimes may exist for identical tail water conditions. Large submergence ratios produce bed attached jets while very shallow jets attach to the surface. Johnston (1985) performed experiments at offset ratios of 3, 4 and 5 for Froude numbers of 4 – 32 and submergence ratios of 1 – 11. Using these results a map of attachment regimes based on submergence and Froude number was

produced. The results also showed that shallow jets produce less dilution than free jets at the same location. In a later study on buoyant shallow jets, Johnston and Volker (1992) included some results on non-buoyant shallow jets close to the nozzle $x/d < 12$. They found that the potential core length is shorter than that of free jets. They also found linear growth rates of 0.107 for both the vertical and horizontal directions, which are higher than the free circular jets. Other researchers have examined shallow jets for the limiting cases of wall jets and surface jets in shallow water.

Ead and Rajaratnam (2002) performed experiments on plane wall jets entering shallow water. In this case the offset ratio is zero and the shear layer grows, eventually reaching the surface, creating a recirculation zone above the nozzle. The length of this recirculation zone was found to be dependant on the submergence ratio and Froude number similar to the surface regime described by Johnston (1985). Two stages were identified for the wall jet. The growth rate was found to be linear in both stages; however, the growth rate was higher in the second stage. The growth rate in the first stage was 0.076 and was higher than a deeply submerged wall jet. The maximum velocity decay rate was higher than that of a plane wall jet in deep water. The decay rate of maximum velocity was also higher in the second stage (Ead and Rajaratnam, 2002).

The limiting case of a plane surface jet in shallow water was examined by Swean and Ramberg (1989). In this case the submergence ratio is large because the jet nozzle is located at the surface. They developed a method to determine if the jet was being affected by the bed. They assumed that in a finite depth some

momentum must be lost to the induced outer flow and therefore at some point this momentum loss must become unacceptable and deviations in the velocity scale would show a breakdown of the jet. If the acceptable momentum loss, ΔJ, was limited to 10% then a usable experiment length L_e or length in which the jet could be considered as a free surface jet could be determined from the following relationship

$$\left(0.05\frac{L_e}{b_o}\right)^{\frac{1}{2}} = \frac{1+\sqrt{\Delta J\left(\frac{2H}{b_o}\right)}}{1+\Delta J} \tag{5.1}$$

Many researchers have also examined jets affected by only one boundary, such as wall jets and near bed jets. In a wall jet, the fluid enters the ambient adjacent to the floor and creates a boundary layer region below the plane of maximum velocity. Above this plane, a shear layer, or free mixing region is created entraining fluid into the jet (Law and Herlina, 2002). The maximum velocity u_m may no longer occur along the nozzle centerline but at some distance z_m from the nozzle centerline. Circular wall jets are three dimensional but still exhibit self-similar properties (Rajaratnam and Pani, 1974).

For circular wall jets and circular near bed jets, the growth rate parallel to the bed has been found to be about 5 times greater than the growth rate perpendicular to the bed. The growth rate of a circular wall jet in the perpendicular direction has been found to be about 0.042 (Rajaratnam and Pani, 1974; Law and Herlina, 2002). Experiments by Padmanabham and Gowda (1991) using smooth polished teak wood as a bed also found this value to be

between 0.04 and 0.049 for different heights of the jet off the bed. The growth rate of circular wall jets parallel to the bed has been found to be 0.2 (Rajaratnam and Pani, 1974), in good agreement with the 0.21 value found by Law and Herlina, 2002. Both growth rates remain constant. Tachie and Balachandar (2004) found that while increasing roughness increases the boundary layer thickness, it has little effect on the growth rate of the jet. However, Wu and Rajaratnam (1990) found that while the parallel growth rate is unaffected, the perpendicular growth rate is increased by a factor of $0.02\left(k_s/d\right)$, where k_s is the roughness of the bed. In the experiments of Law and Herlina (2002), a rectangular region normal to the direction of flow was found in the jet where the half velocity width parallel to the bed remained constant for some distance away from the bed. They found that in this region the momentum flux was completely balanced by skin friction. After a downstream distance of $25d$, the velocity profiles parallel to the bed were self-similar and had higher velocities. Therefore, a Lorentzian distribution was fit to the data (Law and Herlina, 2002). Their results also described the centerline velocity decay rate as,

$$\frac{u_m}{u_o} = 9.23\left(\frac{x}{d}\right)^{-n} \tag{5.2}$$

where n is an exponent and the value of 9.23 was found to decrease with an increase in bed roughness (Wu and Rajaratnam, 1990). The n value ranges between 1.0, found by Rajaratnum and Pani (1974), to 1.29 found by Abrahamsson (1997).

Davis and Winarto (1980) studied circular jets near a bed for offset ratios (y_o/d) of 0.5, 1.0, 2.0, and 4.0. They found that the decay of maximum velocity was similar to that of a free jet with an n value of 1.15 which agreed with the results of Padmanabham and Gowda (1991). Results also showed that velocity profiles normal to the bed had higher local velocities near the bed than a free jet in the early stages of the jet and lower velocities further downstream. They attributed the higher velocities to reduction in mixing in the vertical plane and the lower velocities to the thickening of the turbulent boundary layer near the bed. They also found growth rates for velocity profiles parallel and perpendicular to the bed. The growth rates parallel to the bed were 0.32, 0.33, 0.29, 0.23 for offset ratios of 0.5, 1, 2, and 4, respectively, making them 2.7 – 3.9 times larger than the growth rate of a free jet. The growth rates perpendicular to the bed were 0.037, 0.036, 0.039, and 0.046, respectively, making them 5 – 9.2 times smaller than those measured parallel to the bed. This is a clear indication that the mixing becomes greater parallel to the plane as the jet transitions from a circular free jet to a wall jet (Davis and Winarto, 1980).

While wall jets interact with a solid boundary, surface and shallow jets interact with a free surface. This boundary can move and deform with the jet making surface waves and velocities that affect the jet behavior. Experiments performed by Rajaratnam and Humphries (1984) on plane and circular, non-buoyant, surface jets found that the centerline velocity decay for both nozzle geometries was slower than that in a free jet. The plane surface jet results showed the maximum velocity located at the free surface. The plane surface jet maximum

velocity decay was described by Eq. (2.12a) with a value of A_3 equal to 3.1 instead of 3.5 as suggested for a free jet. The growth rate of the plane surface jet was found to be 0.07, about 72% of a free plane jet. This growth rate is similar to that of a deeply submerged plane wall jet. The circular jet measurements showed the location of the maximum velocity to be below the free surface. The growth rate perpendicular to the surface was found to equal 0.09 similar to that of a circular wall jet, while the growth rate parallel to the free surface was 0.044, about half that of a wall jet.

Similar results were found by Anthony and Willimarth (1992) for a round jet beneath a free surface. These researchers used a three component Laser Doppler Velocimeter (LDV) to measure not only mean flow characteristics but also turbulent velocity fluctuations. The centerline of the 0.635 cm nozzle was located at 1.27 cm below the free surface. Similar to Rajaratnam and Humphries (1984), they found that the growth rate parallel to the free surface was much greater than in the perpendicular direction. Also, at an x/d of 32, the turbulence was affected by the free surface, with the maximum velocity shifting toward the free surface. The streamwise and transverse velocity fluctuations increased toward the free surface while the vertical velocity fluctuations were dampened. The authors attributed this to vortex filaments terminating at the free surface. The results also showed that in a shallow layer near the free surface, the jet widened and a shallow surface current formed. This surface current was much wider than the jet below it with much less turbulent mixing. Waves propagating at an angle outward from the jet in the capillary gravity range were also observed and the

authors attributed the fluctuations in turbulence to the orbital velocities in the wave field.

Experiments more specifically focused on the free surface interactions of a submerged circular jet were performed by Madnia and Bernal, (1994). Using a shadowgraph flow visualization technique along with hot film velocity measurements they were able to take free surface curvature measurements for submergence ratios of 1, 1.5, 2.5 and 3.5. In the near field, vortex ring structures were observed, which terminated perpendicular to the surface farther downstream. In this region surface waves formed and propagated away from the jet symmetrically. The propagation angle relative to the downstream flow for a given depth increased as the initial jet velocity was increased. As the submergence of the jet increased, the vortex generated waves moved downstream until their formation was inhibited by the surface current. Velocity measurements taken in the jet found that the maximum velocity decay was slower than in a free jet and that this effect was more pronounced for smaller values of jet submergence. Growth rates parallel and perpendicular to the surface were reported as 0.078. Results also showed that in the farfield, the jet had twice the momentum of the jet initial momentum when the surface was modeled as a symmetry plane. This produces a relationship similar to Eq. (2.12b) and is shown below

$$\frac{u_o d}{u_m H} = \frac{C_1}{\sqrt{2}}\left(\frac{x-\bar{x}}{H}\right) \tag{5.3}$$

where C_1 is the corresponding value of a free jet ($C_1 = 0.115$). It was also suggested that the half-velocity width, b, normalized by H instead of d, be

measured from the free surface as opposed to the jet centerline for the perpendicular growth rate. Analysis of the surface waves showed an increase and subsequent decrease in surface velocity. This inhibits further wave generation and propagation in the downstream field.

While little research exists on the mixing characteristics of shallow near bed jets, they share many common behaviors with both wall and surface jets. In this study, longitudinal velocity profiles normal and parallel to the bed were measured. The growth rates in normal and parallel to the bed were examined and compared to the growth rate of wall jets and surface jets. The vertical profiles normal to the bed were analyzed using Reichardt's hypothesis and power law.

Experimental Setup

The present experiments were conducted in a 12 ft x 12 ft basin with a maximum depth of 4 ft. The water level was controlled by an adjustable standpipe at the far end of the basin. Flow was provided by a constant head tank adjustable in one inch increments. The jet issued into the basin through a ½ inch nozzle located 36 inches above the floor. To simulate different offset ratios, a flat 4 ft wide by 8 ft long horizontal false floor was placed at the desired level below the jet. Velocity data was captured using a pitot tube with 1/8 inch outer diameter, mounted on a 3 axis cart with 1/16 inch precision. The pitot tube was connected to a differential pressure transducer with a maximum head of 3 feet of water. The output was sampled at 25 Hz for 3200 samples using Labview to convert the signal to an average velocity. Calibration was performed daily

through the use of two standpipes with a head difference of 3 ft (maximum range of the transducer). The standpipes were connected to the pressure transducer in such a way as to allow for zero head and 3 ft head difference. The instrument was also checked for zero calibration between each horizontal and vertical profile. A schematic of the experiment is shown in Fig. 5.2.

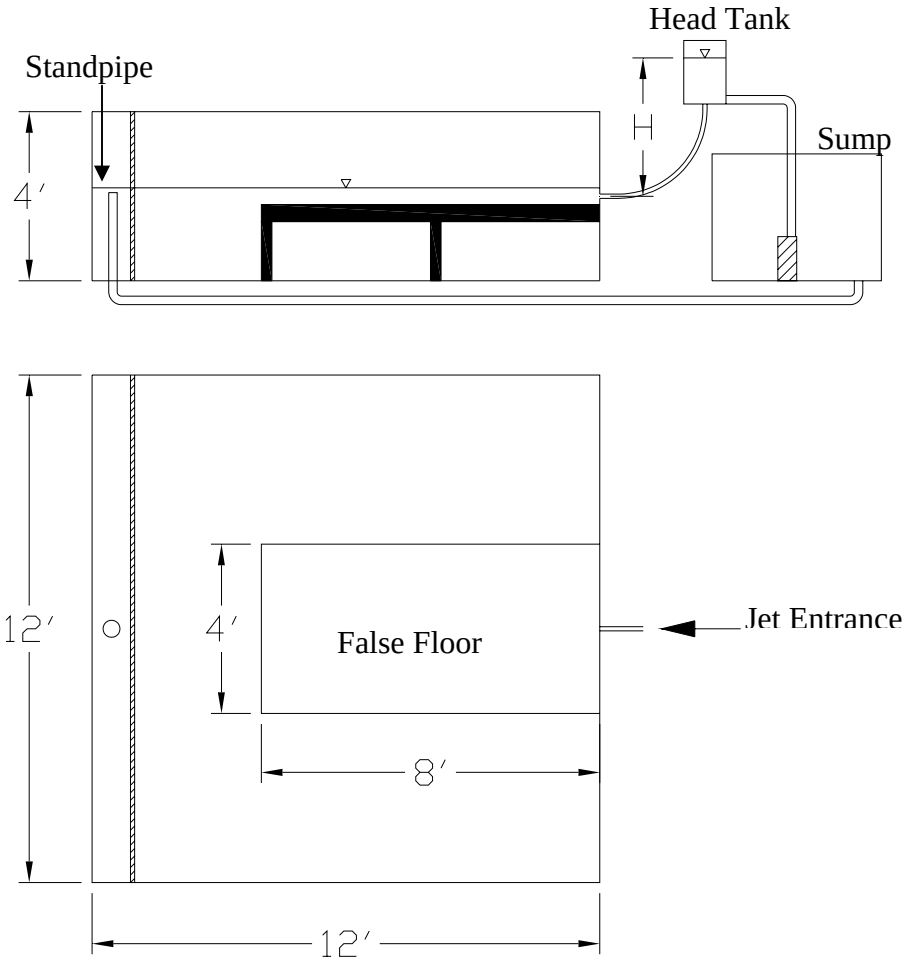

Figure 5.2 Schematic of Model Setup

The offset ratios (y_o/d , Fig 5.1) examined in this experiment were 2, 3, and 4. The submergence ratio (H/d , Fig. 5.1) of the jet was controlled by the standpipe and was equal to the offset ratio for each case. Profiles of Longitudinal velocity in the horizontal (horizontal profiles) and vertical (vertical profiles) planes passing through the point of local maximum velocity were taken at each floor level with three flow rates at x/d locations of 6, 12, 16, 18, 24, 28, 34, 40 and 50. Table 5.1 shows the flow parameters of each experiment.

Table 5.1: Experiment Parameters

Run Number	y_o/d or H/d	R_e	F_r
J1	2	3.9E+04	7.0
J2	2	5.00E+04	8.9
J3	2	5.1E+04	9.2
J4	3	3.8E+04	6.8
J5	3	4.7E+04	8.4
J6	3	5.1E+04	9.1
J7	4	3.8E+04	6.8
J8	4	4.7E+04	8.5
J9	4	5.1E+04	9.1

Results and Discussion

Horizontal and vertical profiles of longitudinal velocity were taken along the planes of local maximum velocity at nine x/d locations from the nozzle. The jet centerline is defined as the location of the maximum velocity and the nozzle centerline extends in a straight line from the center of the nozzle parallel to the bed and perpendicular to the nozzle opening. The velocities were normalized by

the local maximum velocity and the distance from the jet centerline was normalized by the half velocity width for the horizontal profiles as shown in Fig. 5.3. For the vertical profiles the y values were measured from the bed and normalized by the distance from the jet centerline to the bed ($y_o - y_m$) as shown in Fig. 5.4.

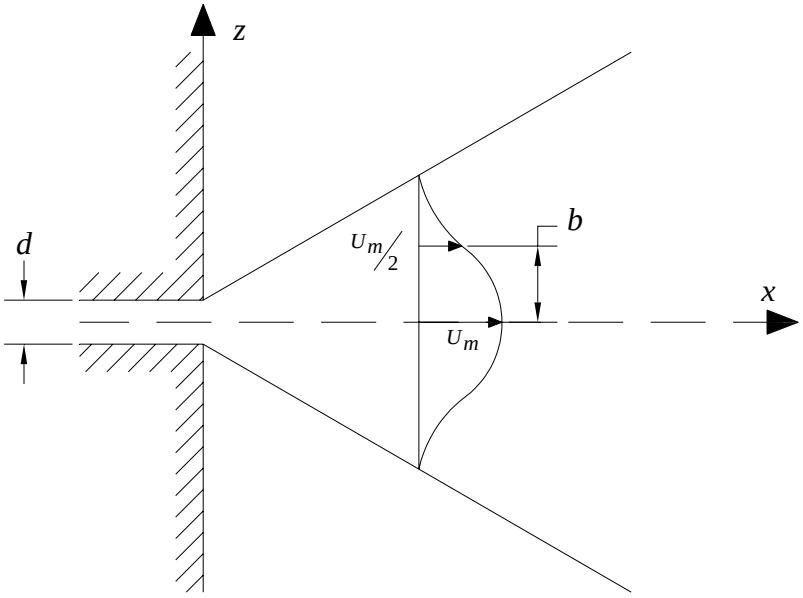

Figure 5.3: Definition Sketch For Horizontal Profiles

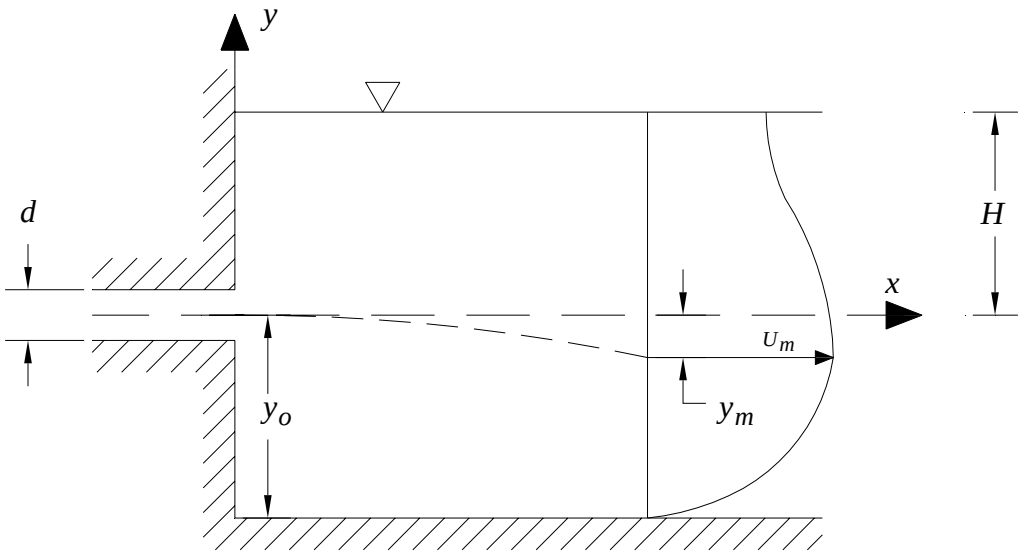

Figure 5.4: Definition Sketch for Vertical Profiles

Horizontal Profiles

The normalized horizontal velocity profiles were self-similar at all locations for all nine combinations of submergence and Reynolds number. The distribution showed good agreement with that of a free jet profile as given by Eq. (2.13). Velocity profiles at x/d = 24 are shown for all 9 cases in Fig. 5.5. The values showed a slight tendency of being smaller in the inner region near the centerline and larger than the free jet away from the center line. Velocity profiles for the other eight x/d locations can be found in Appendix A.

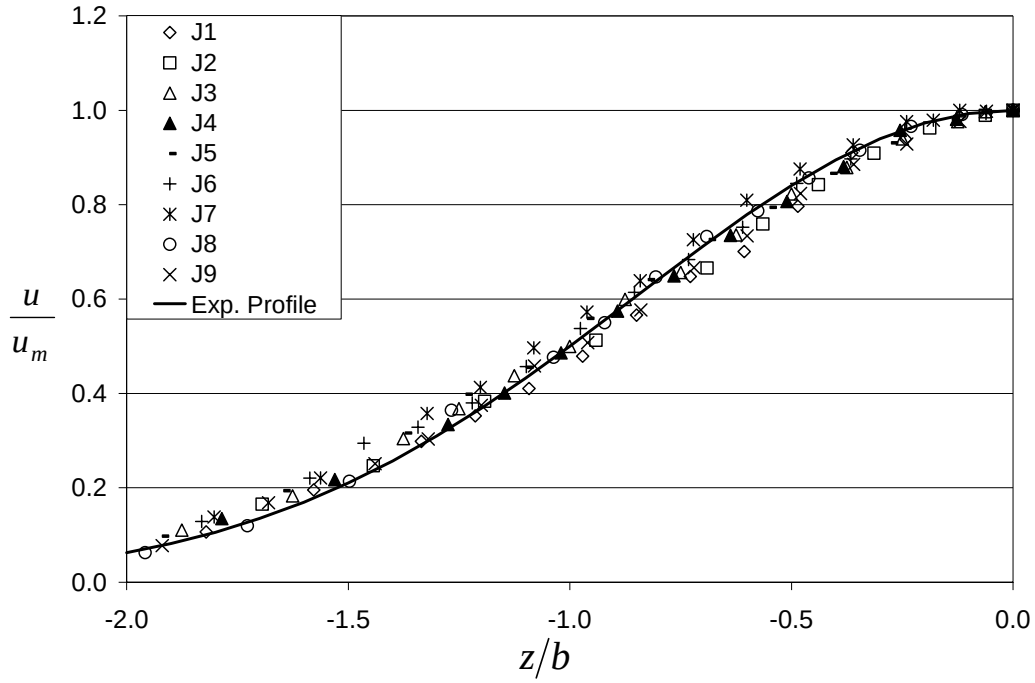

Figure 5.5: Horizontal Profiles at x/d = 24

Jet half width values, normalized by the nozzle diameter, for all nine experimental cases are shown in Fig. 5.6. These half widths were linear with x/d for a submergence ratio of 4 for all nine x/d locations with an average slope of 0.071. For locations near the nozzle, the other two submergence ratio cases also followed this trend. However, for a submergence ratio of 2, the half widths began to deviate at an x/d of 28. The deviation began at x/d of 34 for the submergence ratio of 3. The deviations can be divided into two regions in the case of H/d of 2 and 3. Near the nozzle these regions follow the trend seen by the large submergence cases and change to a linear trend with a larger slope. Plots of these regions are shown in Figs. 5.7, 5.8 and 5.9 for submergence ratios of 2, 3, and 4, respectively. It is possible that the growth rate for submergence

ratio of 4 may begin to deviate from the initial growth rate further downstream. This behavior of higher horizontal growth rate has not been reported for wall and surface jets.

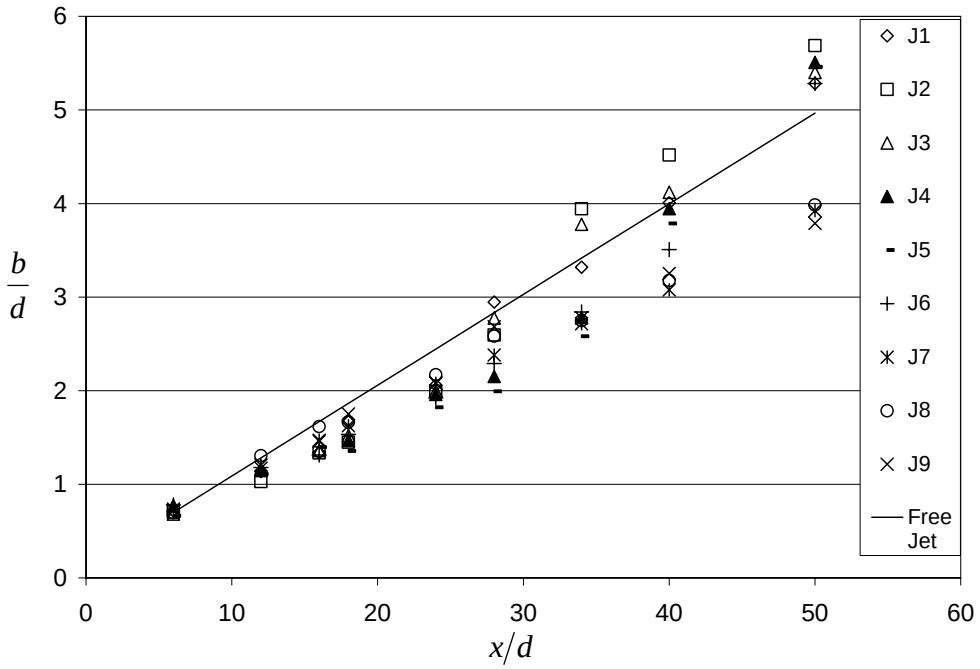

Figure 5.6: Horizontal Half-Widths

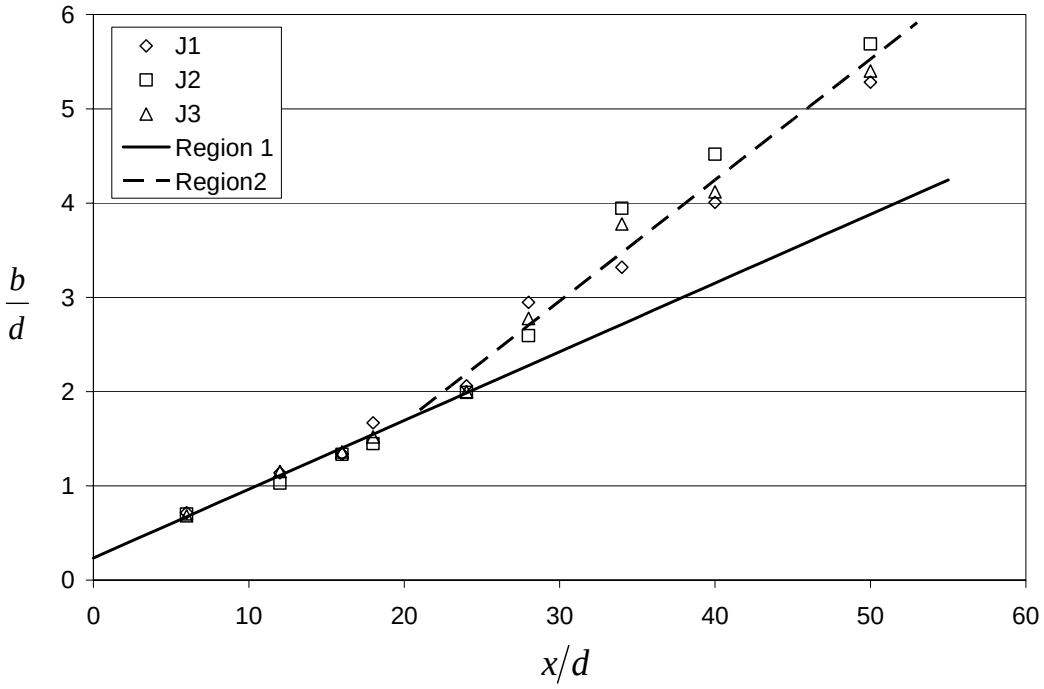

Figure 5.7: Horizontal Half-Widths for $H/d = 2$

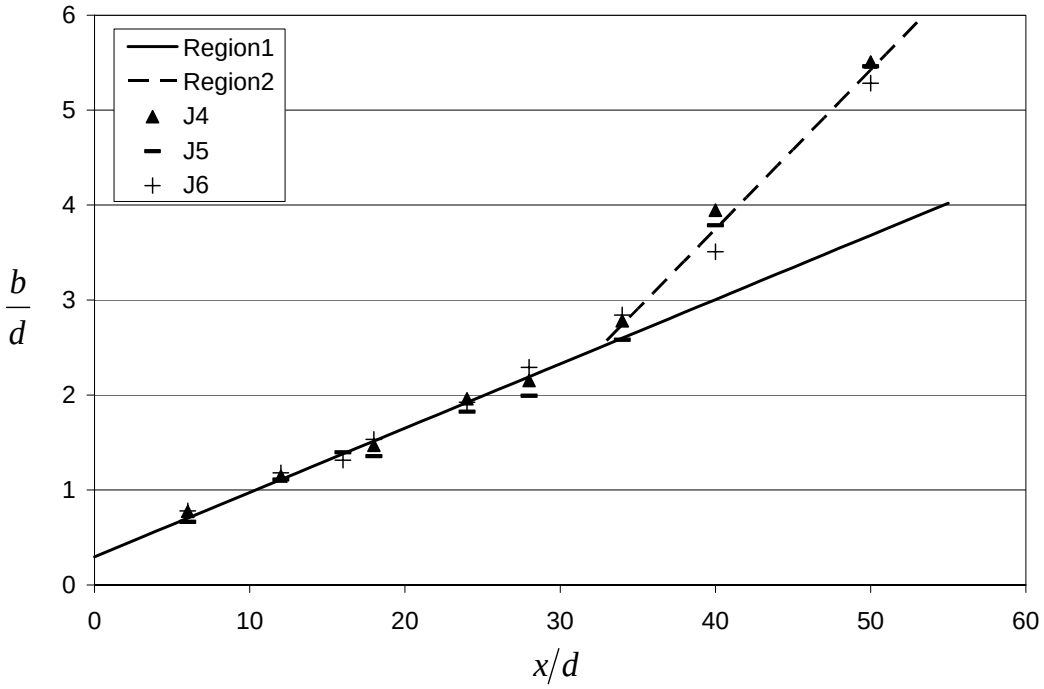

Figure 5.8: Horizontal Half-Widths for $H/d = 3$

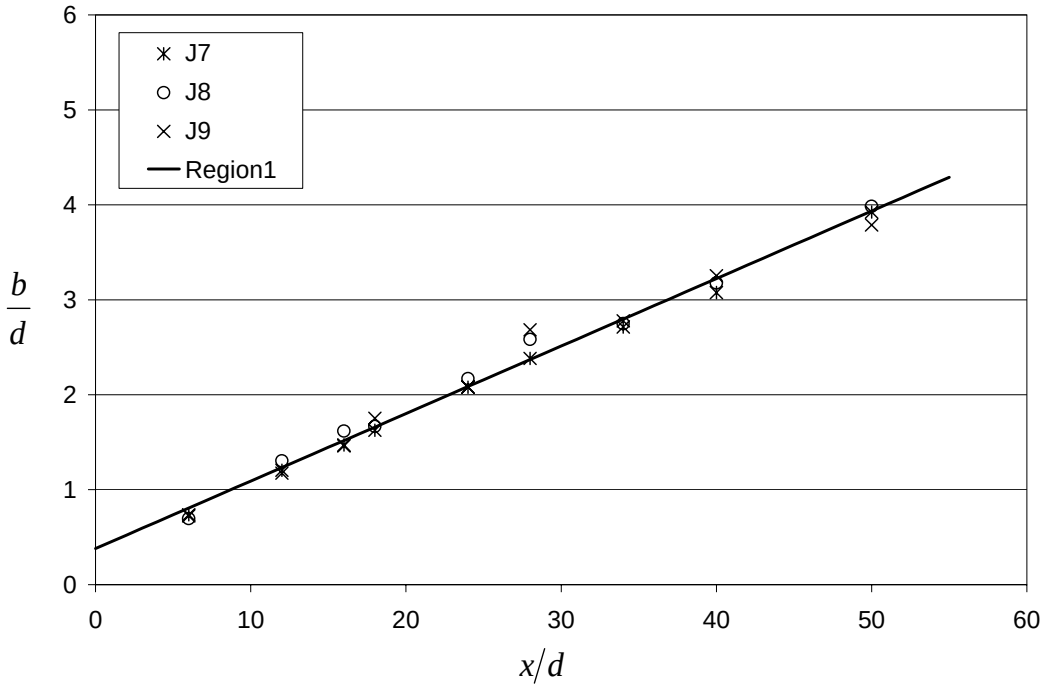

Figure 5.9: Horizontal Half-Widths for $H/d = 4$

Decay of the maximum centerline velocity was also calculated for each case. The results are shown in Fig. 5.10. The results are slightly larger than those from a circular free jet beyond x/d = 24. The results from the submerged jet experiments of Madnia and Bernal (1994) and the wall jet results from Law and Herlina (2002) are included for comparison.

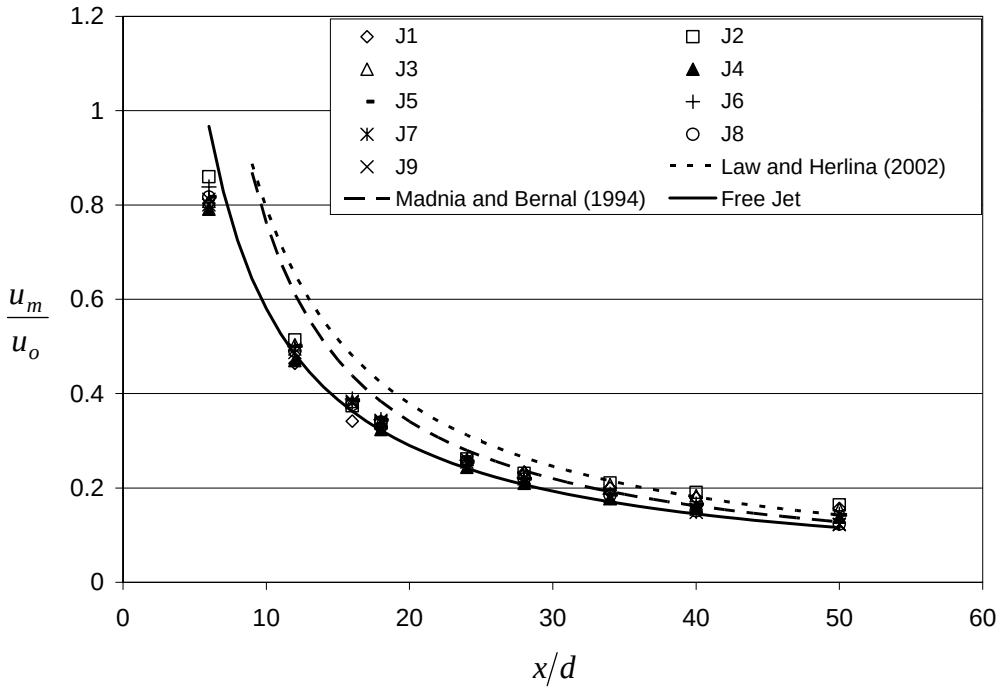

Figure 5.10: Centerline Velocity Decay

Vertical Profiles

The vertical velocity profiles can be divided into two categories, the boundary layer, which occurs below the jet centerline and the mixing region, which occurs above the jet centerline. At locations near the nozzle, the vertical profiles were self similar with an average growth rate of 0.12 and showed good agreement with the horizontal profiles, an example of the vertical profiles can be seen in Figure 5.11 for all 9 experimental cases for x/d = 12. Velocity profiles for the other eight x/d locations can be found in Appendix A. The growth rates for the vertical profiles where the self similarity was observed are shown in Figure 5.12.

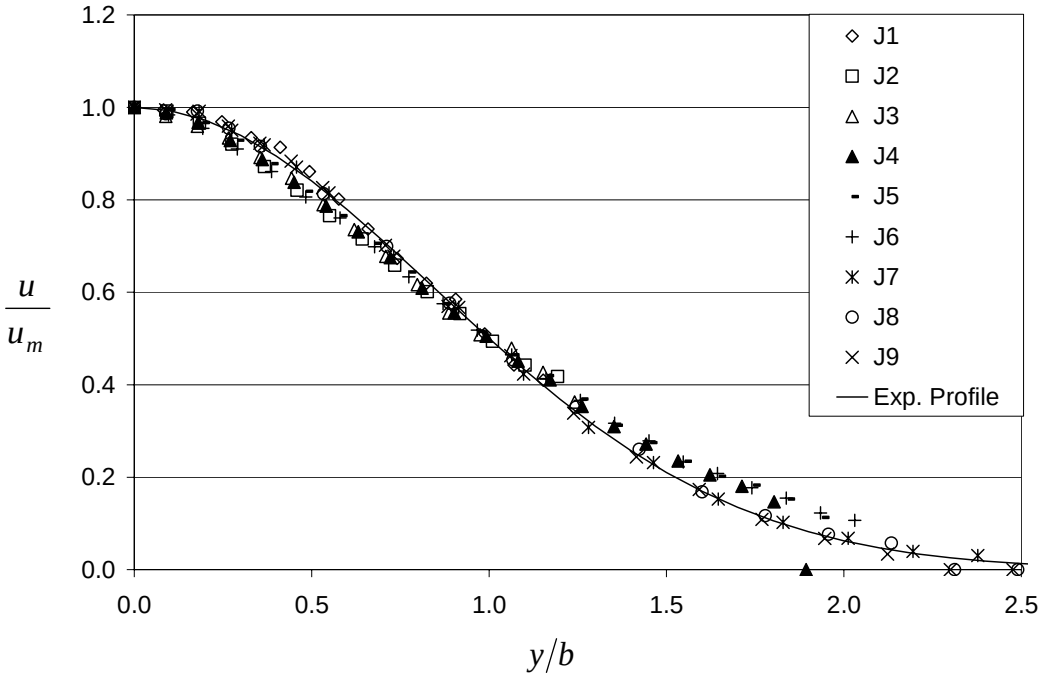

Figure 5.11: Vertical Profiles at x/d = 12

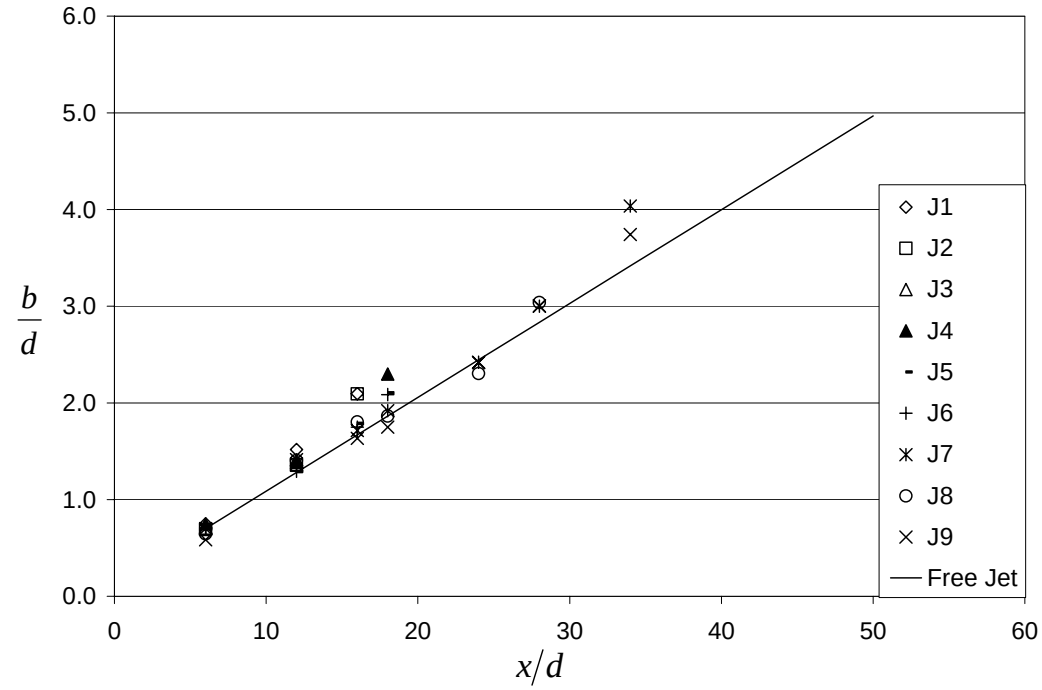

Figure 5.12: Vertical Half-Widths

Past the point where the jet began to interact with the boundaries, the half width for the profile above and below the jet centerline could not determined as a velocity of $u_m/2$ was not measured in the profile. At this point a power law was fit to the boundary layer portion of the vertical profiles in the form of Eq. (5.4).

$$\frac{u}{u_m} = A\left(\overline{Y}\right)^{1/m} \tag{5.4}$$

were $\overline{Y}$ is given by Eq. (5.5).

$$\overline{Y} = \frac{y_o + y}{y_o - y_m} \tag{5.5}$$

where y, y_o and y_m are defined in Figure 5.4. The values of A, m and the regression coefficient (R^2) are shown below in Table 5.2.

The majority of the curve fits represent the data adequately; however, the values of A are not unity therefore when the jet centerline is reached, the curves will not predict a u/u_m value of unity, with the largest coefficient predicting a value of 1.053. No relationship was found between m and x/d. An example of the curve fit for the case of J8 is shown in Fig. 5.13. Curve fits for the remaining cases can be found in Appendix B.

Table 5.2: Power Law Curve Fit Parameters

x/d	Test	J1	J2	J3	J4	J5	J6	J7	J8	J9
6	A									
	m									
	R^2									
12	A									
	m									
	R^2									
16	A	1.03	1.01	1.03						
	m	5.28	2.95	3.14						
	R^2	0.951	0.993	0.988						
18	A	0.99	1.00	1.02						
	m	5.83	4.54	4.39						
	R^2	0.987	0.996	0.993						
24	A	1.02	1.03	1.05				1.02	1.03	1.03
	m	9.61	8.73	5.80				3.55	3.62	3.94
	R^2	0.929	0.917	0.873				0.995	0.992	0.990
28	A	1.02	1.03	1.03	0.86		0.90	1.03	1.04	1.04
	m	6.70	7.27	7.64	2.19		2.46	4.65	4.90	5.32
	R^2	0.891	0.827	0.953	0.963		0.967	0.968	0.955	0.924
34	A	1.02	1.03	1.03	0.98	0.98	1.02	1.05	1.04	1.08
	m	5.61	5.66	5.83	3.22	3.69	3.63	4.89	6.44	5.10
	R^2	0.965	0.874	0.961	0.986	0.973	0.994	0.863	0.893	0.743
40	A	1.03	1.04	1.05	1.01	1.01	1.01	1.04	1.04	1.07
	m	7.21	5.65	6.11	5.31	5.31	5.41	4.36	5.20	5.65
	R^2	0.918	0.835	0.908	0.992	0.993	0.969	0.872	0.943	0.866
50	A	1.03	1.03	1.03	1.02	1.03	1.03	1.05	1.05	1.04
	m	5.76	7.47	6.41	7.62	7.92	9.17	4.73	4.33	4.90
	R^2	0.947	0.778	0.947	0.909	0.928	0.861	0.941	0.951	0.958

*The blank shaded cell represent self-similar behavior

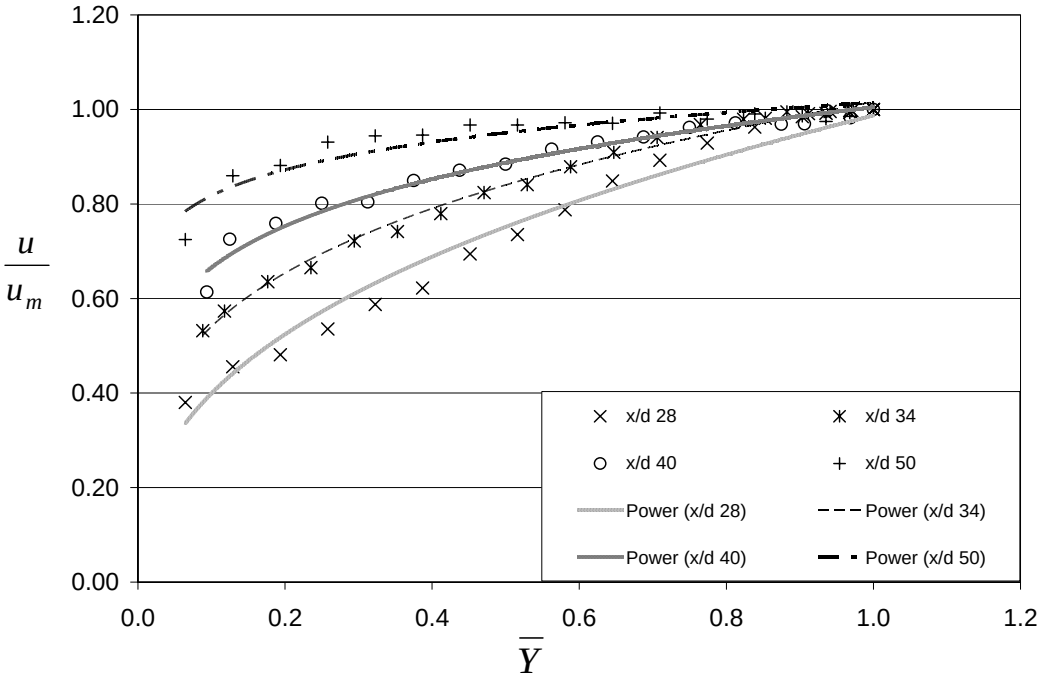

Figure 5.13: Power Law Fit for Vertical Boundary Layer Profile of J8

The locations of the local maximum velocities are shown in Fig. 5.14. The jet centerline deviated from the nozzle centerline for low submergence ratios. The large submergence ratio cases remained close to the nozzle centerline. These are the same cases for which the growth rate remained linear for all x/d locations. The $y_o/d = 2$ cases dip toward the bed and begin to return to the nozzle centerline at about $x/d = 34$, suggesting that the jet is attaching itself to the bed. Test parameters and the centerline shape for this test falls within the reattached bed jets regime outlined by Johnston (1985). For ratios of $y_o/d = 3$ the jet centerlines deviate from the nozzle center line further downstream. This is expected as the bed/surface interaction occurs further downstream for the deeper cases. For experiments with $y_o/d = 4$ the jet centerline stays relatively close to

the nozzle centerline. These cases fall into the zone of both surface and bed jets based on their submergence and inlet Froude number, according to Johnston (1985). However, the centerline meander does not seem to support one boundary attachment over the other for this offset ratio.

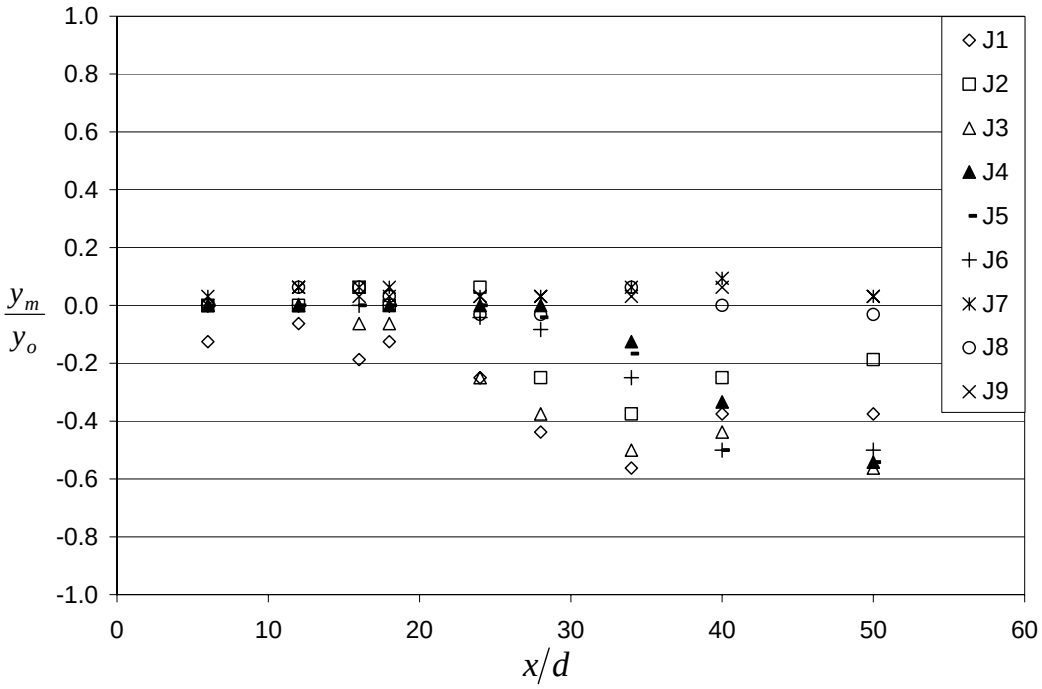

Figure 5.14: Deviation of Maximum Velocity from the Nozzle Centerline

For velocity profiles above the bed in the mixing region, the free surface was modeled as a plane of symmetry. Reichardt's hypothesis for a circular jet (Miller and Comings, 1957) was used and the equation is given by

$$\frac{u}{u_m} = \frac{1}{A_4}\sqrt{\frac{1}{8A_2^2F_2}\sum_{n=-\infty}^{\infty}\exp\left(-2\ln(2)\left(\frac{y-n\lambda}{b}\right)^2\right)} \qquad (5.6)$$

where n is an integer representing the number of image jets, one in this case, $\lambda = 2(H + y_m)$, A_2 is the growth rate of a circular free jet, F_2 is equal to 0.36 for circular free jets, and A_4 is the decay rate of the local maximum velocity.

An example of the symmetry solution above the jet centerline is shown in Fig. 5.15 using J8. The remaining cases can be found in Appendix C.

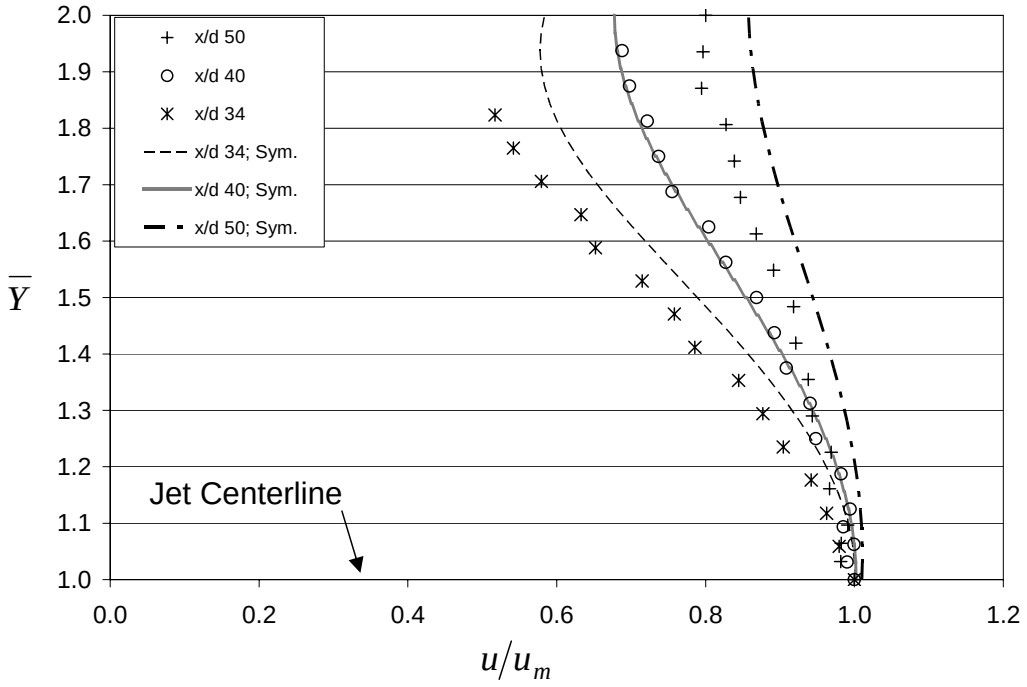

Figure 5.15: Plane of Symmetry and Power Law fit for J8

Reichardt's hypothesis has been modified in this study to report velocities normalized by the local maximum velocity as well as accounting for the meander in the jet centerline. These modifications give better results than assuming constant jet spacing. However, while the plane of symmetry solution shows good agreement for a few cases, it does not systematically describe the behavior above

the jet centerline. The accuracy of the solution seemed to improve with submergence.

The effects of the jet on the surface were also examined qualitatively and are shown in Figs. 5.16, 5.17, and 5.18 for increasing submergence values. The effects of increased submergence moved the beginning of the disturbance downstream of the nozzle. Increased submergence also showed an increase in wave length of the surface waves as well a decrease in amplitude. Wave heights were higher for lower values of y_o/d with a maximum recorded wave height for J3 of approximately 0.03 inches. The effects of Reynolds number on the wave field could not be distinguished due to the small range of values used in the experiment.

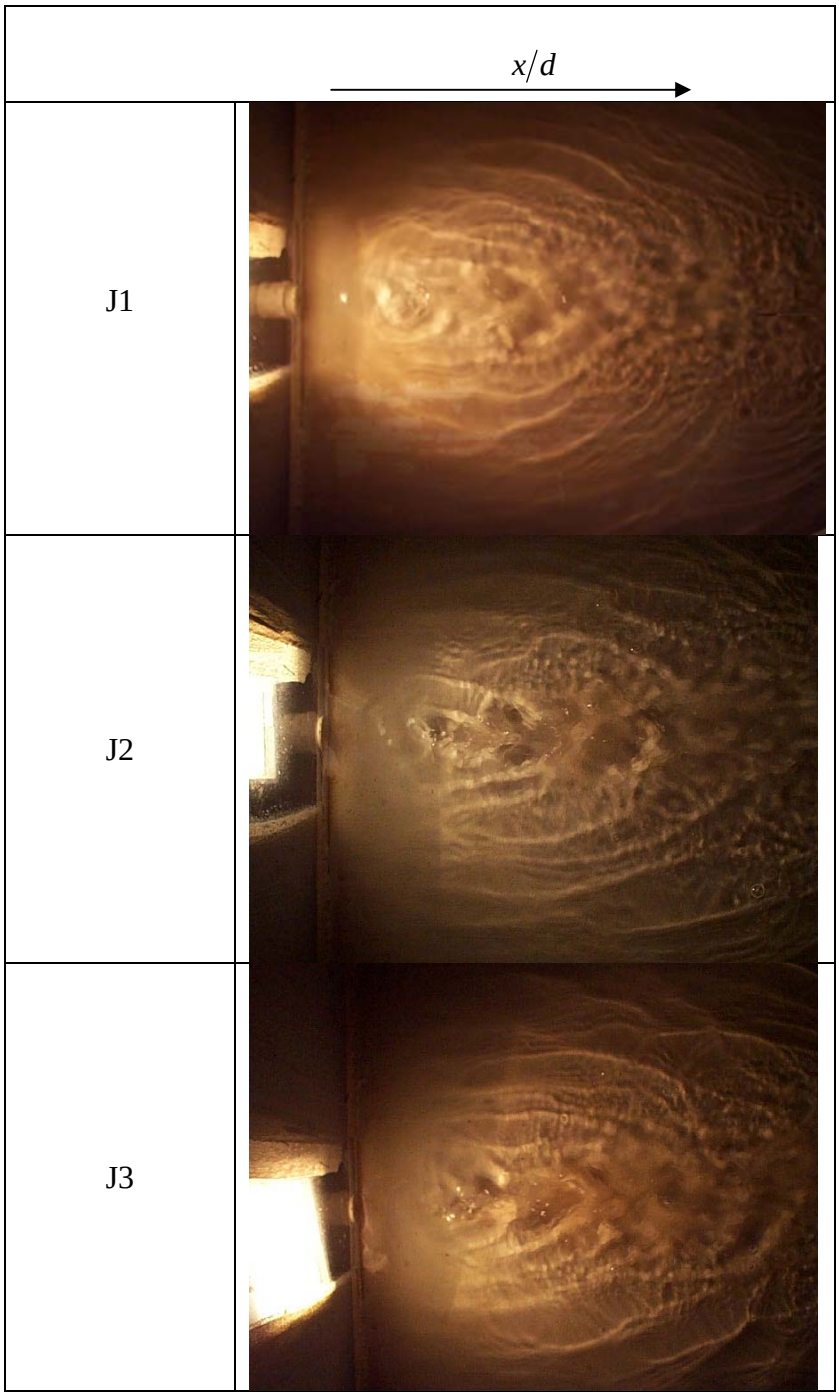

Figure 5.16: Photographs of Surface Disturbance for y_o/d = 2

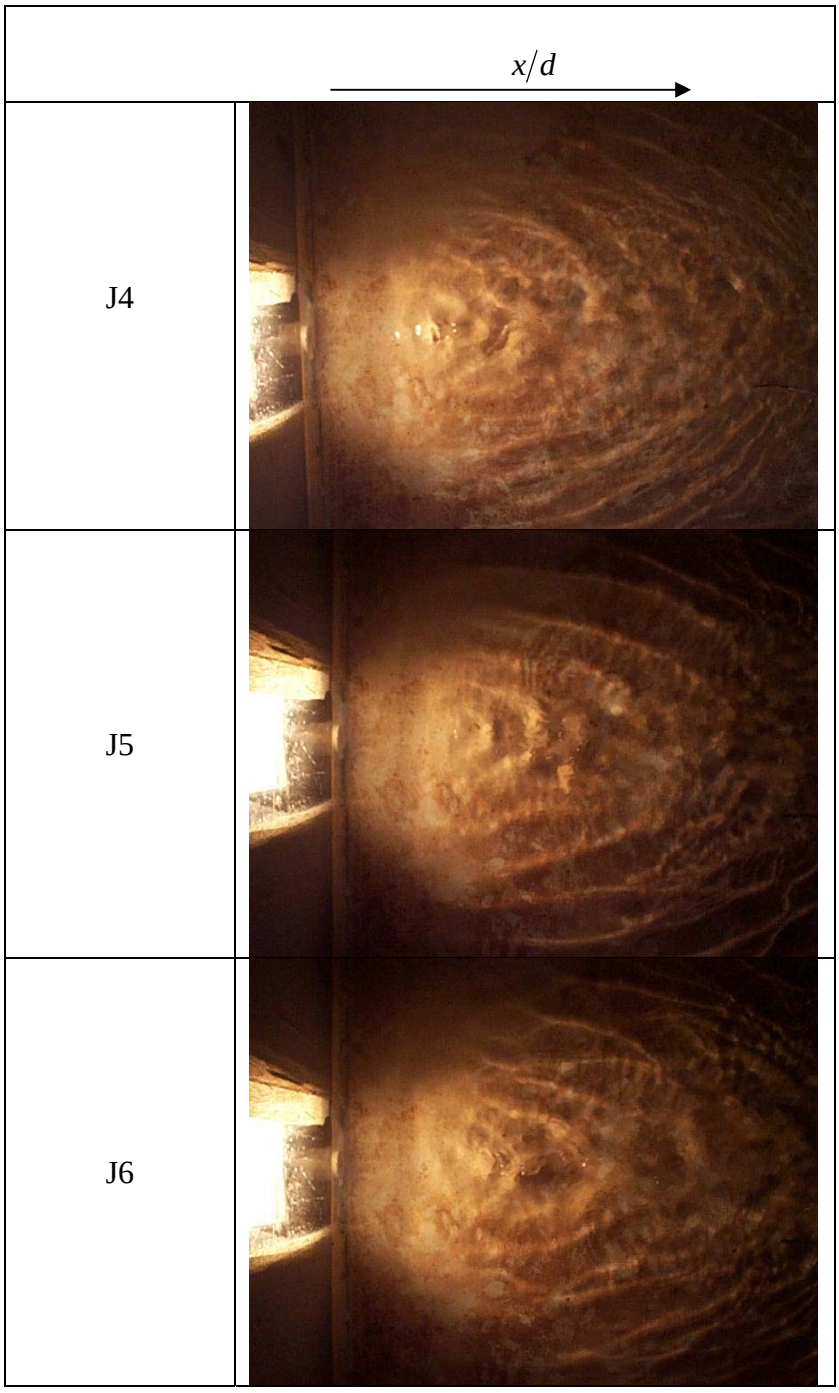

Figure 5.17: Photographs of Surface Disturbance for y_o/d = 3

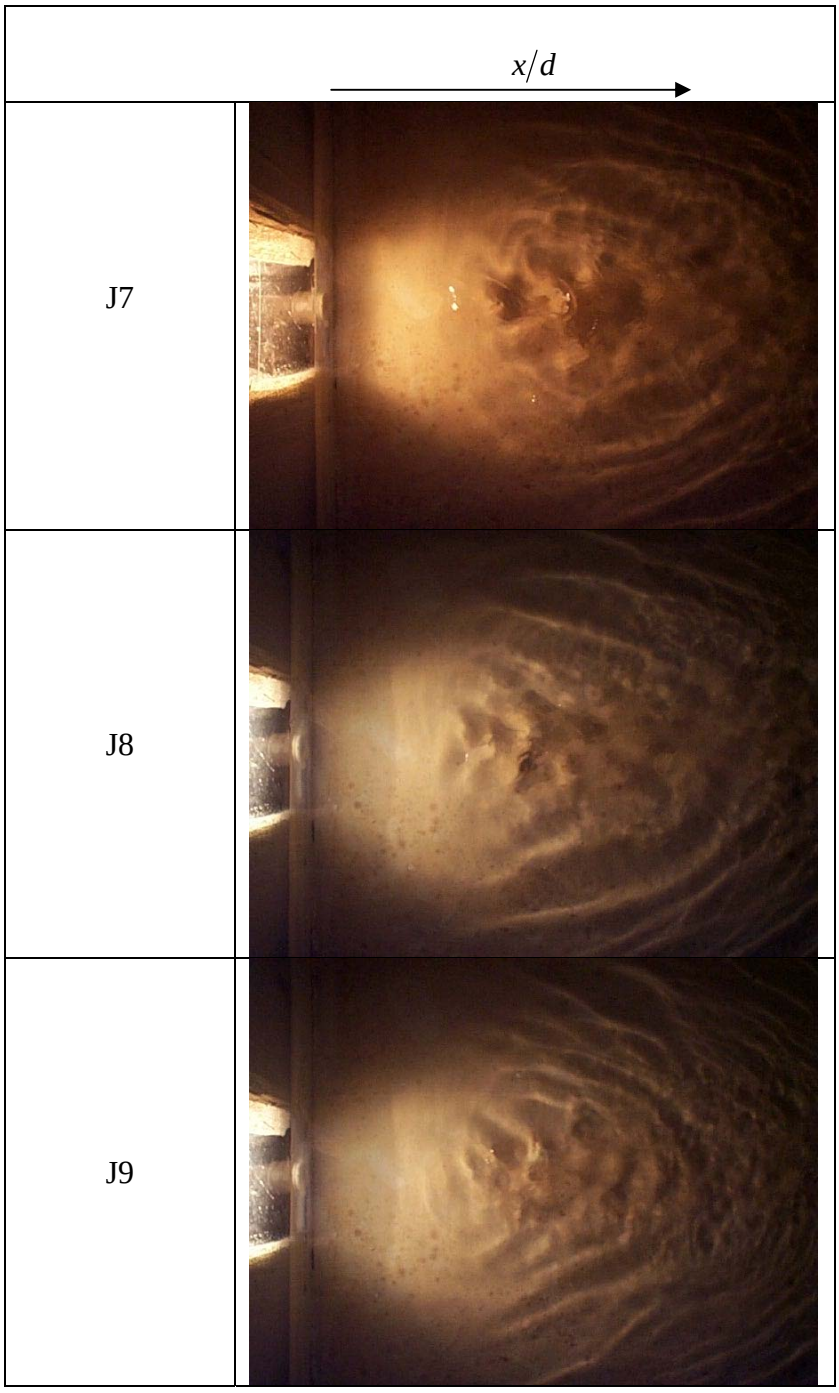

Figure 5.18: Photographs of Surface Disturbance for y_o/d = 4

Conclusions

The horizontal velocity profiles in the jet are self-similar and show good agreement with a free jet profile. The growth rate in the horizontal direction was found to be 0.071 in the near field and matches closely with that found by Madnia and Bernal (1994). The growth rates diverge from this value as the jets interact with the boundaries for the lower two submergence ratios. The centerline decay shows good agreement with a free jet near the nozzle but the decay rate is slower in the far field. This slower decay rate is indicative of a reduction in mixing.

The velocity profiles, in the vertical plane, near the nozzle were self similar and showed good agreement with the horizontal profiles, however their growth rates were larger (0.12) than the horizontal growth rates. In the case of wall or surface jets, this growth rate was usually found to be larger in the near field than the horizontal growth rate (Davis and Winarto, 1980). The velocity profiles below the jet, away from the nozzle, were not self-similar when normalized by $y_o - y_m$. However, a power law was found to fit the profiles in the boundary layer region of the jet. The coefficients of the power law were not one and so these fits over or under predict u/u_m at the jet centerline. Also no relationship between the exponent and the distance from the nozzle could be determined.

The deviation of the jet centerlines from the nozzle centerline in the y direction were examined. The jet centerlines meander around the nozzle centerline for the case of $y_o/d = 4$. The other two cases move toward the bed and

then begin to come back up toward the nozzle centerline seeming to fall into the reattached bed jet regime described by Johnston (1985).

Velocity profiles in the vertical direction for locations in the mixing region, away from the nozzle of the jet, were modeled by taking the surface as a plane of symmetry. The model was slightly modified in this study to account for the jet center line meander by adjusting the jet spacing parameter λ. The solution failed to systematically describe the jet behavior especially at low submergence ratios. A qualitative examination of surface waves showed that the wavelength increased and amplitude decreased as H/d increased.

CHAPTER 6
CONCLUSIONS AND RECOMENDATIONS

Shear flows occur in many industrial and environmental applications. It is very important to understand their behavior and mixing characteristics when designing outfalls into the environment. A better understanding of the behavior of the computational models used when simulating these widely occurring flows will lead to more accurate predictions of flow behavior in the design stage avoiding situations like that at the J. H. Overton Dam.

The $k-\varepsilon$ and RNG turbulence schemes are widely used to predict the behavior of shear flows. When modeling free circular and plane turbulent jets, comparisons of the schemes' behavior, to well documented empirical and analytical solutions, were made. A summary table of the behavior of each scheme is shown in Tables 6.1 and 6.2 for plane and circular jets, respectively.

Table 6.1: Evaluation of Scheme Performance for Plane Turbulent Jet

Jet Behavior	$k-\varepsilon$	RNG	Comment
Growth Rate	G	Ok	RNG predicted higher values than the $k-\varepsilon$ and those reported in the literature
Centerline Velocity Decay	G	Ok	$k-\varepsilon$ error magnitude under 0.03 for whole rage with RNG up to 0.05
Longitudinal Velocity Profiles	G	Ok	RNG had high error (-0.5) near the nozzle
Vertical Velocity Profiles	Ok	Ok	RNG had high error near the nozzle but was lower than the $k-\varepsilon$ for $x/2b_o = 50$
Turbulent Kinetic Energy	No	No	Both Over Predicted with the RNG error 50% or greater than the $k-\varepsilon$

*G = Good performance, Ok = Satisfactory performance, and No = Poor performance

Table 6.2: Evaluation of Scheme Performance for Circular Turbulent Jet

Jet Behavior	$k-\varepsilon$	RNG	Comment
Growth Rate	G	Ok	RNG predicted higher values than the $k-\varepsilon$ and those reported in the literature
Centerline Velocity Decay	G	No	RNG underestimated values with an error as much as 0.3 while the $k-\varepsilon$ stayed below 0.07
Longitudinal Velocity Profiles	G	G	
Radial Velocity Profiles	Ok	Ok	
Turbulent Kinetic Energy	No	No	RNG showed better performance in the inner region of the jet

An evaluation of the $k-\varepsilon$ and RNG turbulence schemes are also performed for the case of a submerged hydraulic jump. Comparisons to experimental data were used to evaluate the performance of both schemes. A summary table of the behavior of the schemes is shown below in Table 6.3.

Table 6.3: Evaluation of Scheme Performance for Submerged Hydraulic Jump

Jump Behavior	$k-\varepsilon$	RNG	Comment
Water Surface Profile	No	No	Overpredicted by both
Maximum Velocity	No	G	$k-\varepsilon$ over predicted in all three cases
Longitudinal Velocity Profiles	Ok	G	RNG better performance near the bed
Vertical Velocity Profiles	No	No	
Reverse flow Region, (velocity magnitude and location)	No	No	Both the magnitude and location were over predicted by both schemes
Reverse Flow Region, (longitudinal extent)	G	G	
Turbulent Kinetic Energy Profiles	No	No	Both models overestimated the location and magnitude of the maximum value

As seen from the above tables both models consistently over predict turbulent kinetic energy. The different behaviors of the two models when modeling the turbulent jets and submerged jump can be seen in the longitudinal velocity profiles. The difference can be attributed to the presence of the bed in the in the submerged hydraulic jump creating higher turbulent shear than seen in the free jets. The better performance of the RNG model in the high shear region near the bed is expected as this model was designed for high shear flows.

However, when modeling lower shear flows the $k-\varepsilon$ model seems to give more accurate predictions.

In the case of shear flows in natural channels, the complicated geometry makes the use of three dimensional computational models impractical. In many cases a depth-averaged model may be used. These depth-averaged models use turbulent closure schemes just like their three dimensional counter parts. In this work a two dimensional depth-averaged model is used to compare three depth-averaged turbulent closure schemes to experimental and field measurements downstream of a lock and dam. The schemes are the Parabolic eddy viscosity, modified mixing length and depth-averaged $k-\varepsilon$ schemes. The main flow parameters used for evaluation are the size and strength of the recirculating eddies as well as cross channel velocity profiles. The results show that the mixing length and $k-\varepsilon$ schemes perform well in predicting the velocity profiles as well as accurately predicting, the size, shape, and location of eddies found in the physical model study. However, the eddy viscosity profiles across the channel in the recirculation zone, computed using mixing length scheme, differ from that predicted using the $k-\varepsilon$ scheme. The results from the two tests conducted in this study show that the modified mixing length turbulent closure scheme, though simple, can be used to predict flow features in the channel downstream of a lock and dam. However, the results are specific to this study and the applicability of the mixing length model must be verified against the $k-\varepsilon$ scheme for other applications.

While the behavior of turbulence models is important for accurate prediction of flow behavior, the behavior of the flow itself must be understood for a computational model to be developed requiring experimental measurements to elucidate general and specific flow behaviors. The final portion of this research is an experimental study of circular shallow near bed jets. This shear flow shares many commonalities to shallow jets and near bed jets. The shallow near bed jets were evaluated at three different submergence levels which were equal to the height of the jet off the floor in each case. Each submergence level was evaluated at three flow rates. Profiles of longitudinal velocity were taken in the vertical and horizontal planes of the local maximum velocity. The results showed that the horizontal profiles were self similar with a growth rate similar to that of a submerged jet. The growth rate was linear for the large submergence case. However at the lower submergences, growth rates began to increase as the vertical expansion of the jet was affected by the boundaries and the mixing rate increased in the horizontal plane. The path of the jet centerline showed that the jets attached themselves to the bed in agreement with previous research by Johnston (1985).

Evaluation of the velocity profiles in the vertical directions showed that the jet transitions from a free jet to resemble a wall or surface jet. It was found that the profiles in the vertical direction below the jet centerline could be modeled by a power law curve. The power law fits adequately described the profile shape and magnitude however the condition of unity for the normalized velocity at the

jet centerline is not met. Also no relationship was found between the fitting coefficients and the jets parameters.

Above the jet the profiles were modeled by taking the surface as a plane of symmetry, using a modified Reichardt's hypothesis. The symmetry solution failed to systematically predict the behavior of the vertical profile above the jet centerline. A qualitative examination of the surface wave field showed that as the submergence was increased, the wavelengths increased and the wave amplitudes decreased.

The author would like to recommend future studies to further verify the modifications made to the mixing length model in this research. Furthermore, future research in the field of shallow near bed jets should include asymmetric submergence and offset ratios and a larger range of Reynolds numbers. Including the effects of bed roughness on the jet is also recommended. Finally the author would like to recommend the simulation of shallow near bed jets, using the turbulence schemes evaluated in this study.

APPENDICES

Appendix A

Horizontal and Vertical Profiles

Below are the longitudinal velocity profiles in the horizontal and vertical planes of local maximum velocity for all x/d locations not shown in the text.

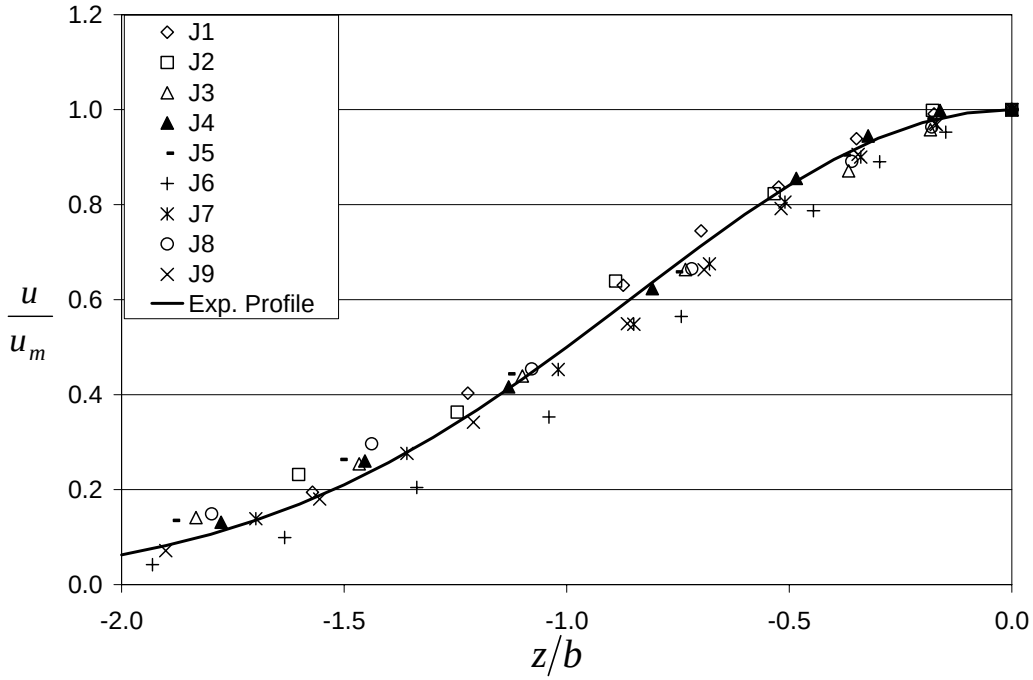

Horizontal Profile for x/d = 6

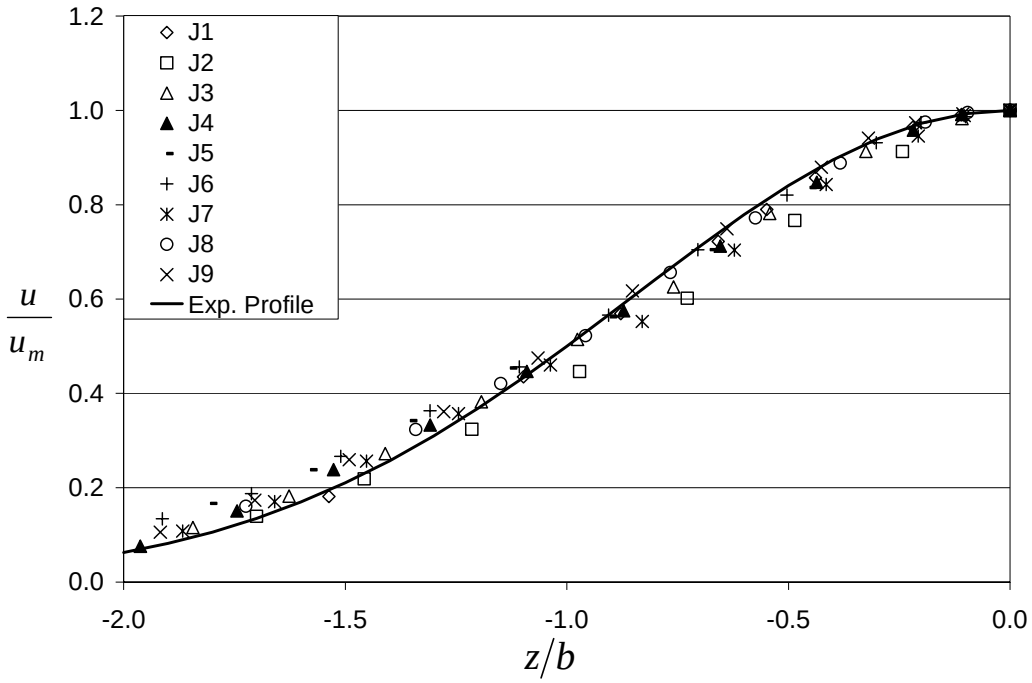

Horizontal Profile for x/d = 12

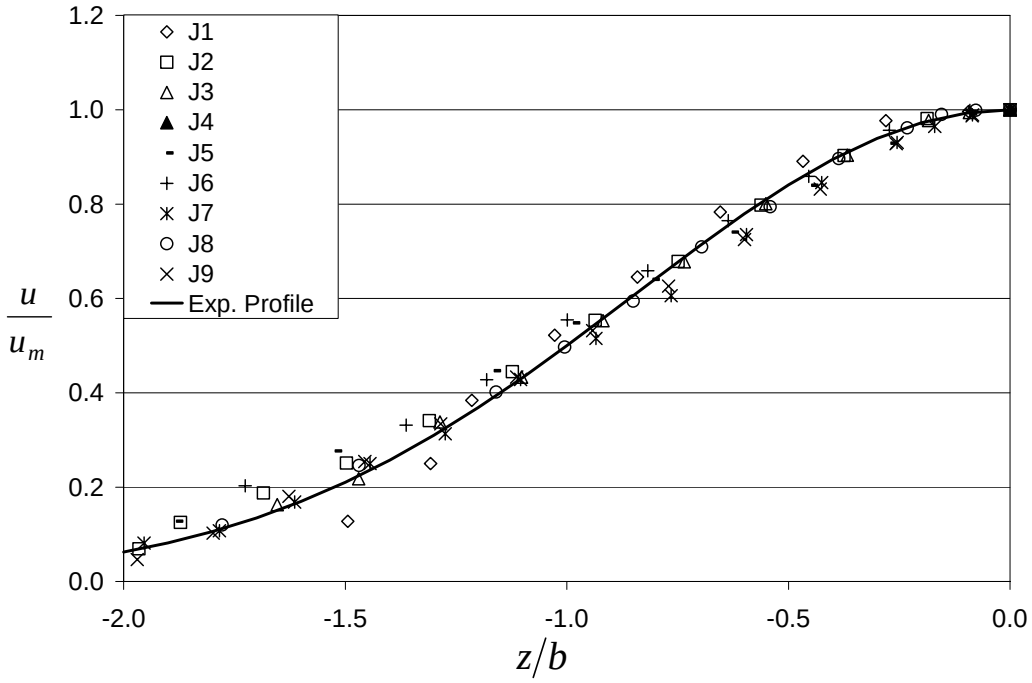

Horizontal Profile for x/d =16

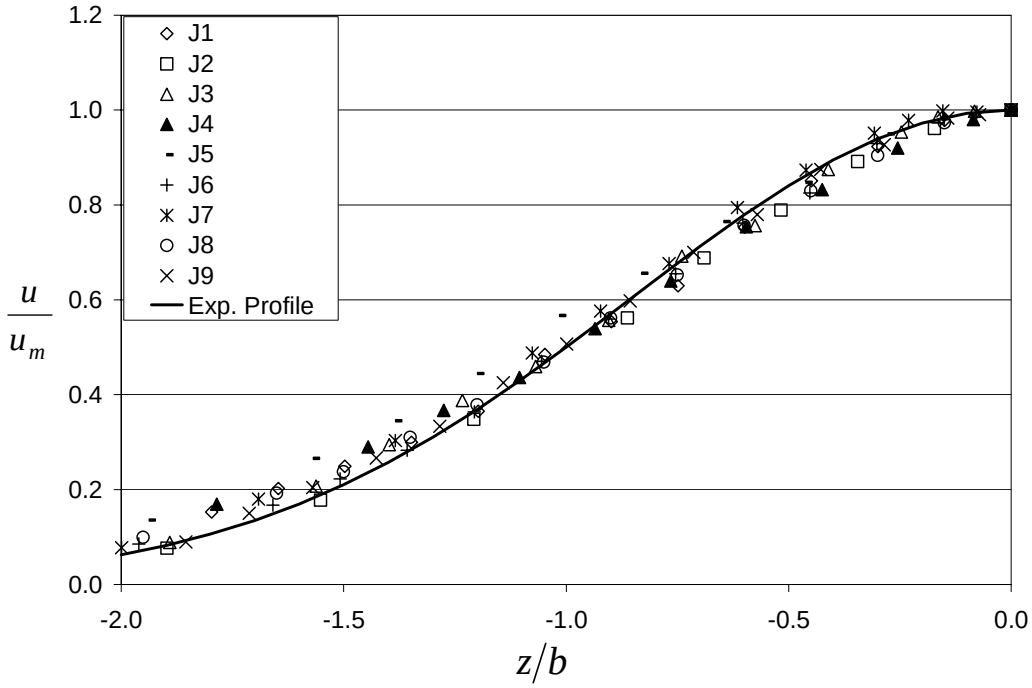

Horizontal Profile for x/d =18

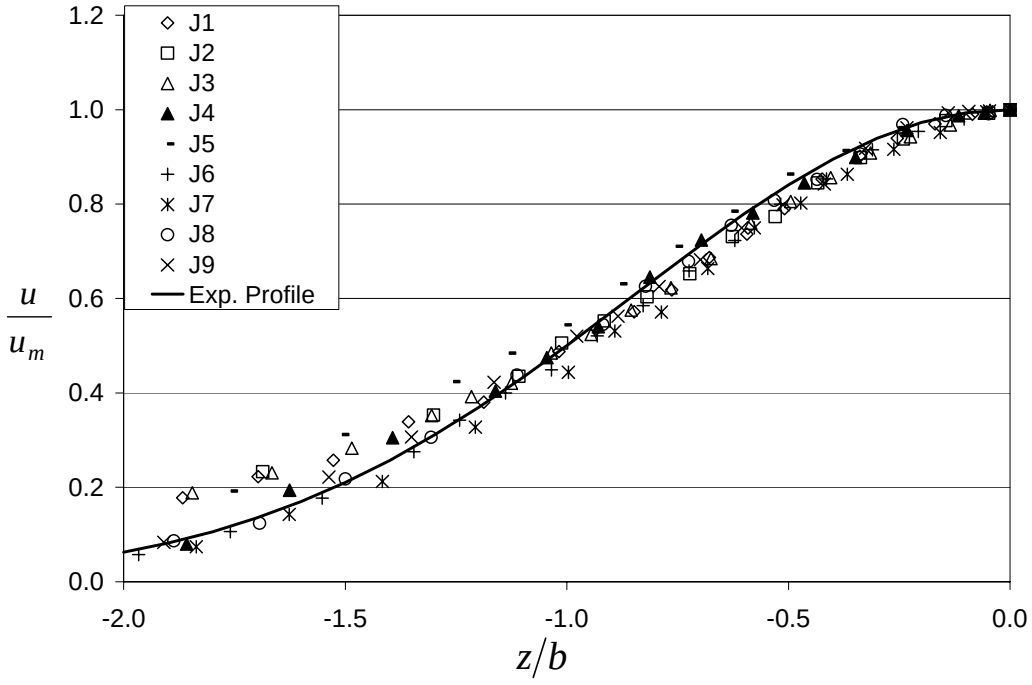

Horizontal Profile for x/d =28

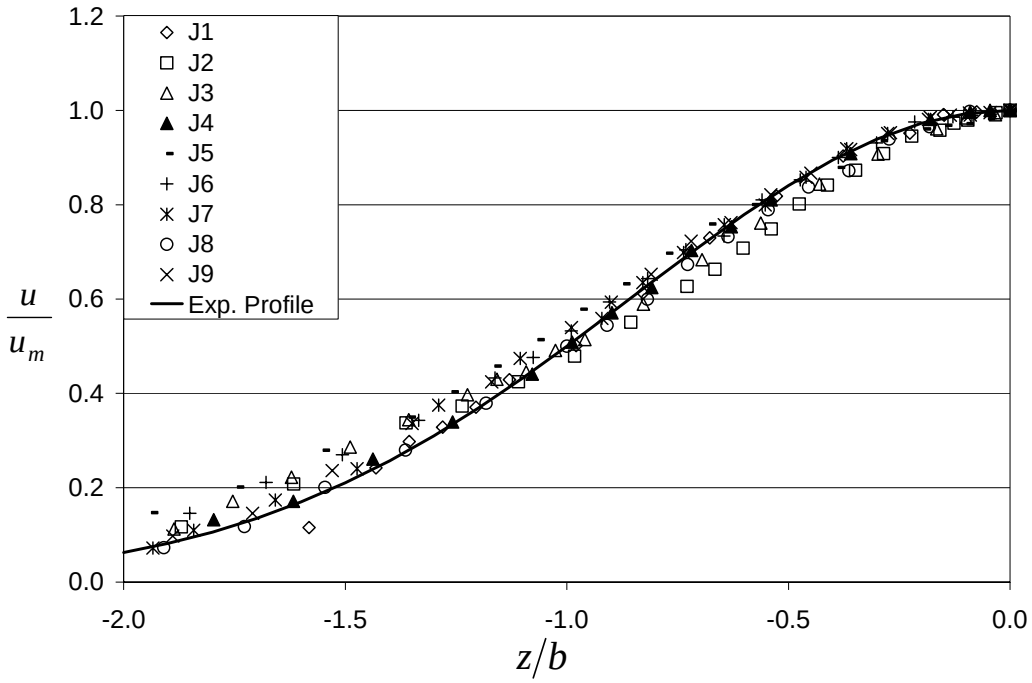

Horizontal Profile for x/d =34

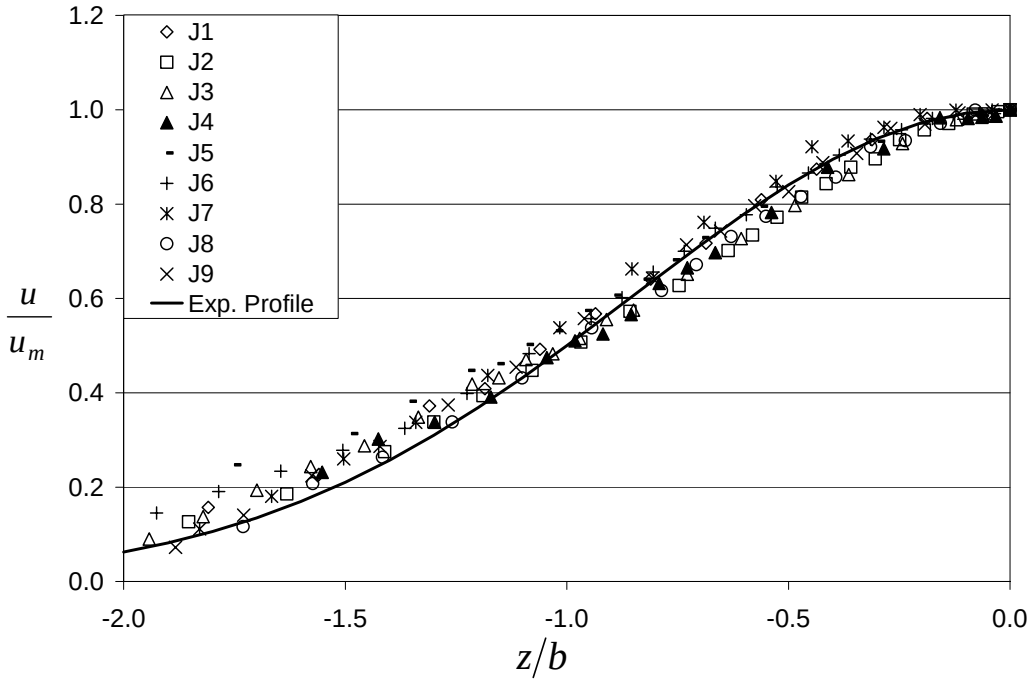

Horizontal Profile for x/d =40

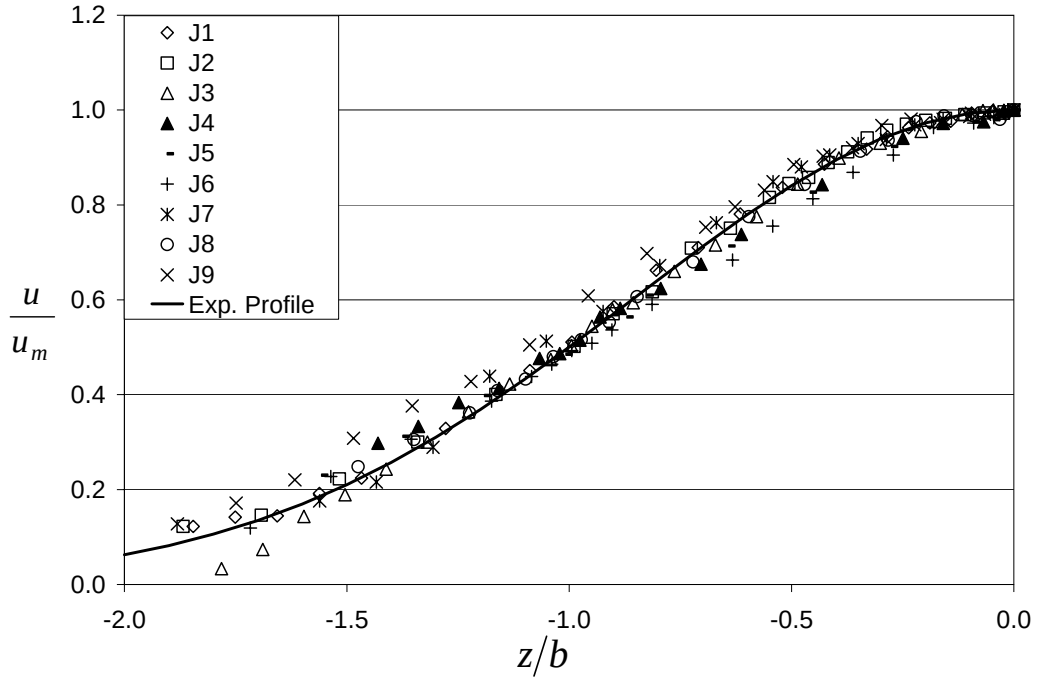

Horizontal Profile for x/d =50

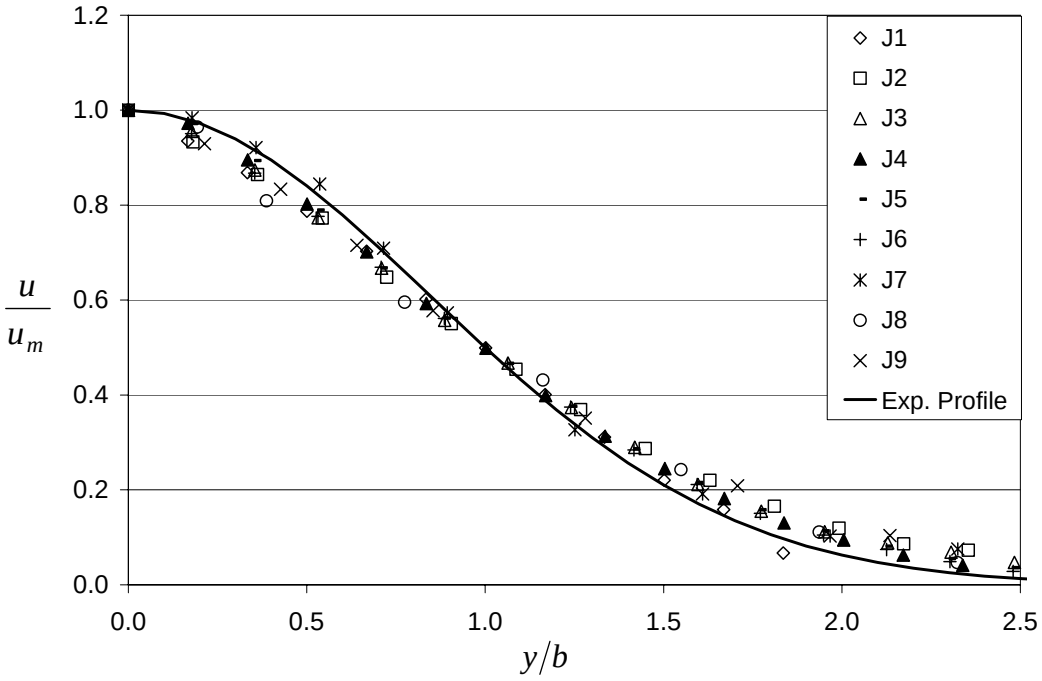

Vertical Profile for x/d =6

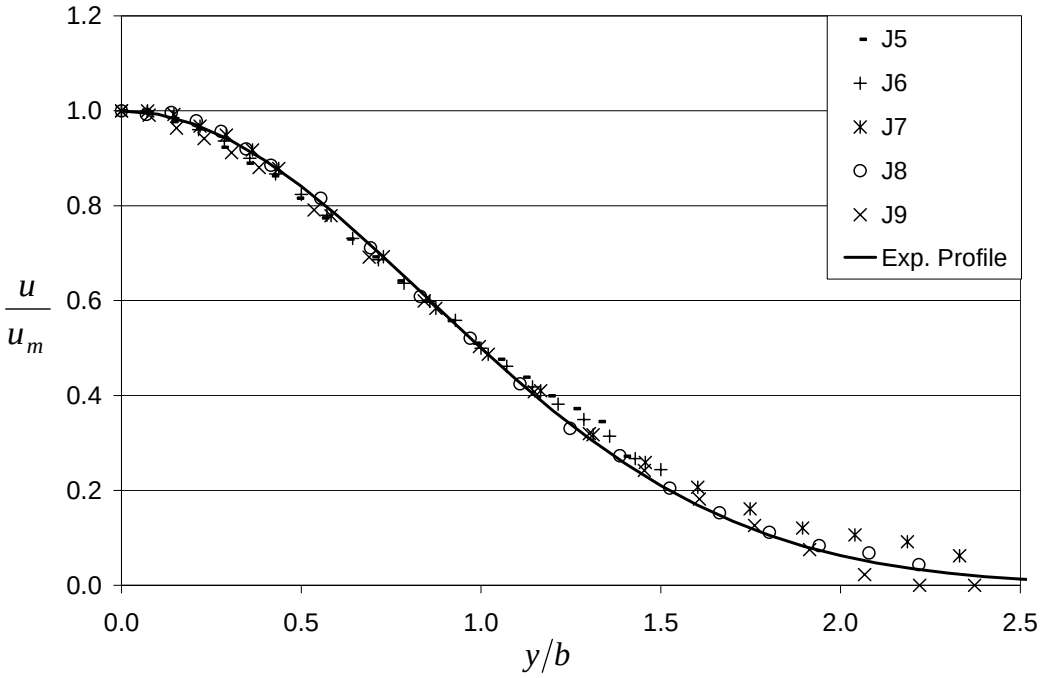

Vertical Profile for x/d =16

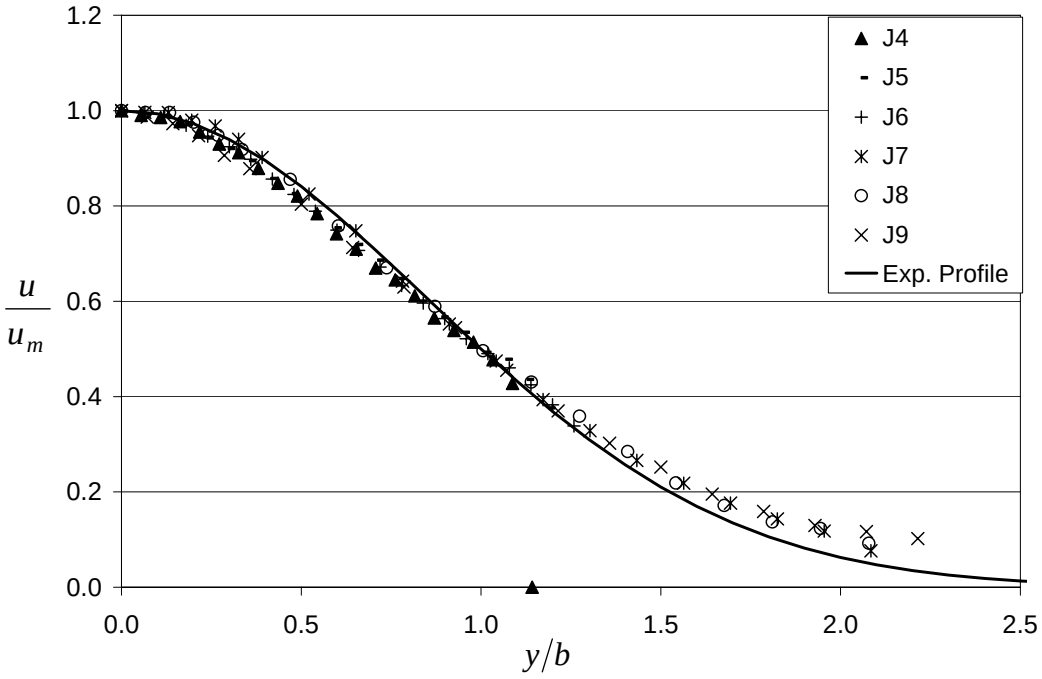

Vertical Profile for x/d =18

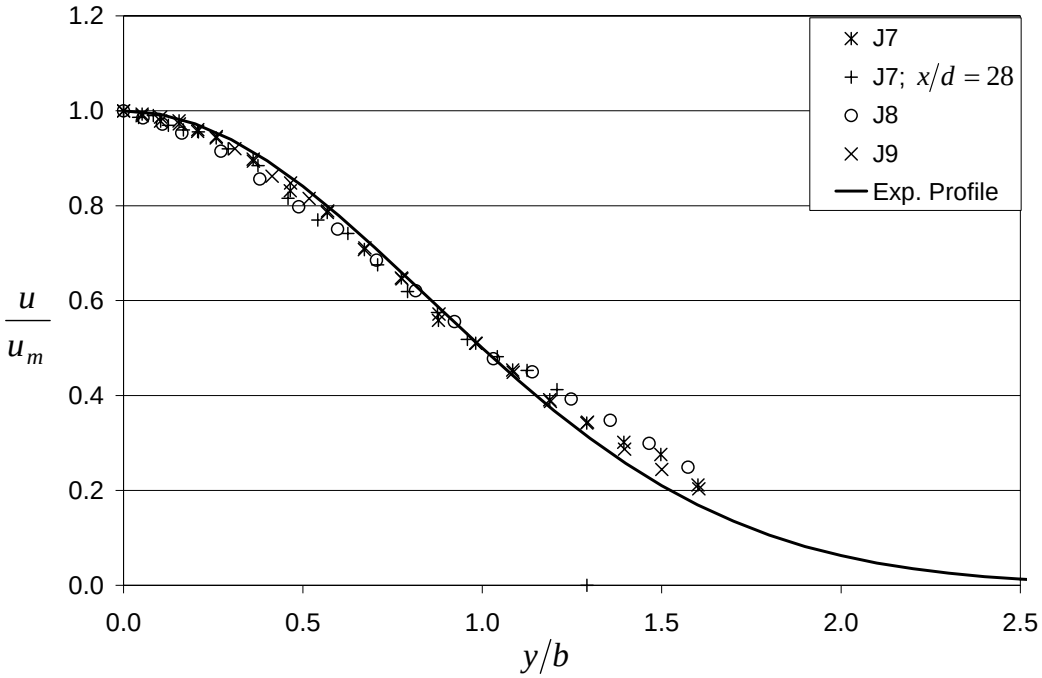

Vertical Profile for x/d =24

Appendix B

Power Law Fits

Below are the power law fits of the vertical profiles below the nozzle for all tests not shown in the text.

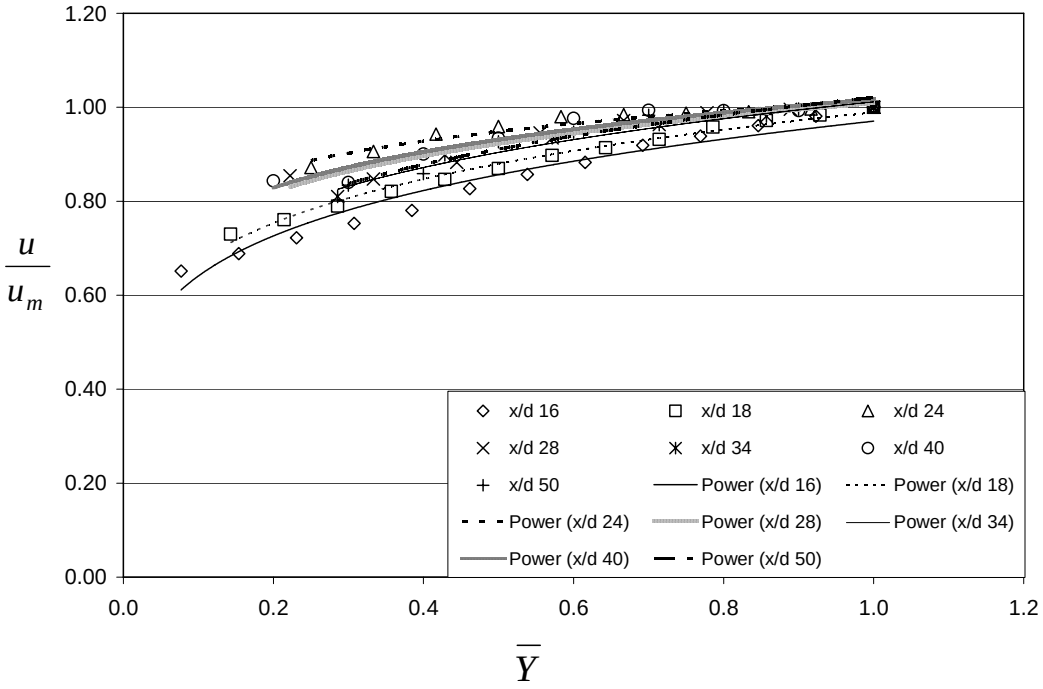

Power Law Fit for Test J1

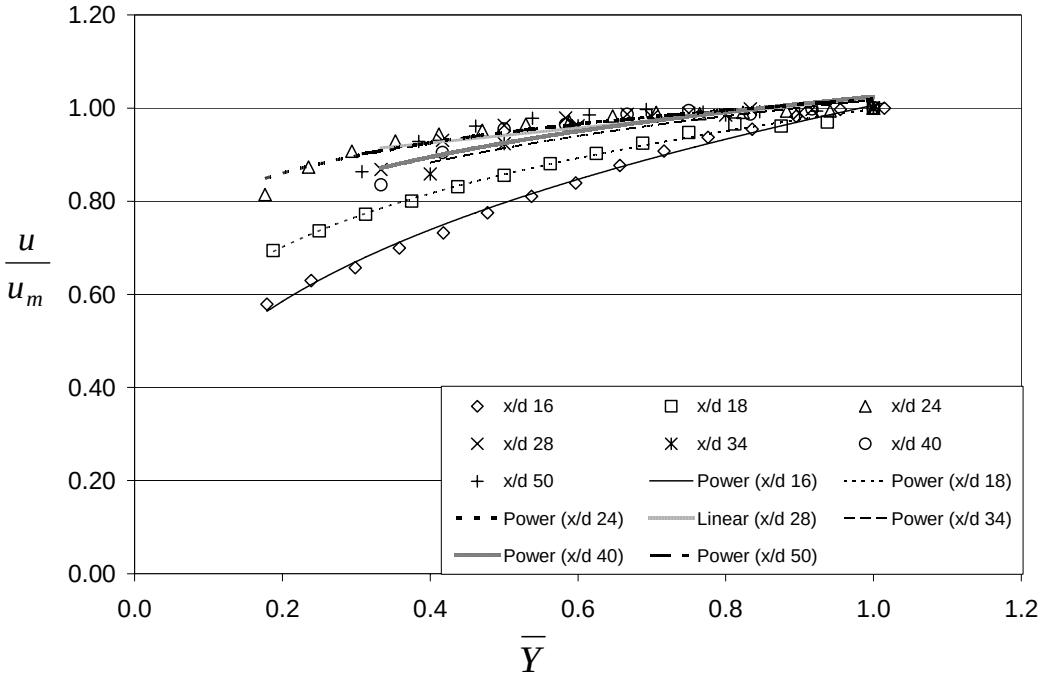

Power Law Fit for Test J2

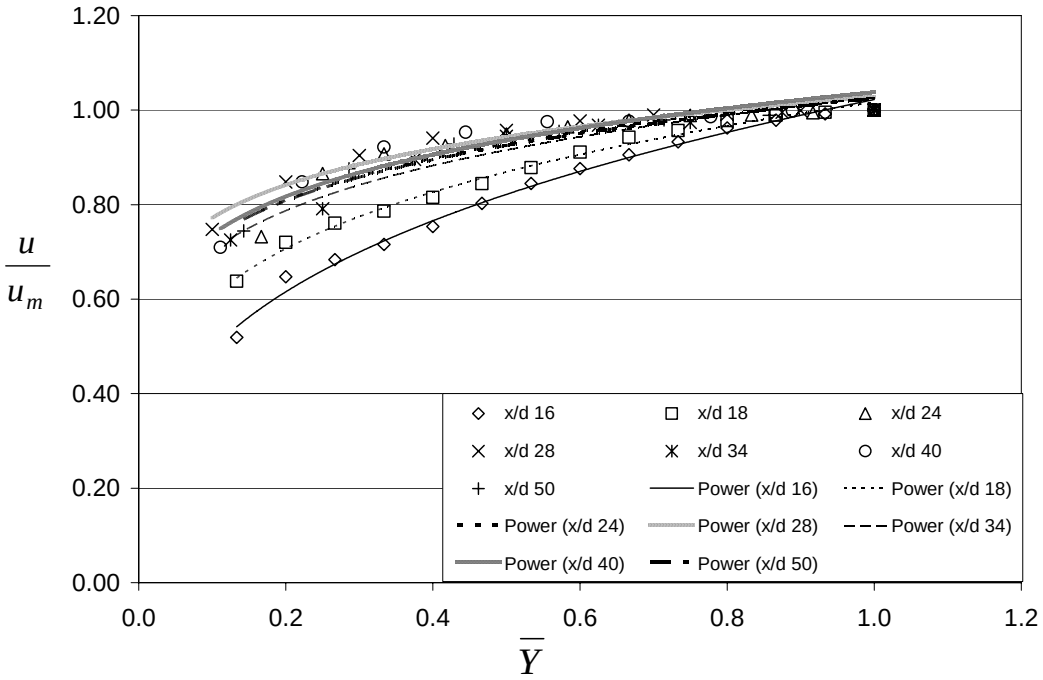

Power Law Fit for Test J3

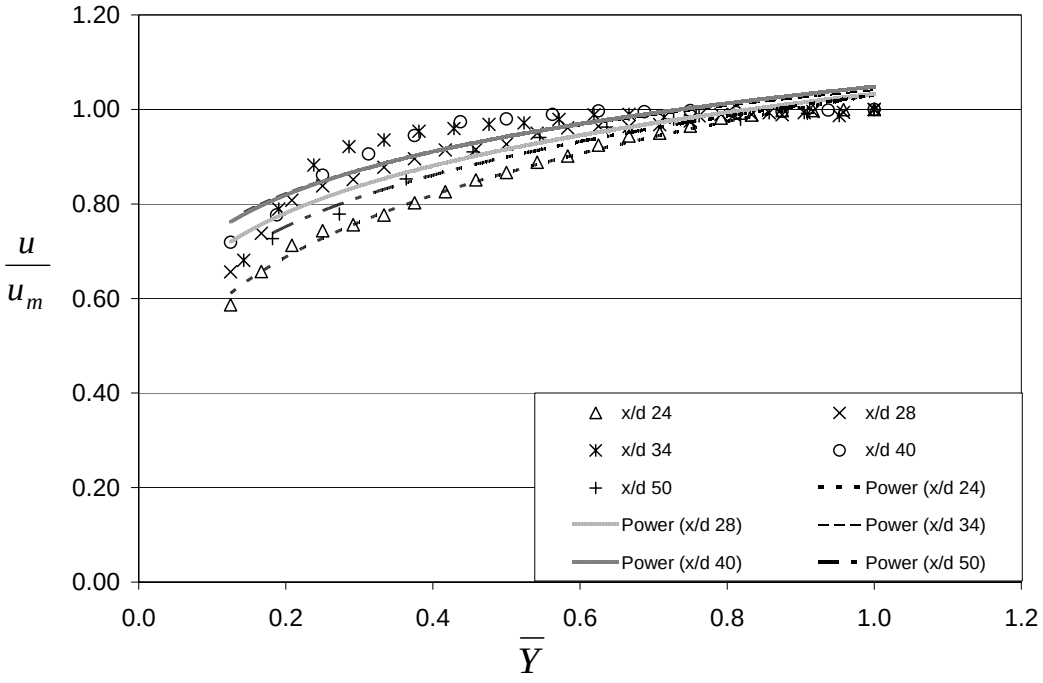

Power Law Fit for Test J4

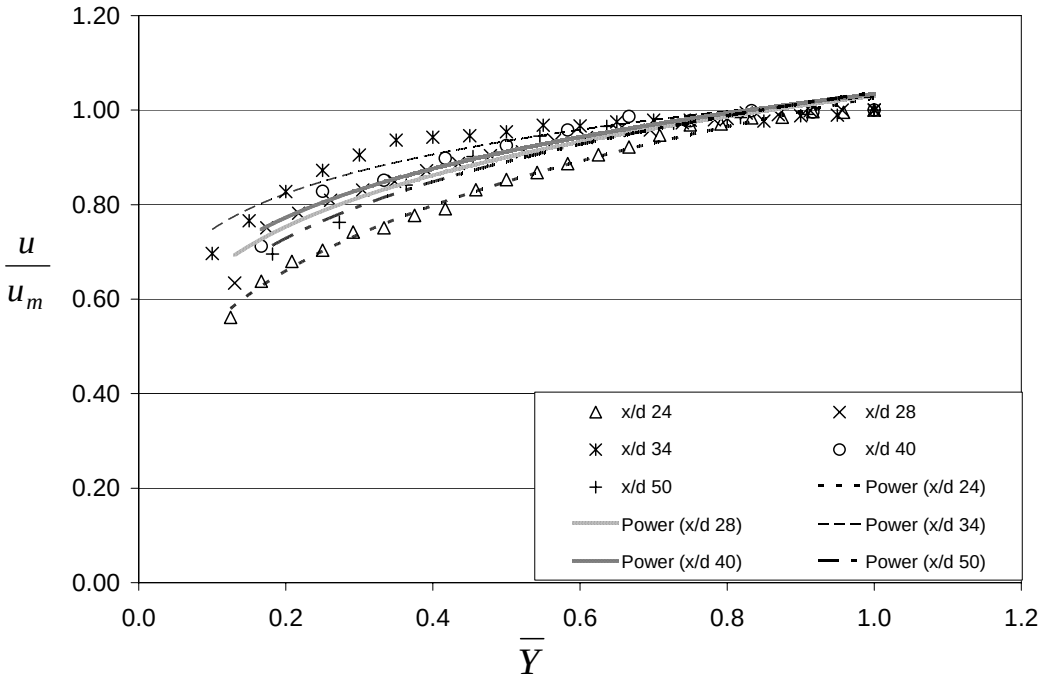

Power Law Fit for Test J5

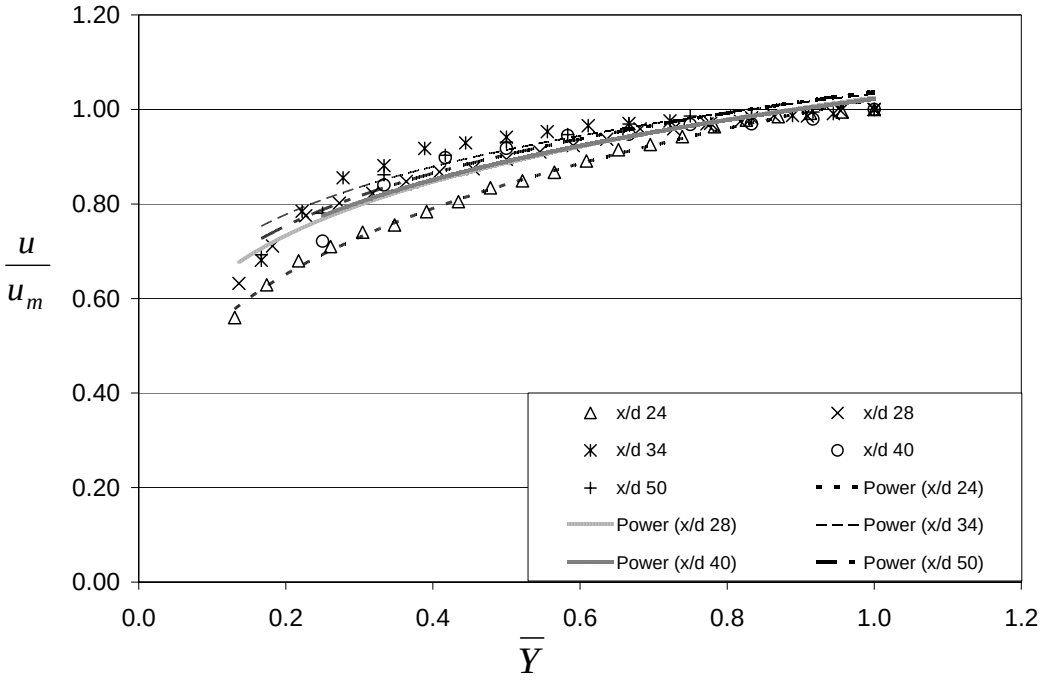

Power Law Fit for Test J6

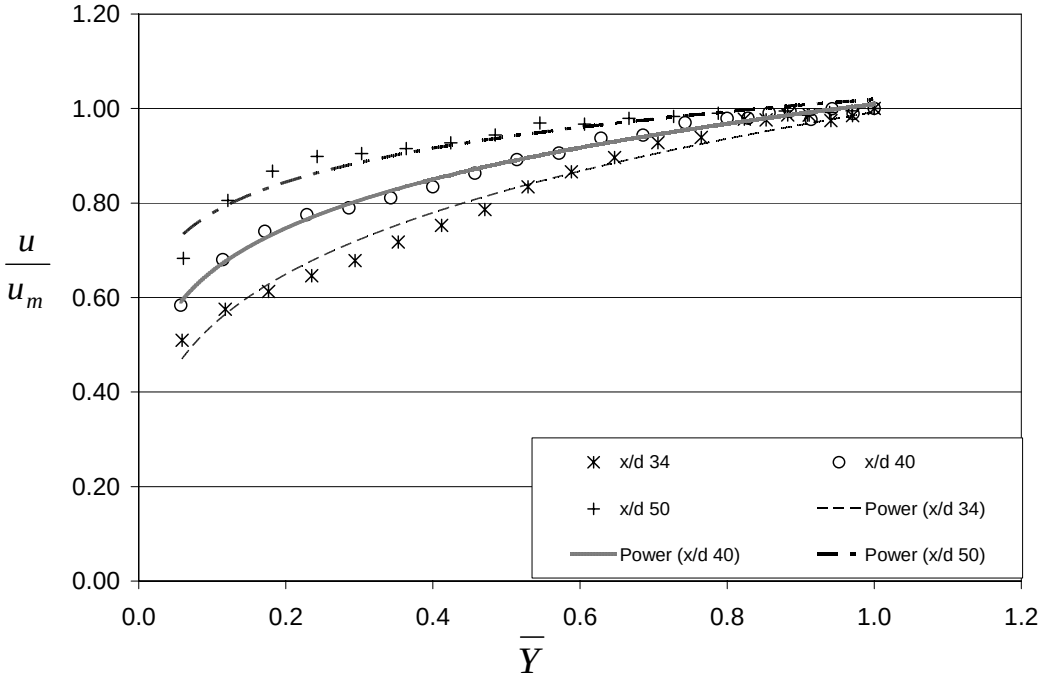

Power Law Fit for Test J7

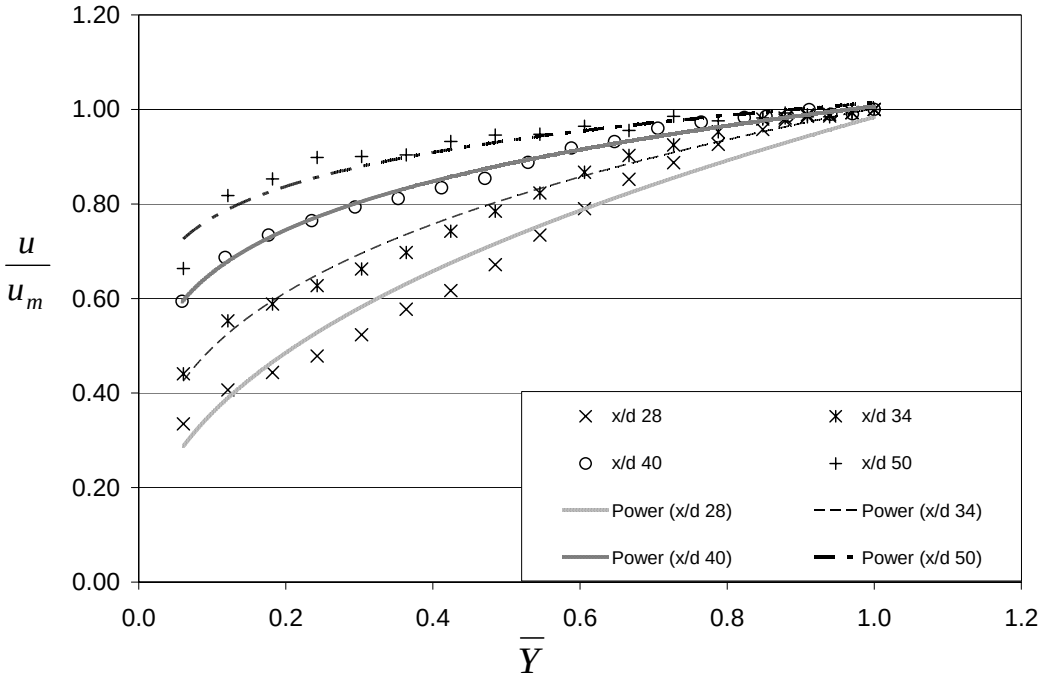

Power Law Fit for Test J9

Appendix C

Similarity Solution

Below are the similarity solutions of the vertical profiles above the nozzle for all tests not shown in the text.

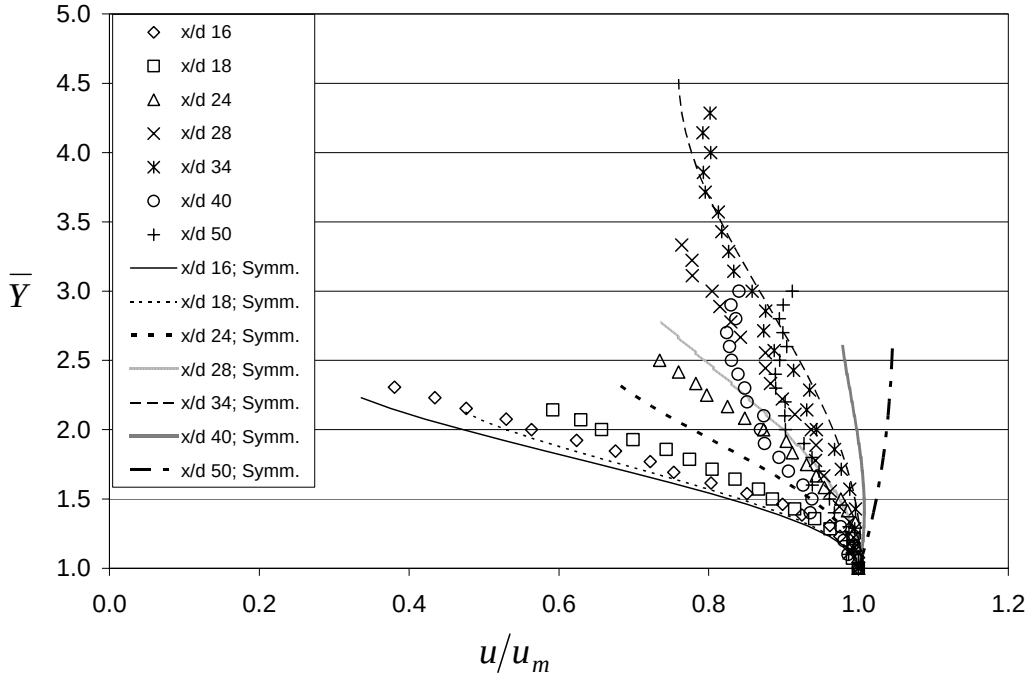

Similarity Solution for Test J1

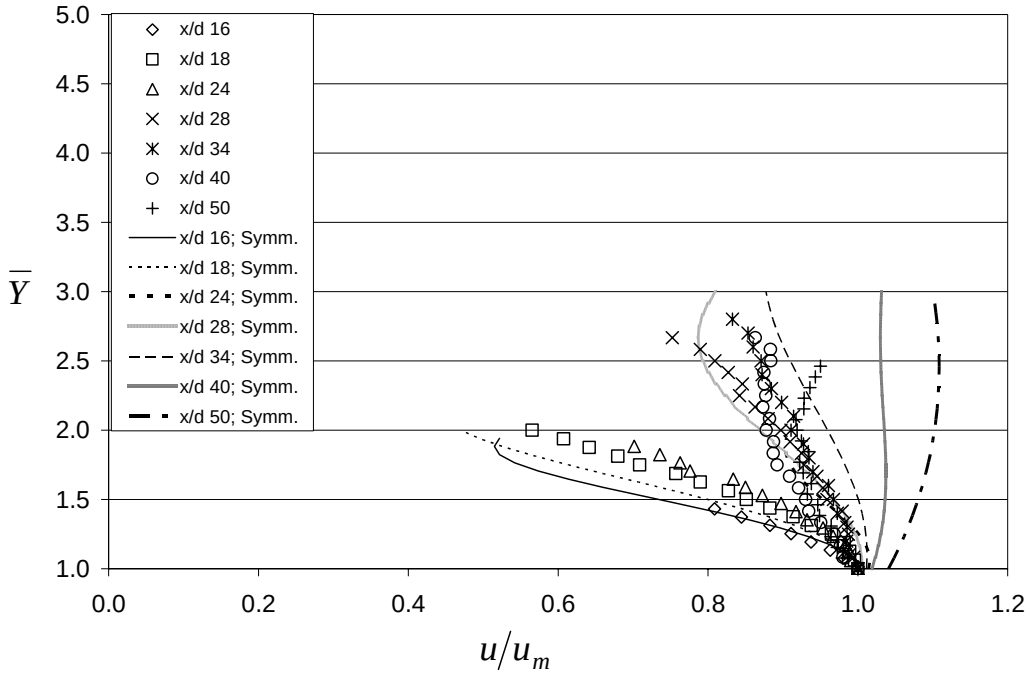

Similarity Solution for Test J2

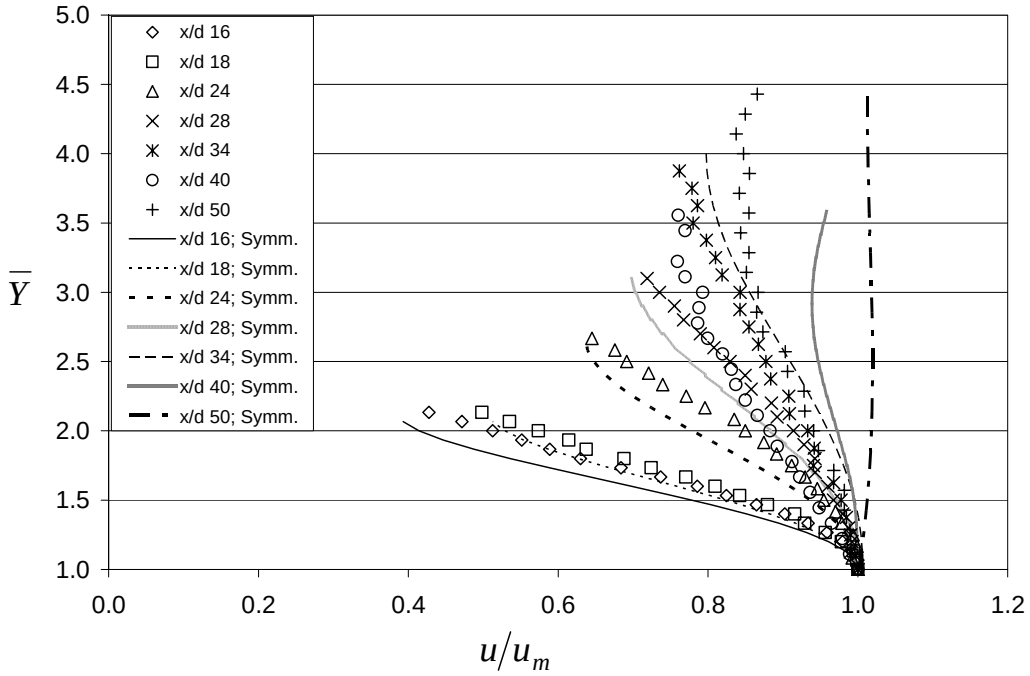

Similarity Solution for Test J3

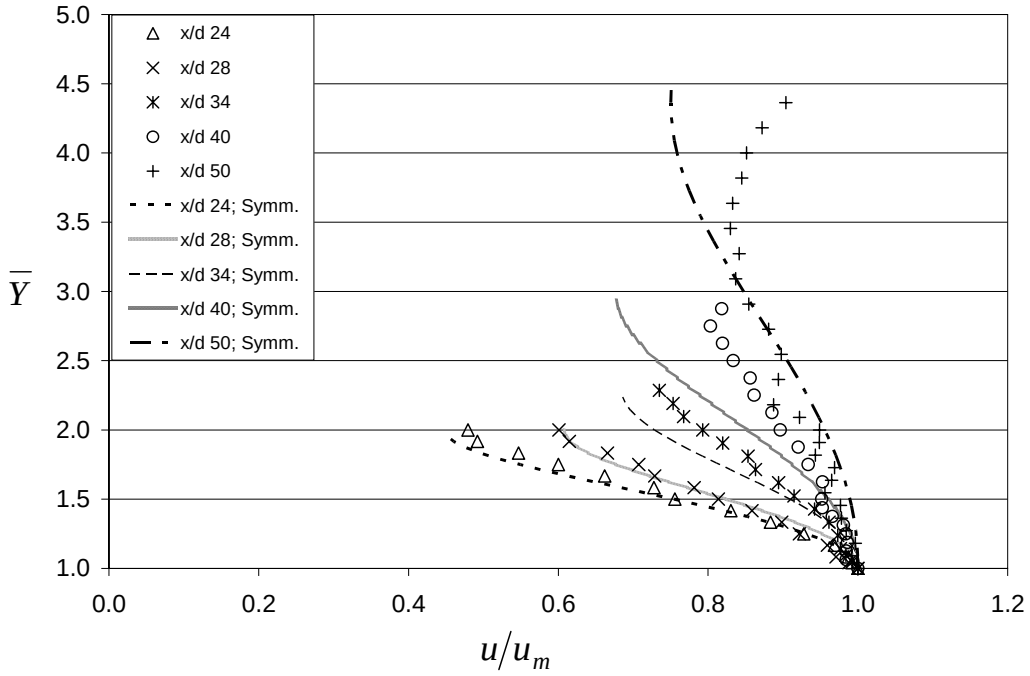

Similarity Solution for Test J4

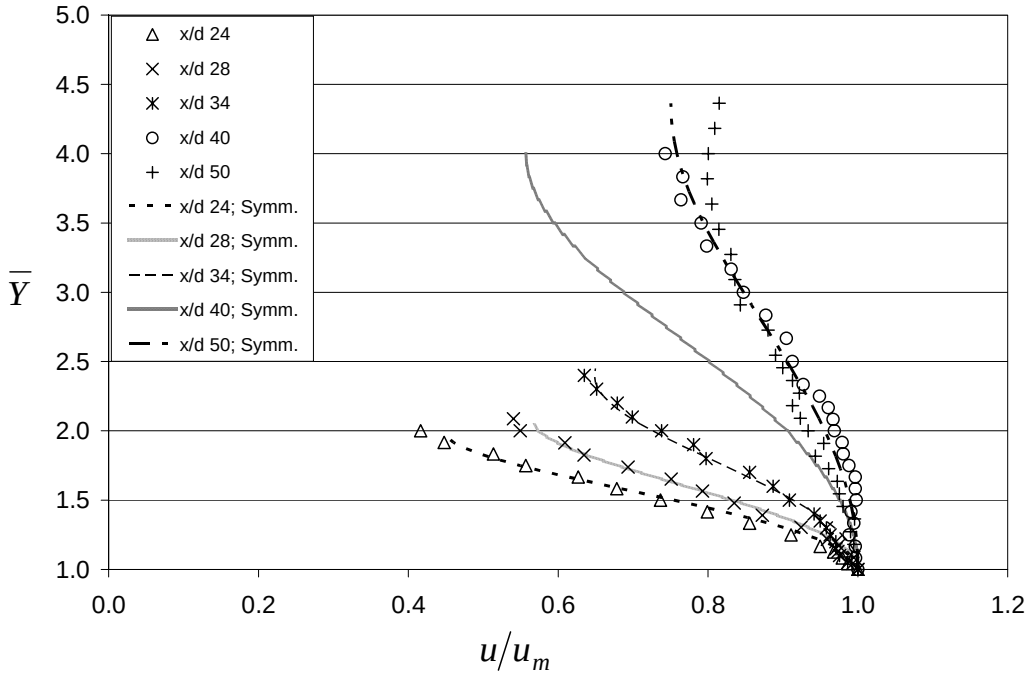

Similarity Solution for Test J5

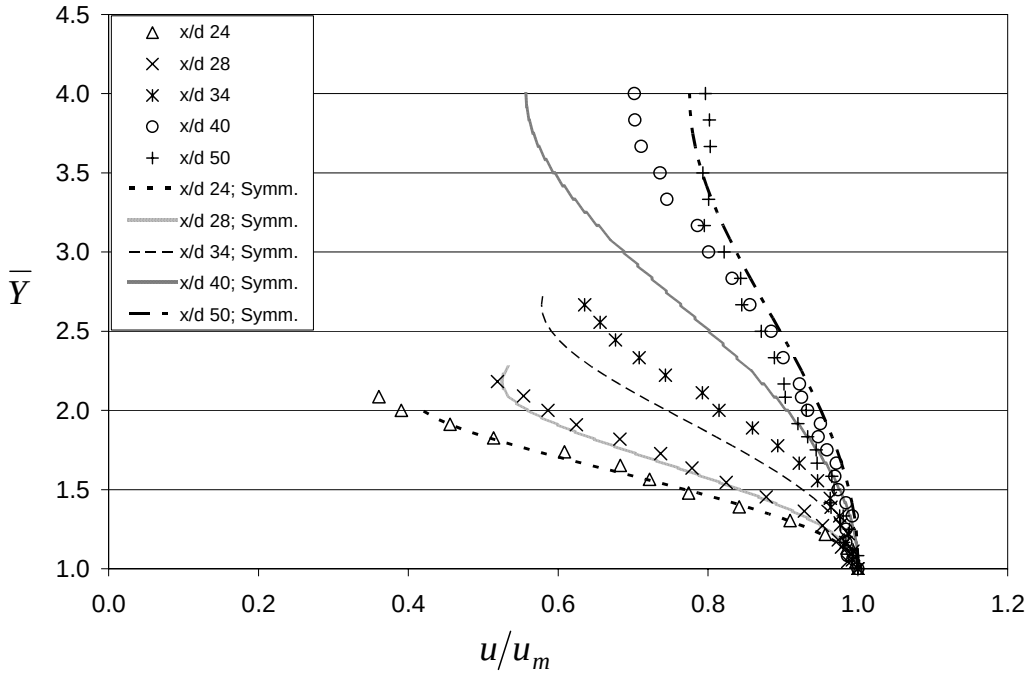

Similarity Solution for Test J6

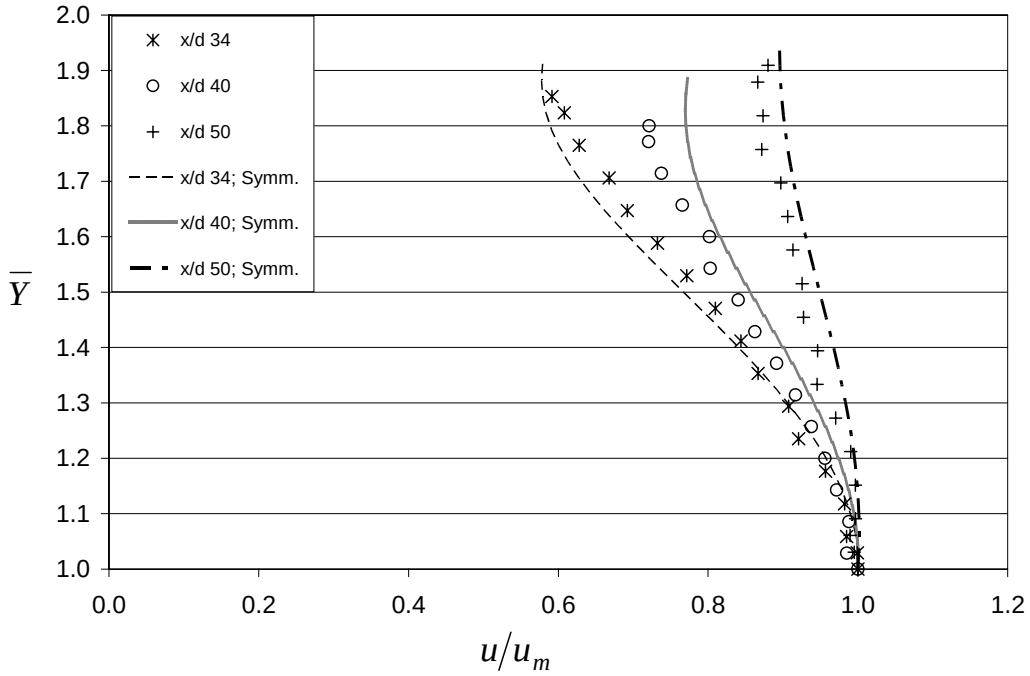

Similarity Solution for Test J7

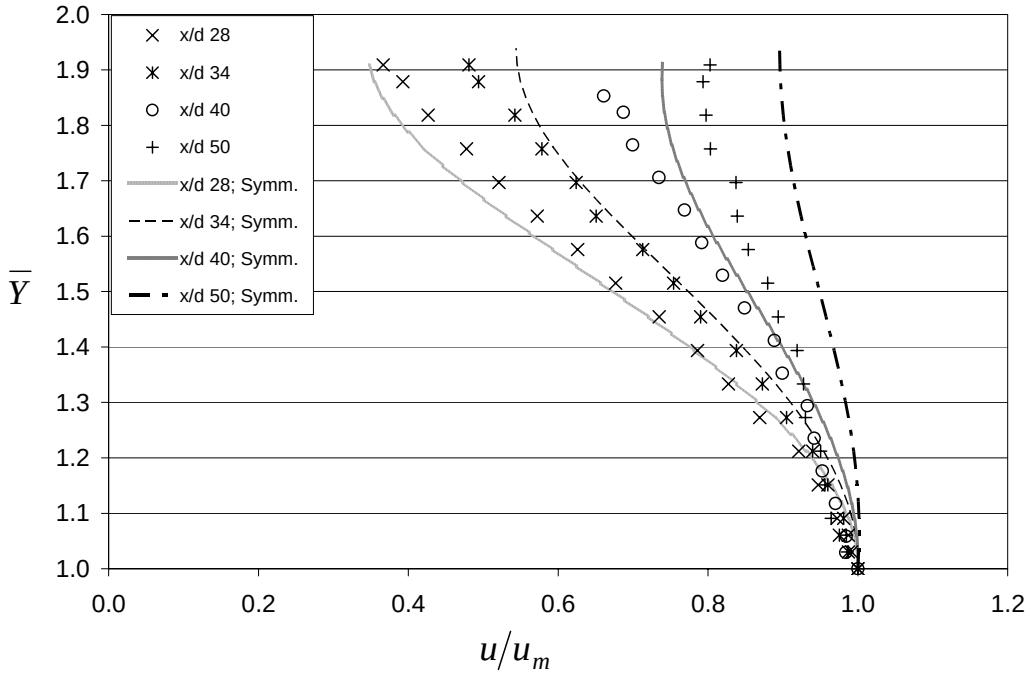

Similarity Solution for Test J9

Appendix D

Relative Error for Turbulent Jets

Below are relative error plots for the plane and circular turbulent jets modeled in this research.

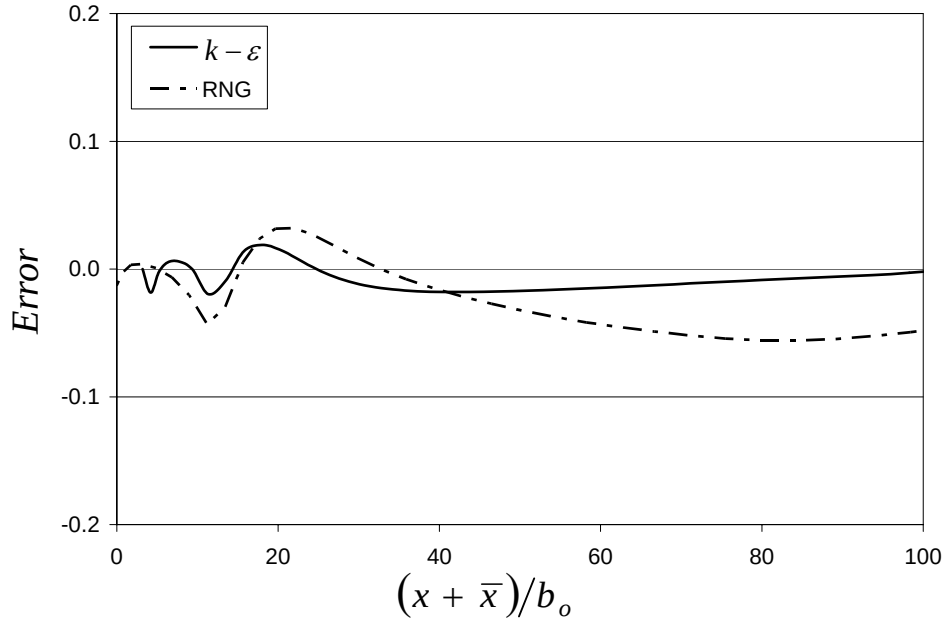

Error Plot of Center Line Velocity Decay
for a Plane Turbulent Jet

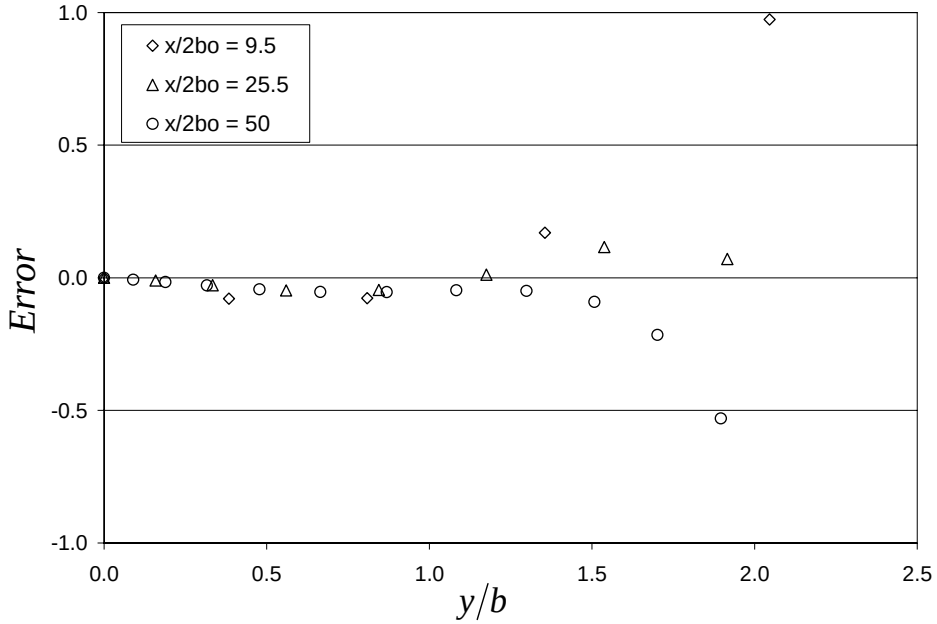

Error Plot of Longitudinal Velocity Profile
for a Plane Turbulent Jet ($k-\varepsilon$)

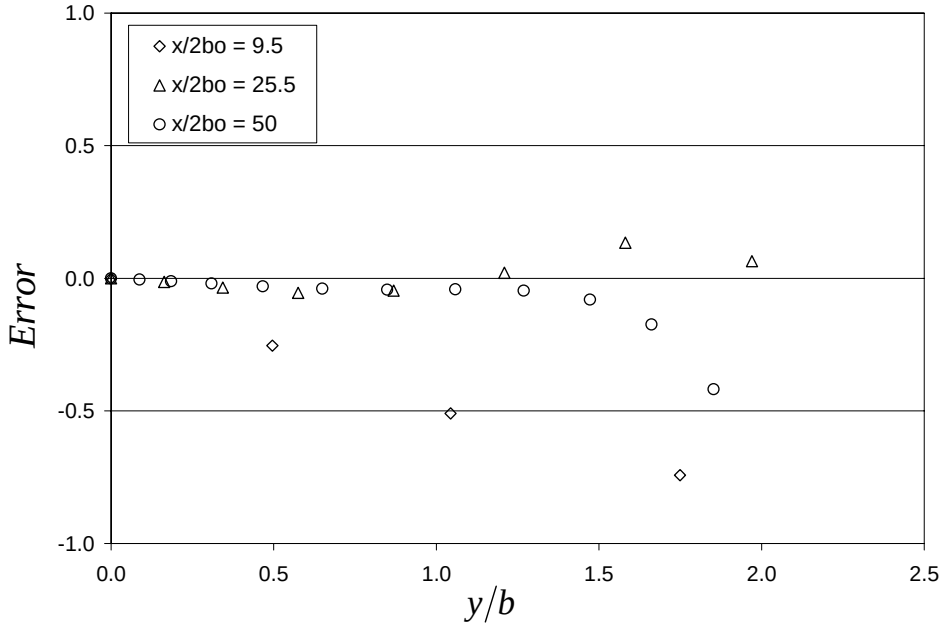

Error Plot of Longitudinal Velocity Profile
for a Plane Turbulent Jet (RNG)

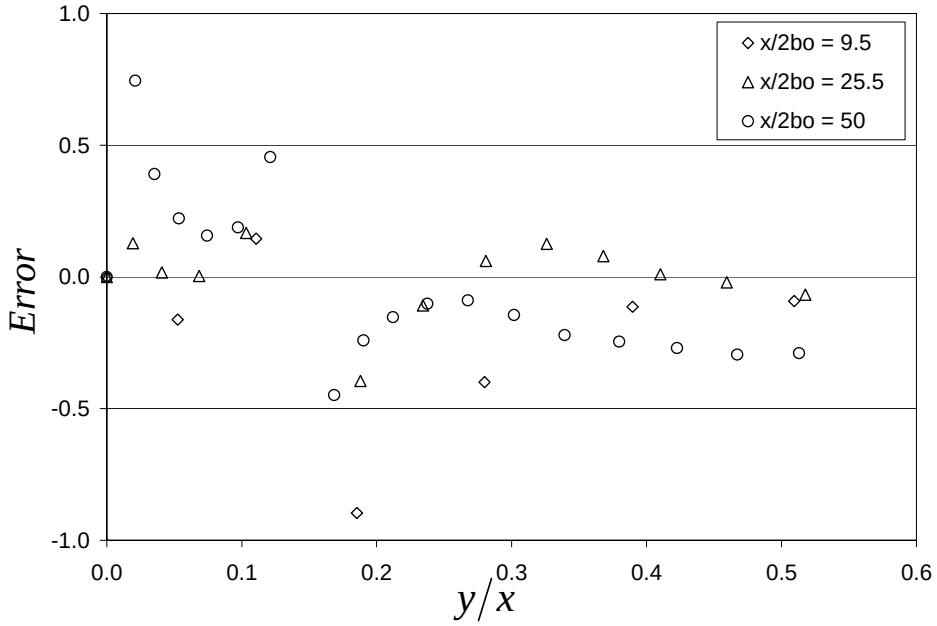

Error Plot of Vertical Velocity Profile
for a Plane Turbulent Jet ($k-\varepsilon$)

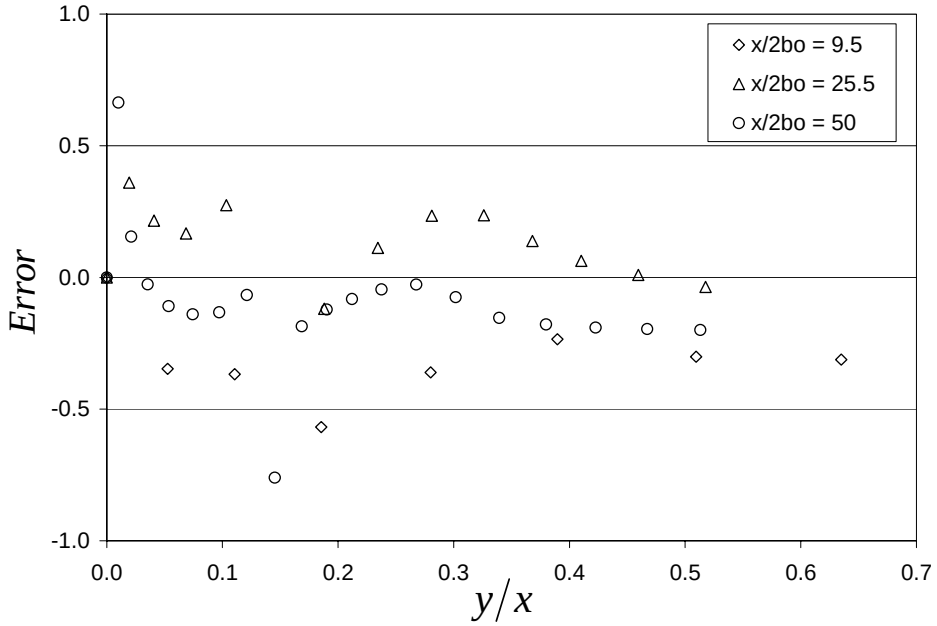

Error Plot of Vertical Velocity Profile
for a Plane Turbulent Jet (RNG)

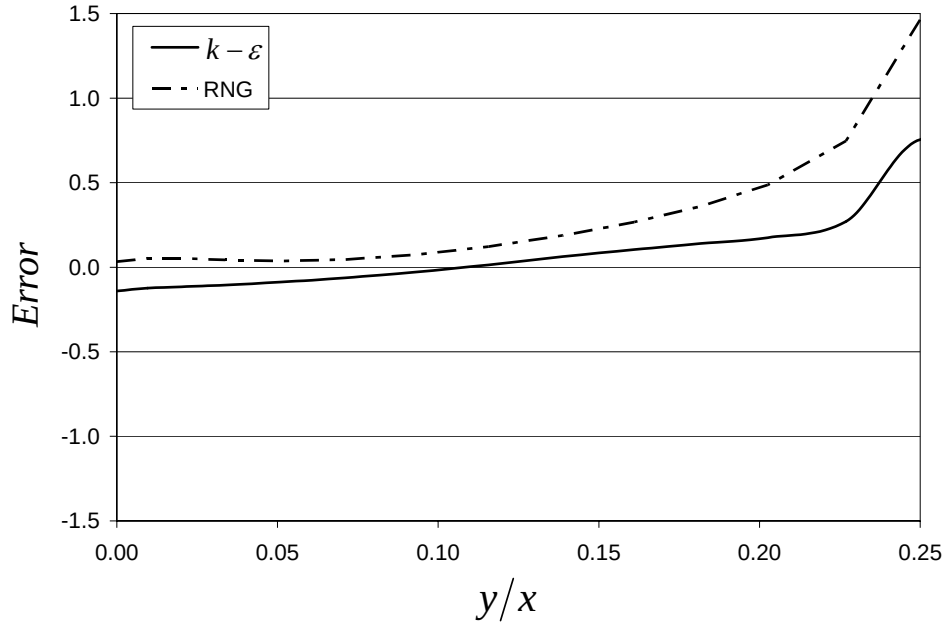

Error Plot of Turbulent Kinetic Energy
for a Plane Turbulent Jet

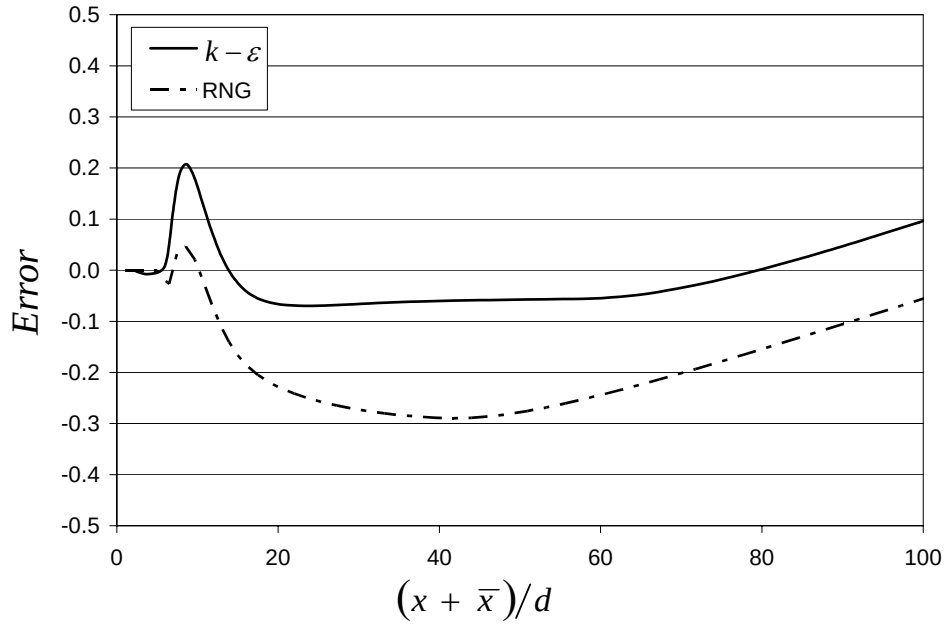

Error Plot of Center Line Velocity Decay
for a Circular Turbulent Jet

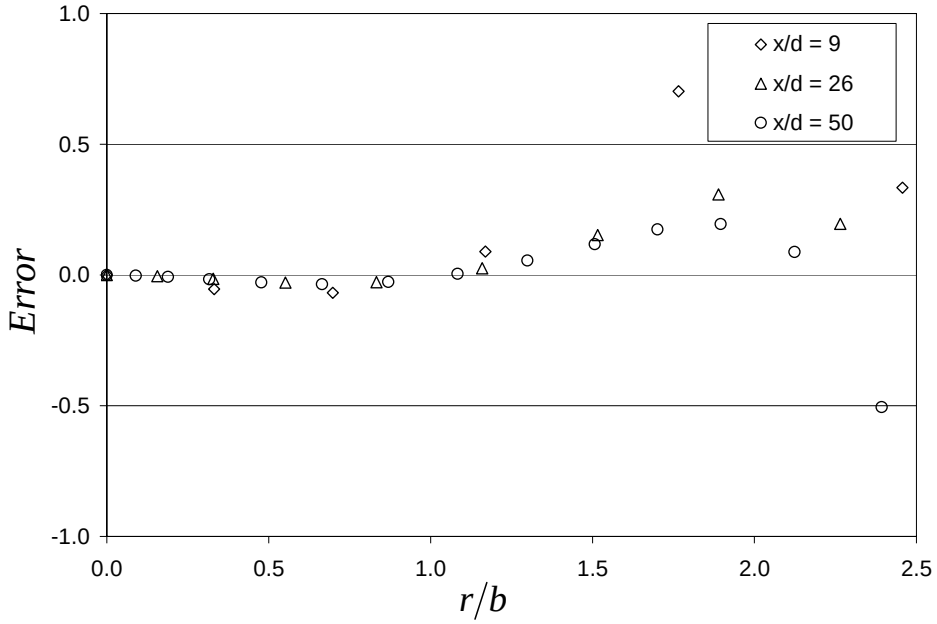

Error Plot of Longitudinal Velocity Profile
for a Circular Turbulent Jet ($k-\varepsilon$)

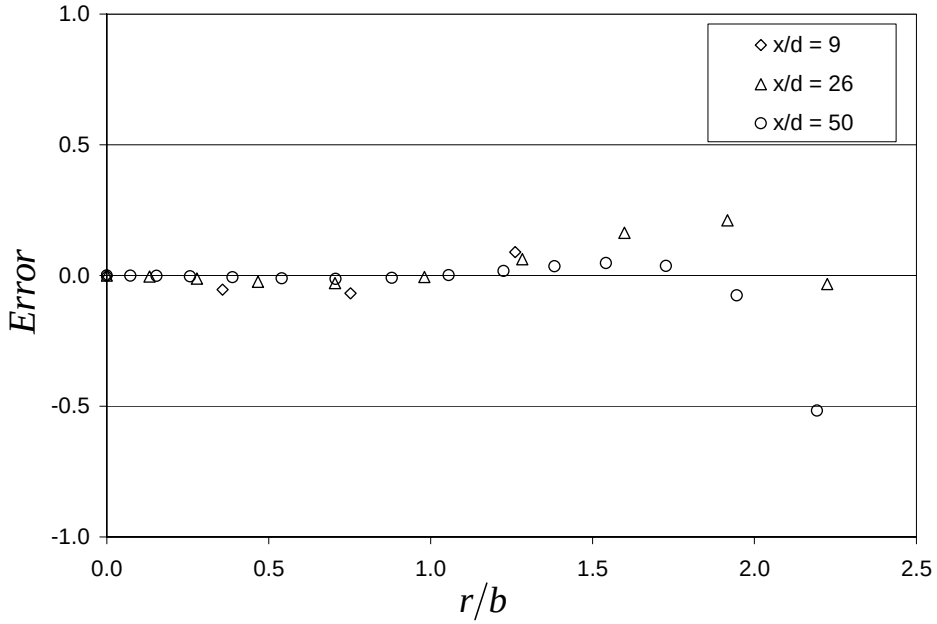

Error Plot of Longitudinal Velocity Profile
for a Circular Turbulent Jet (RNG)

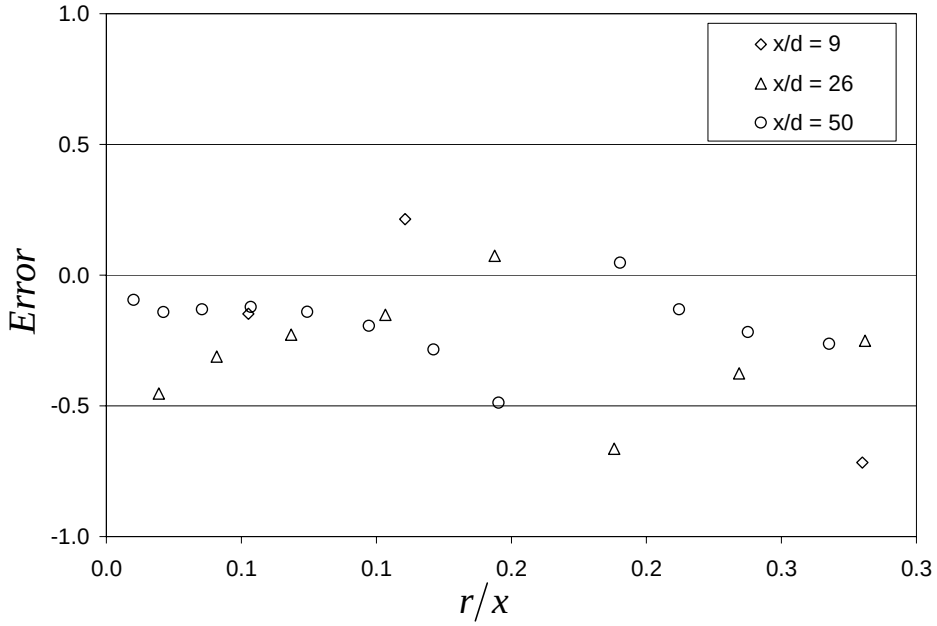

Error Plot of Vertical Velocity Profile
for a Circular Turbulent Jet ($k-\varepsilon$)

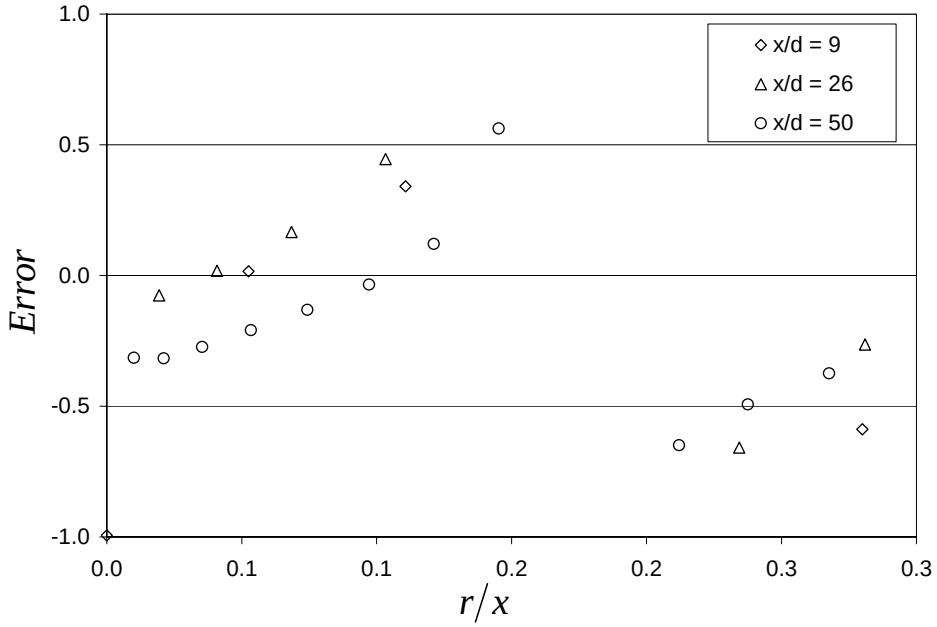

Error Plot of Vertical Velocity Profile
for a Circular Turbulent Jet (RNG)

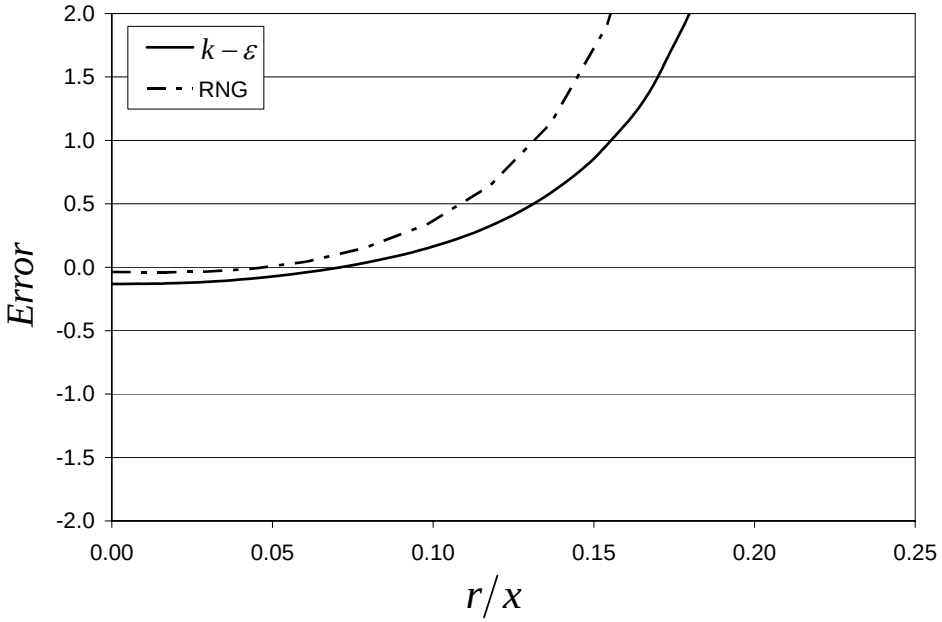

Error Plot of Turbulent Kinetic Energy
for a Circular Turbulent Jet
Velocity for Test 3

Appendix E

Relative Error for Submerged Hydraulic Jump

Below are relative error plots at representative location for the submerged hydraulic jump cases modeled in this research.

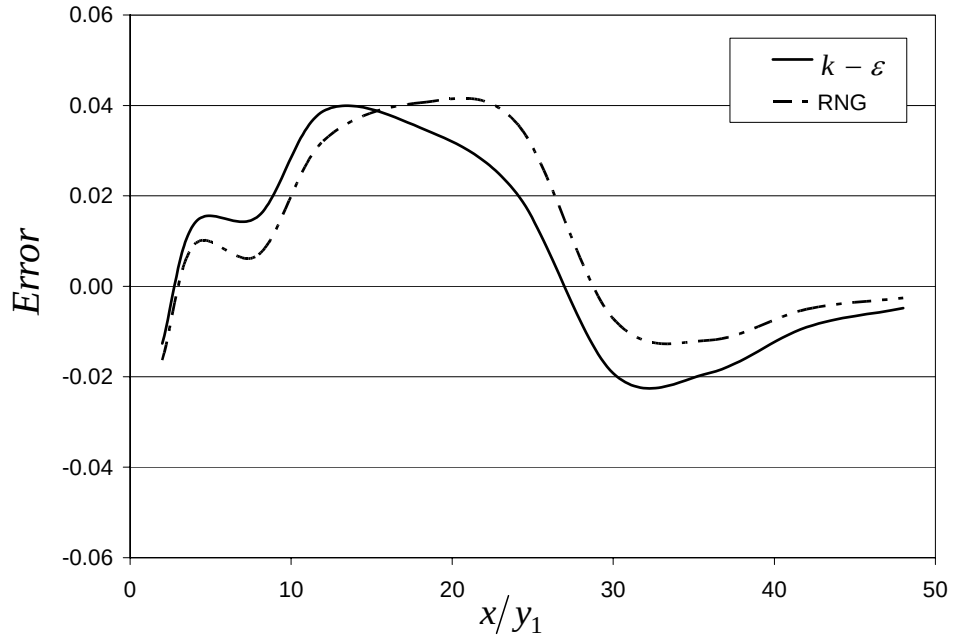

Error Plot of Water Surface Profile for Test 1

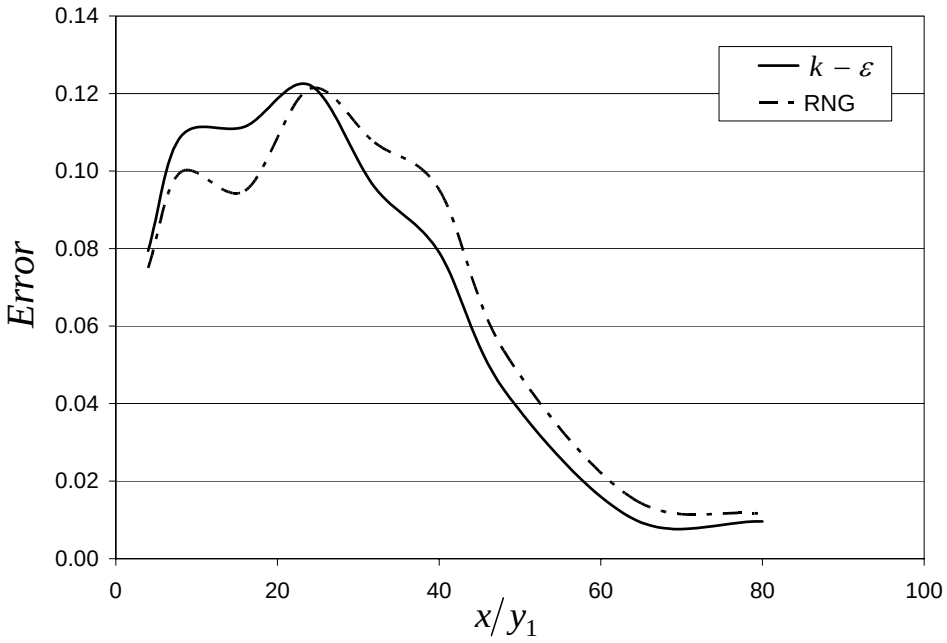

Error Plot of Water Surface Profile for Test 2

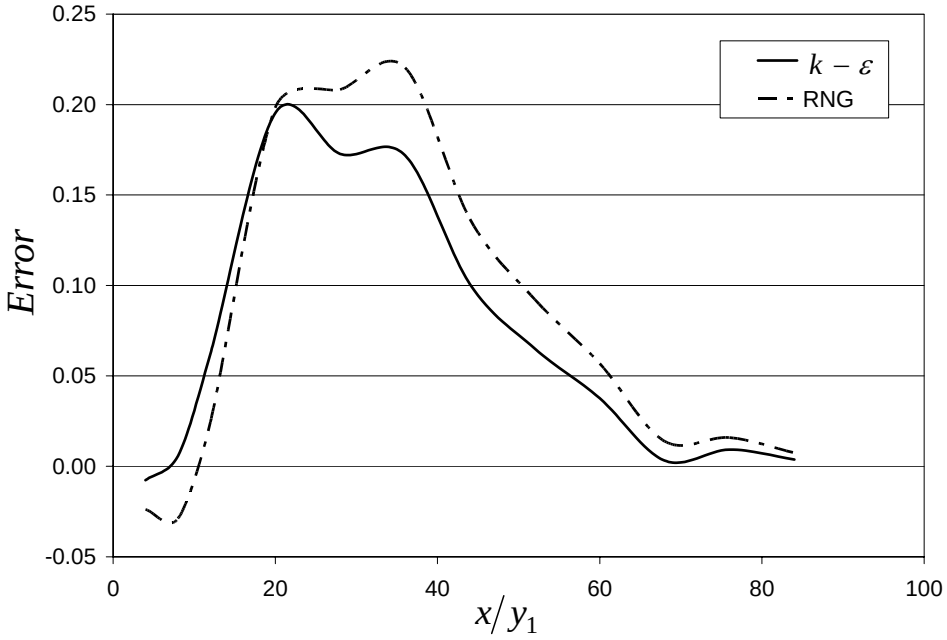

Error Plot of Water Surface Profile for Test 3

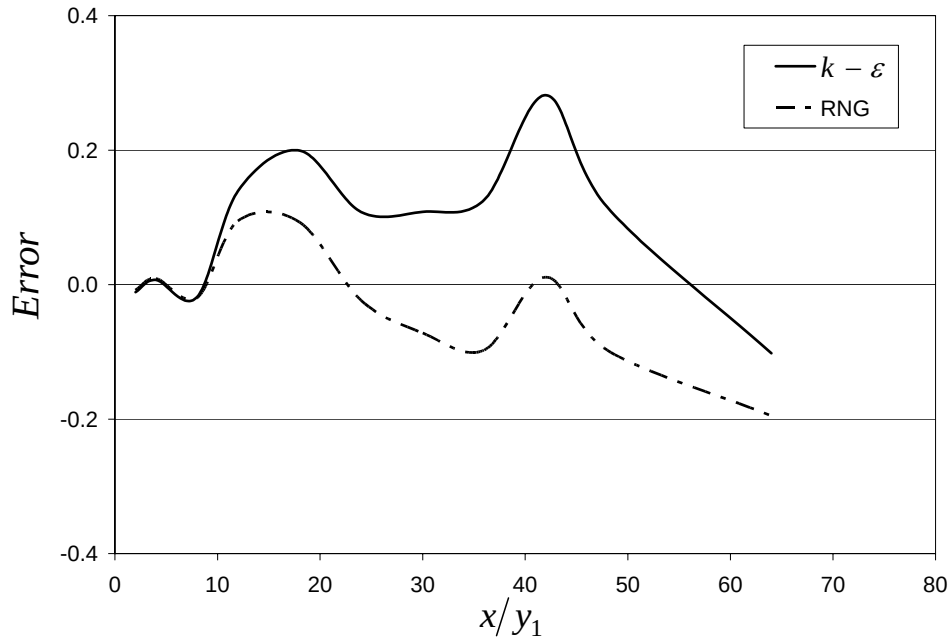

Error Plot of Maximum Longitudinal Velocity for Test 1

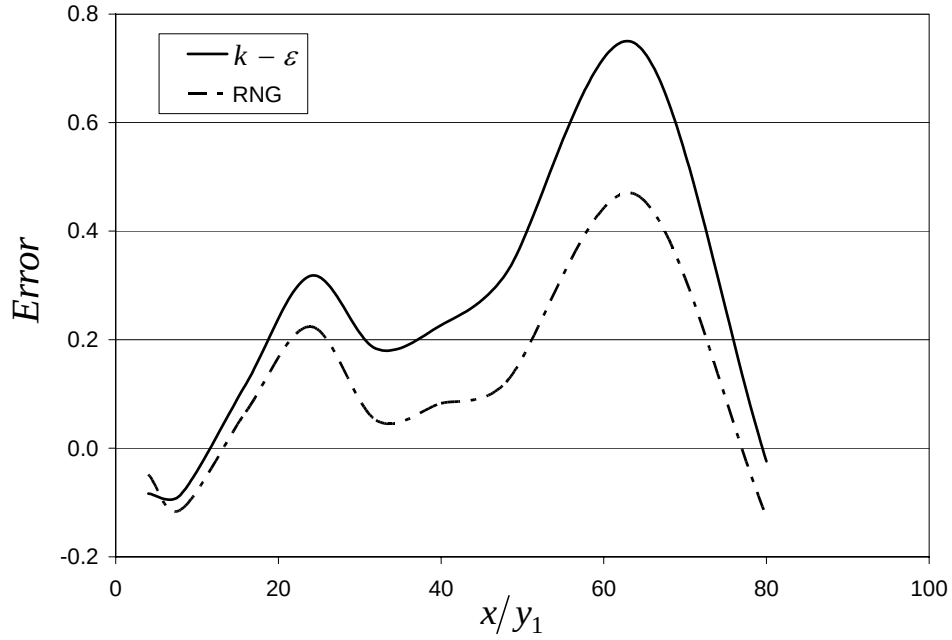

Error Plot of Maximum Longitudinal Velocity for Test 2

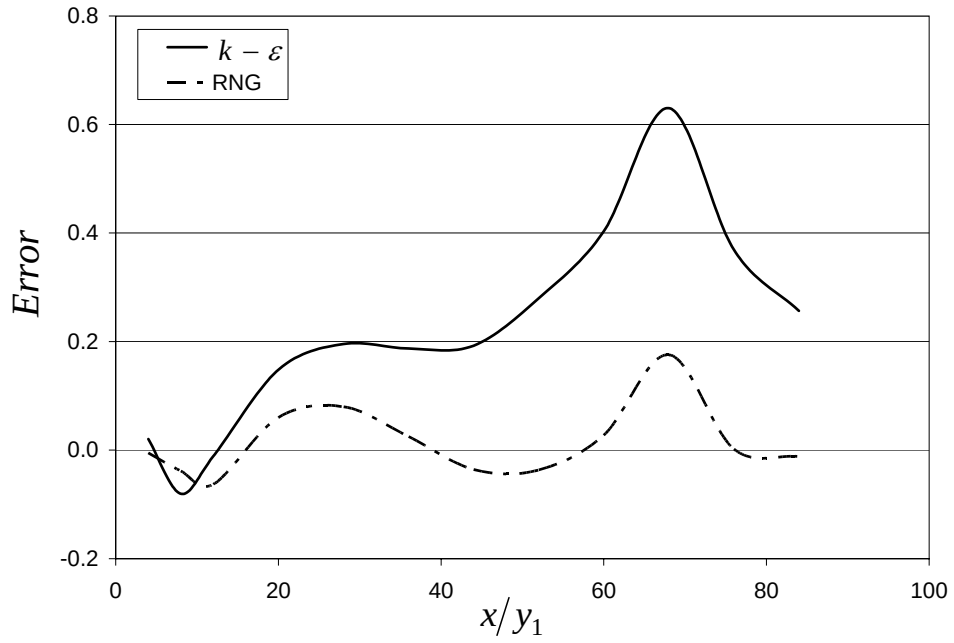

Error Plot of Maximum Longitudinal

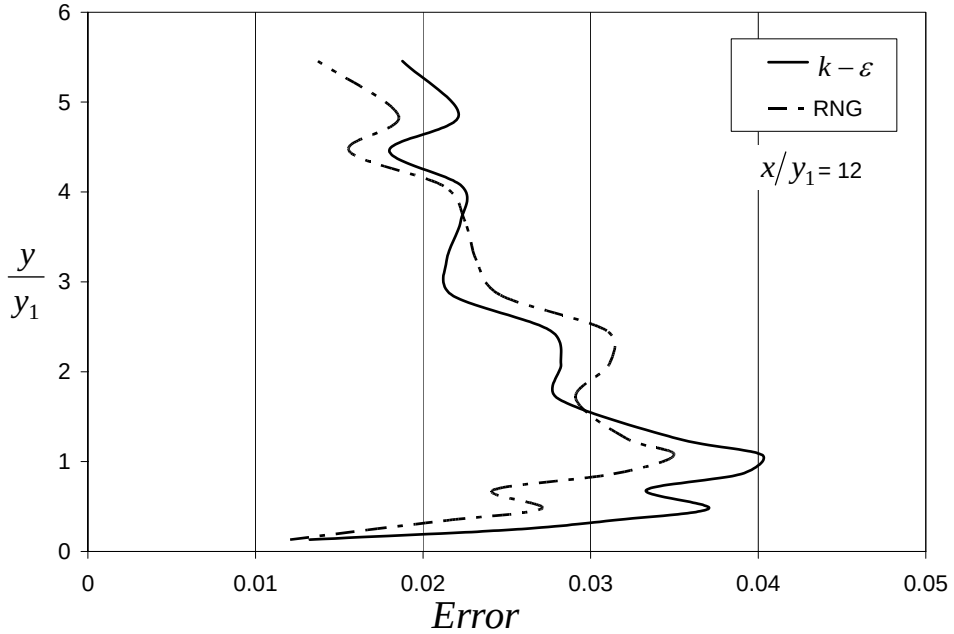

Error Plot of Longitudinal Velocity for Test 1

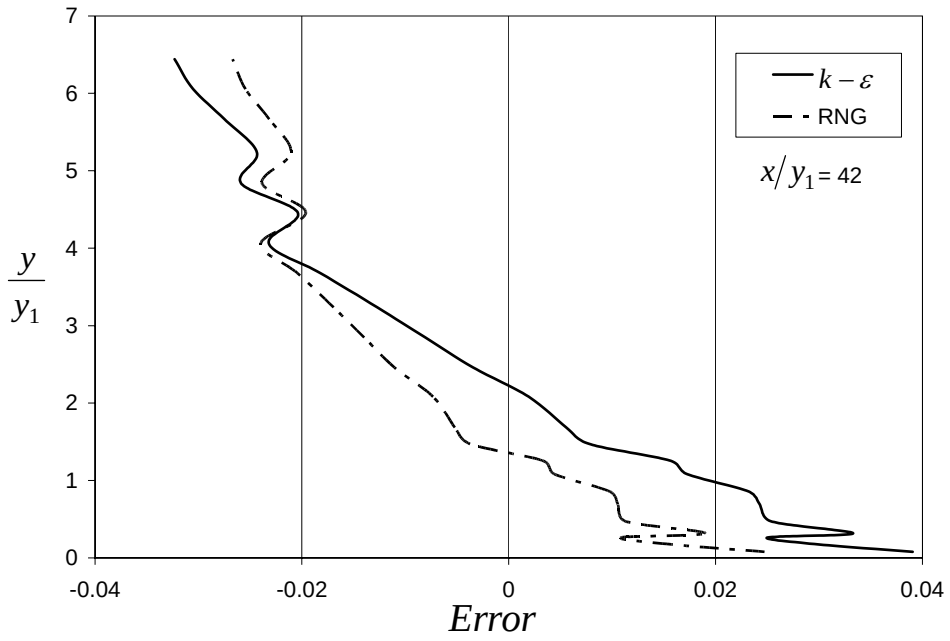

Error Plot of Longitudinal Velocity for Test 1

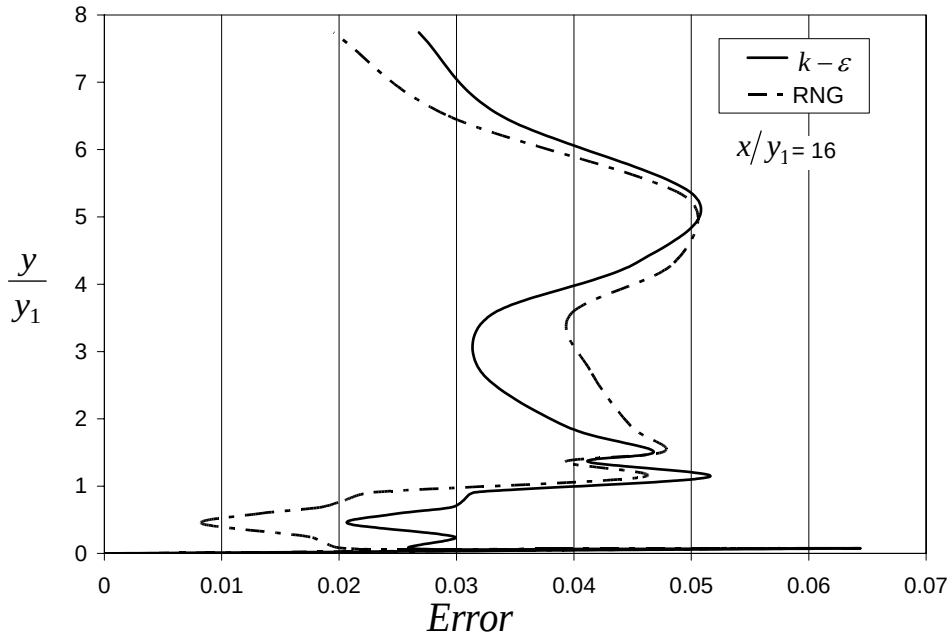

Error Plot of Longitudinal Velocity for Test 2

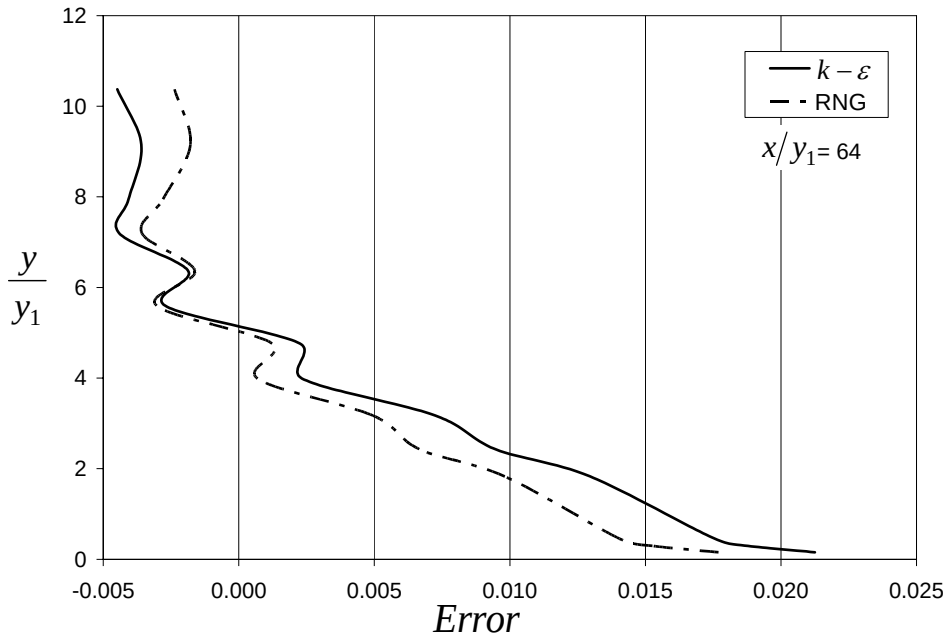

Error Plot of Longitudinal Velocity for Test 2

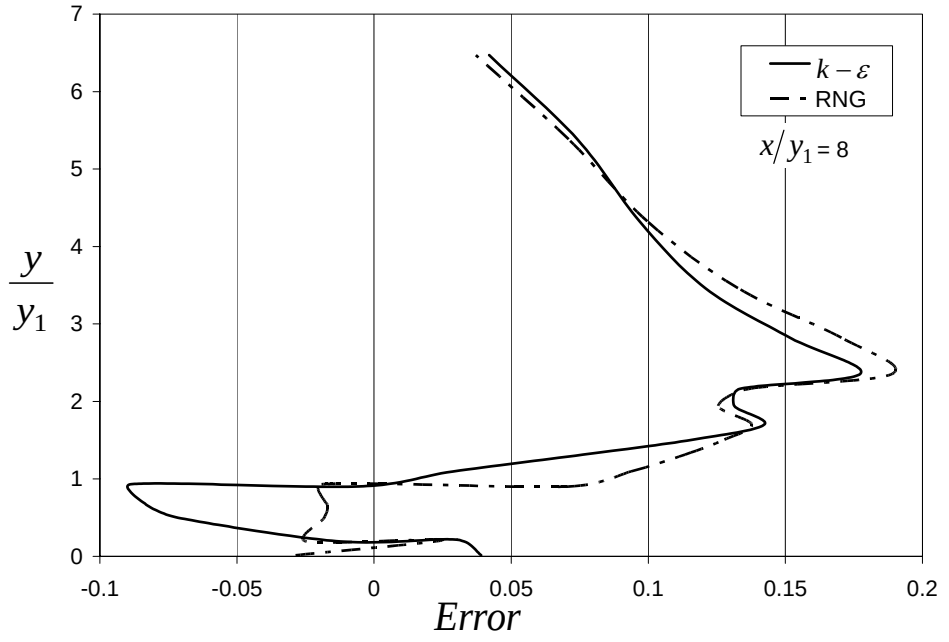

Error Plot of Longitudinal Velocity for Test 3

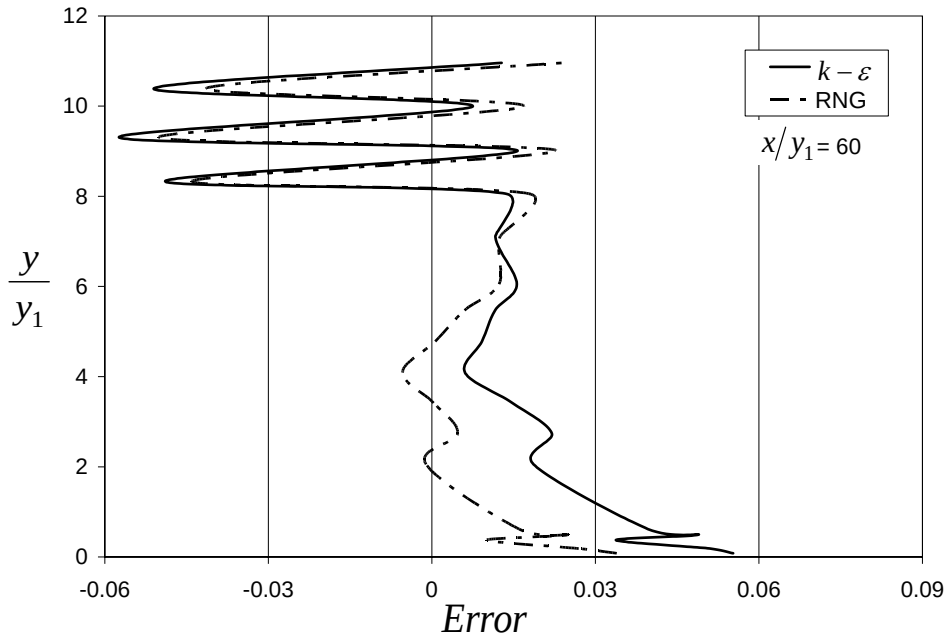

Error Plot of Longitudinal Velocity for Test 3

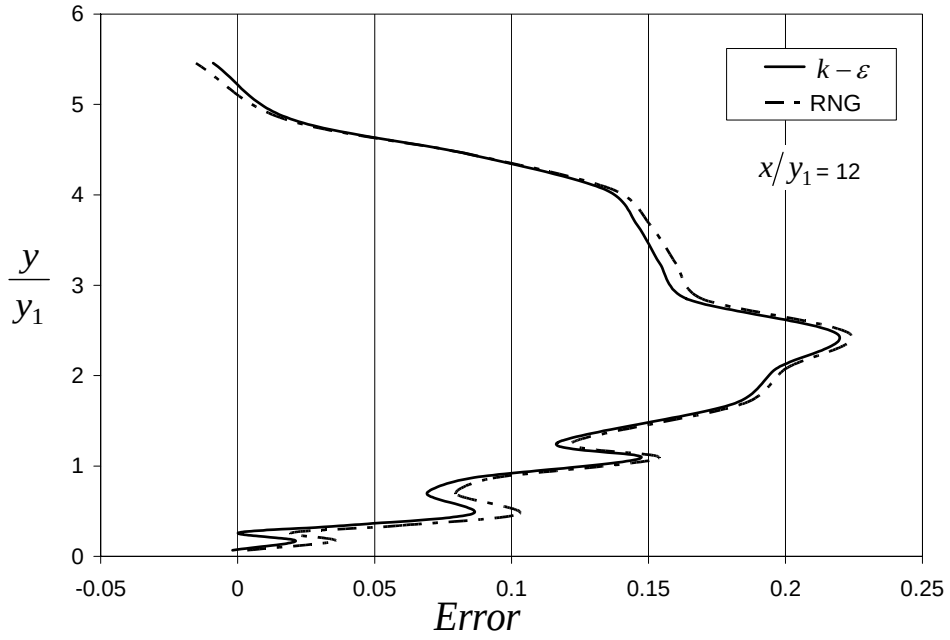

Error Plot of Vertical Velocity for Test 1

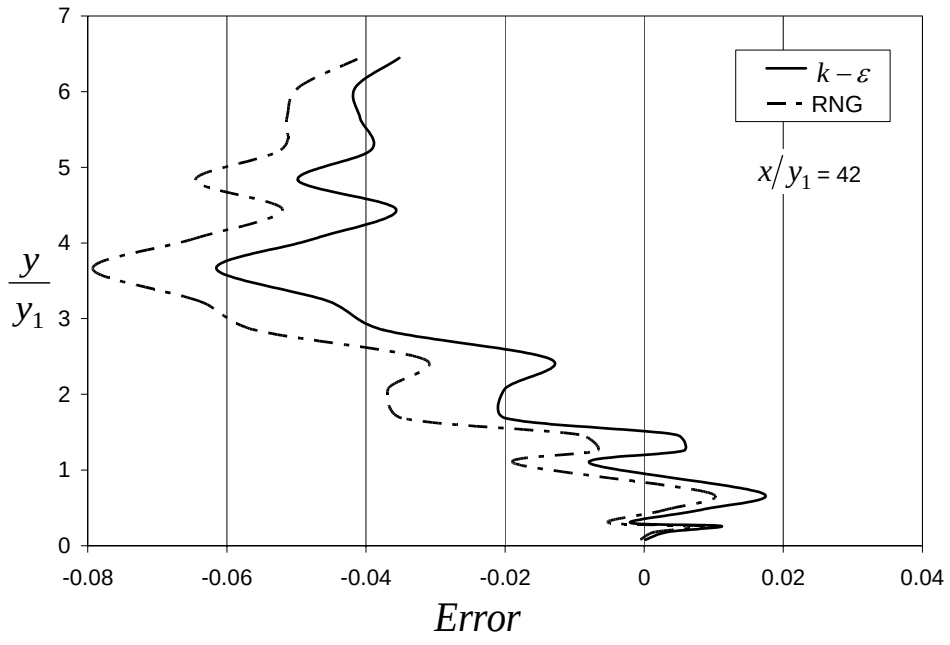

Error Plot of Vertical Velocity for Test 1

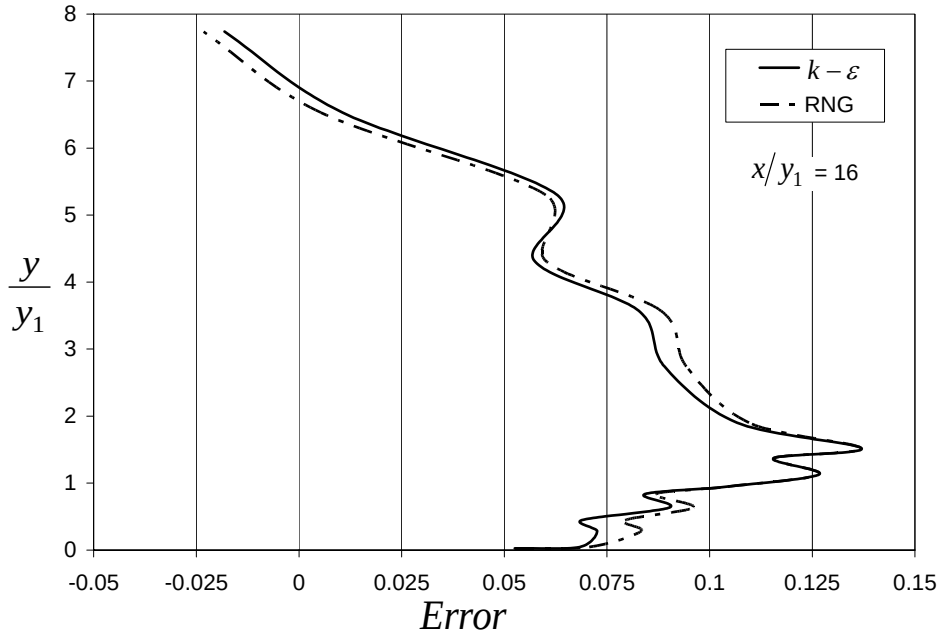

Error Plot of Vertical Velocity for Test 2

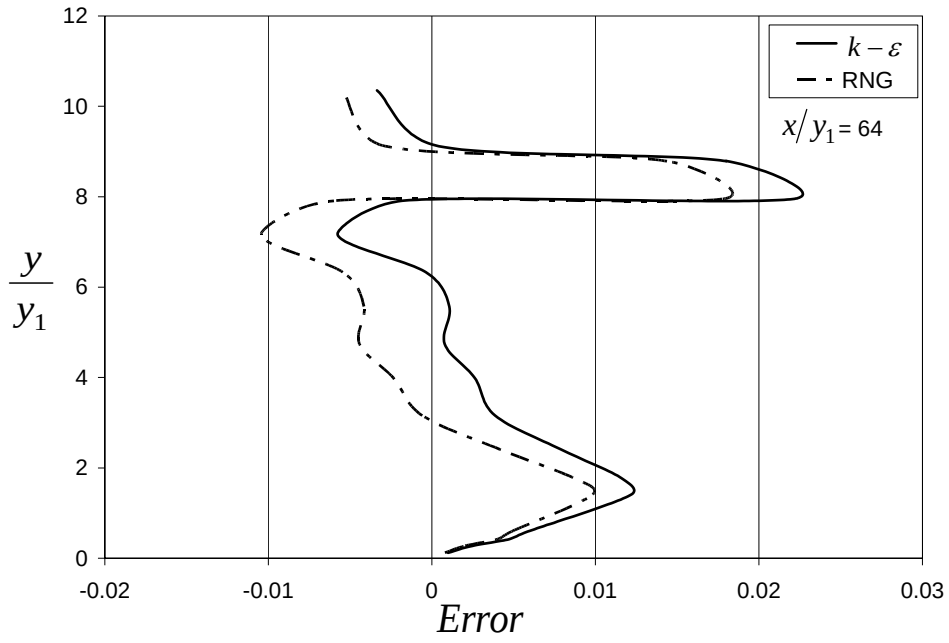

Error Plot of Vertical Velocity for Test 2

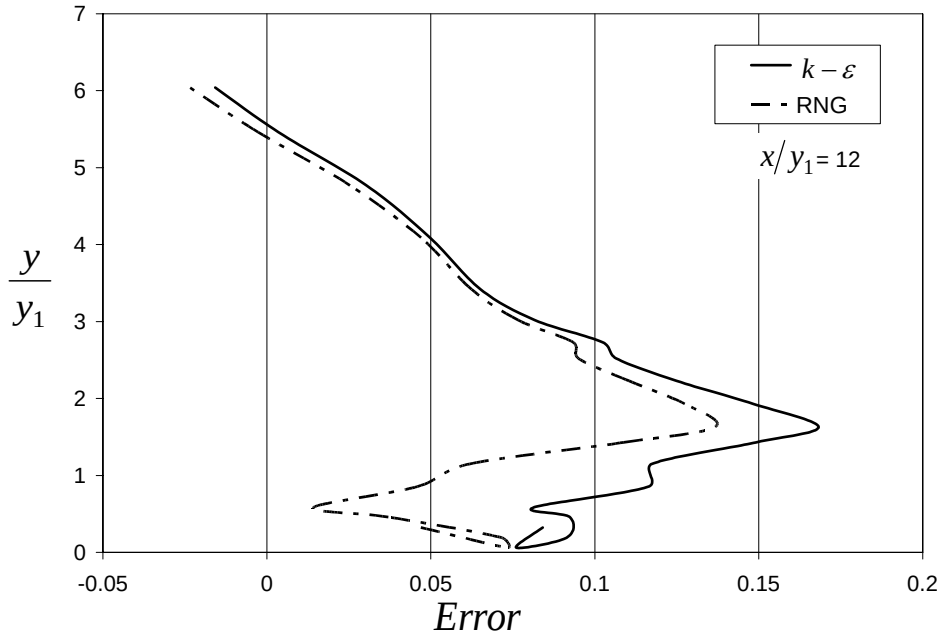

Error Plot of Vertical Velocity for Test 3

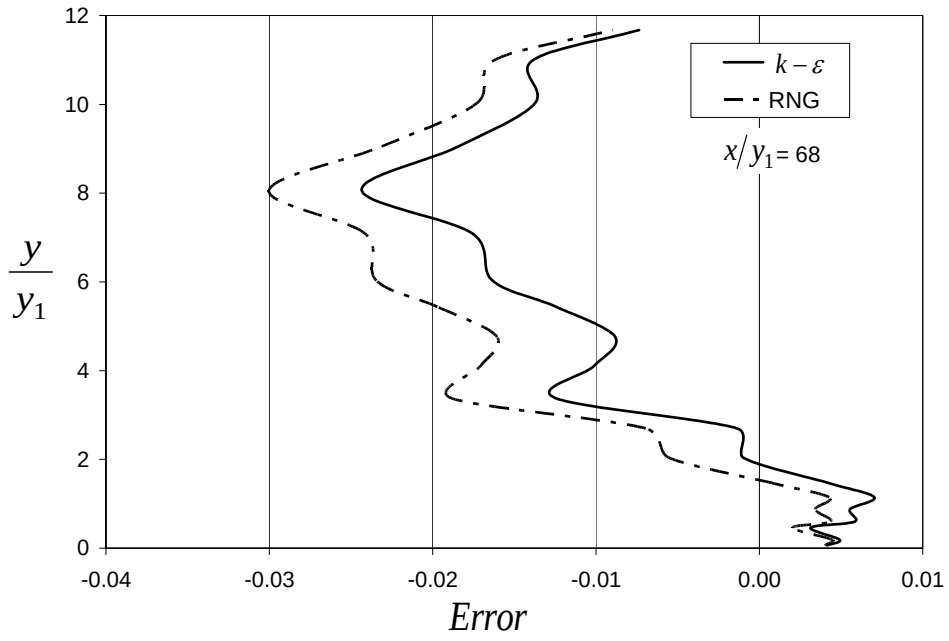

Error Plot of Vertical Velocity for Test 3

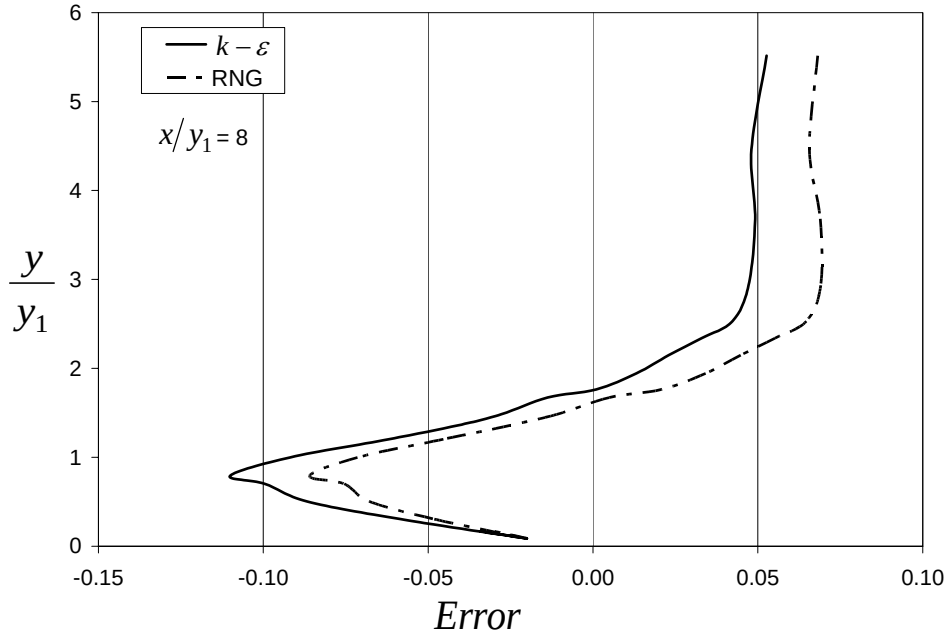

Error Plot of Turbulent Kinetic Energy for Test 1

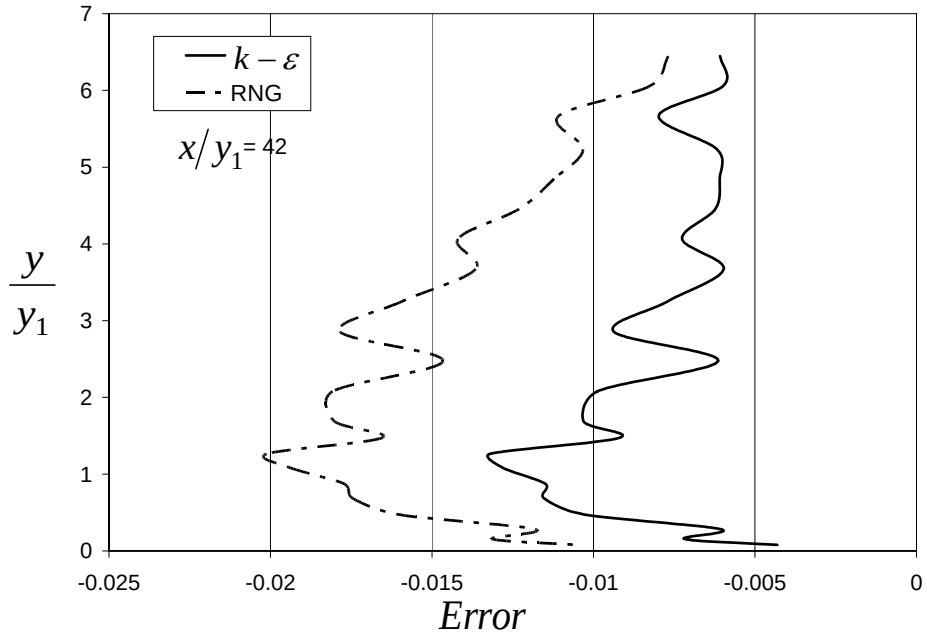

Error Plot of Turbulent Kinetic Energy for Test 1

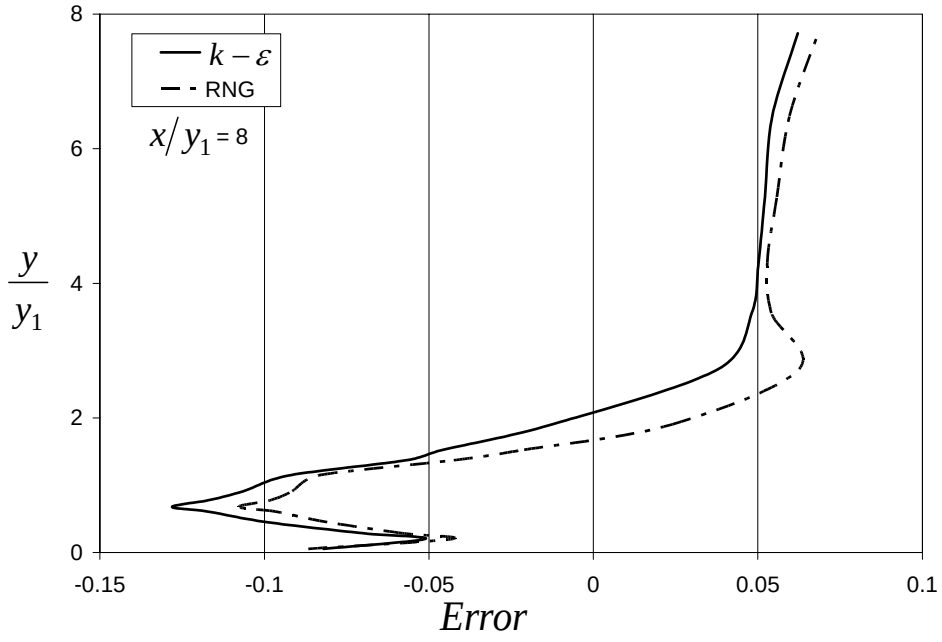

Error Plot of Turbulent Kinetic Energy for Test 2

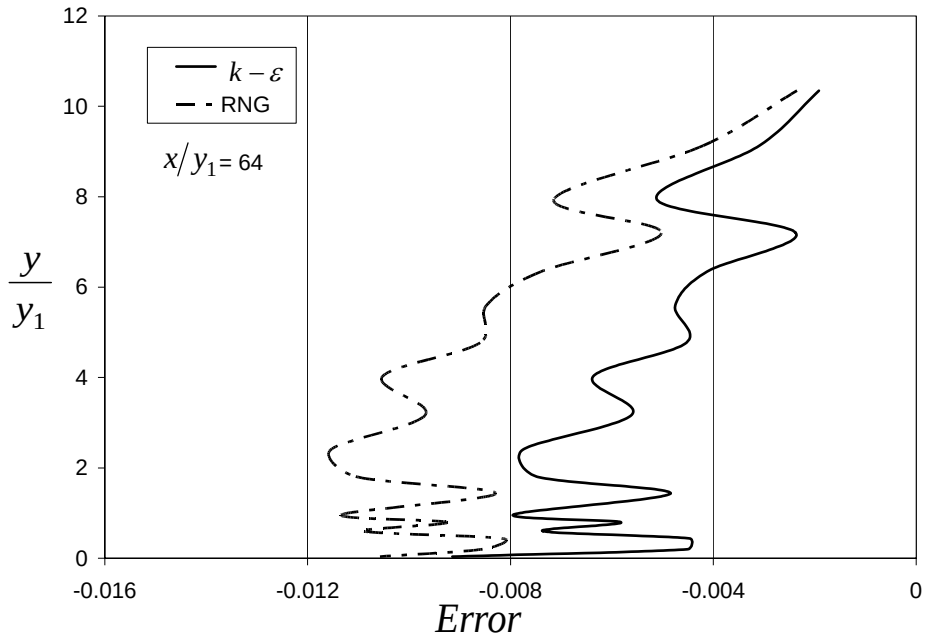

Error Plot of Turbulent Kinetic Energy for Test 2

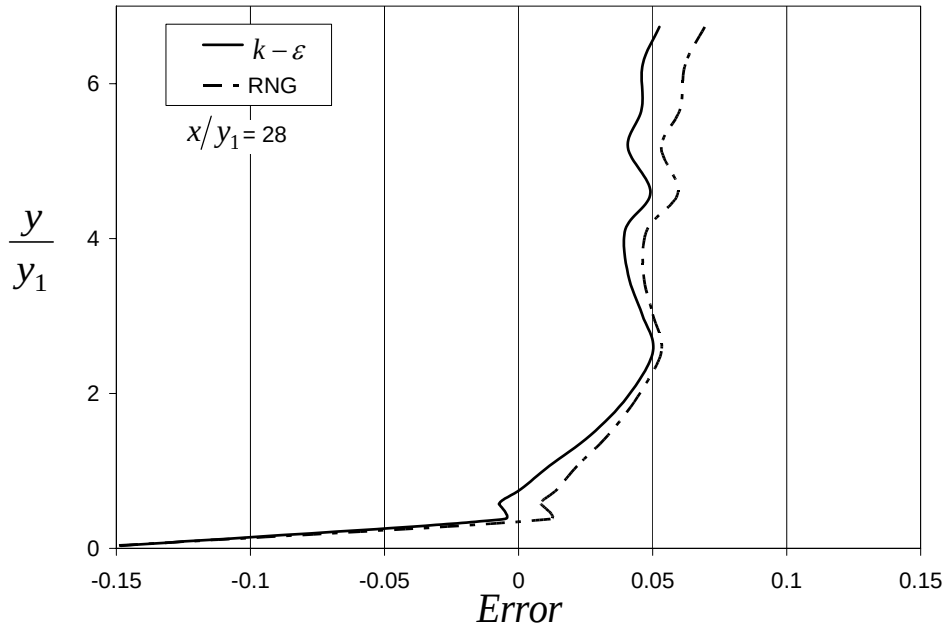

Error Plot of Turbulent Kinetic Energy for Test 3

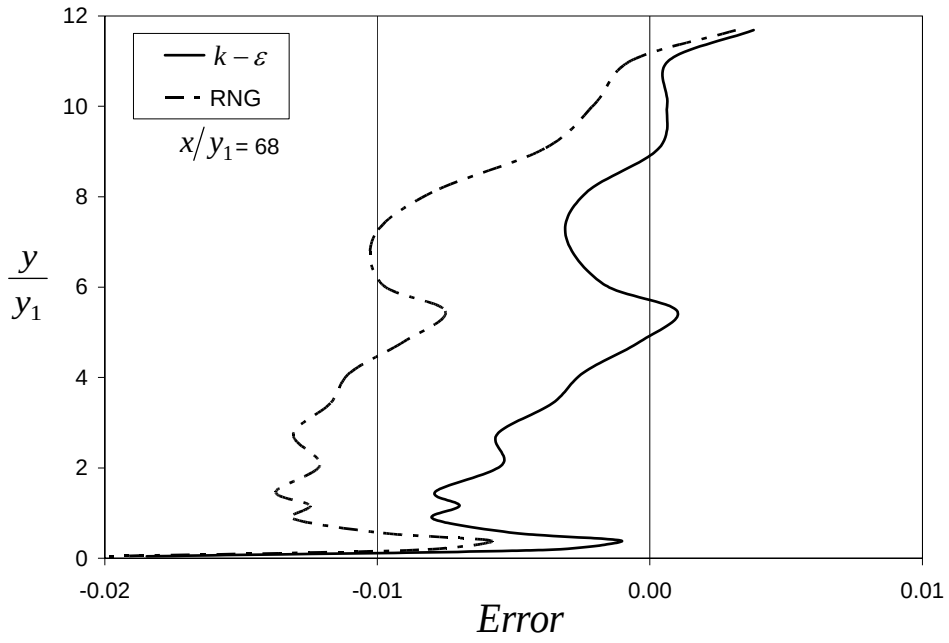

Error Plot of Turbulent Kinetic Energy for Test 3

Appendix F

Computational Mesh

Diagrams of the computational mesh geometries used in the numerical simulations of this research are given below.

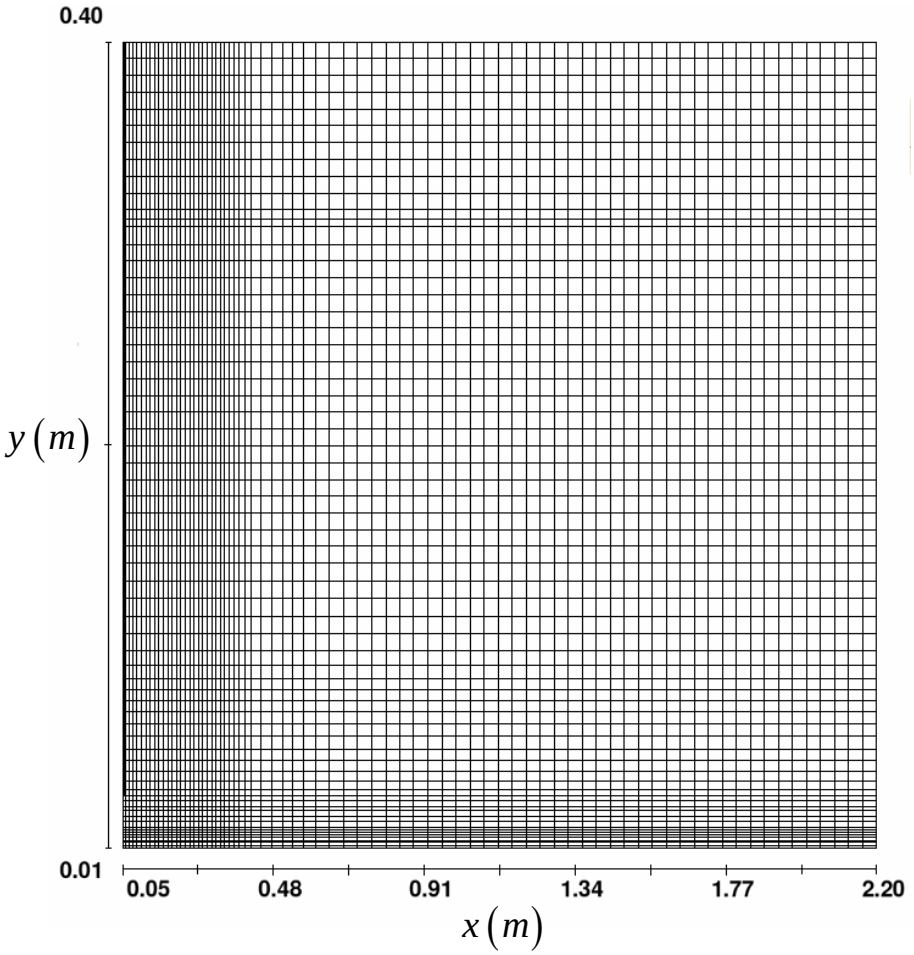

Computational Mesh for Submerged Hydraulic Jump

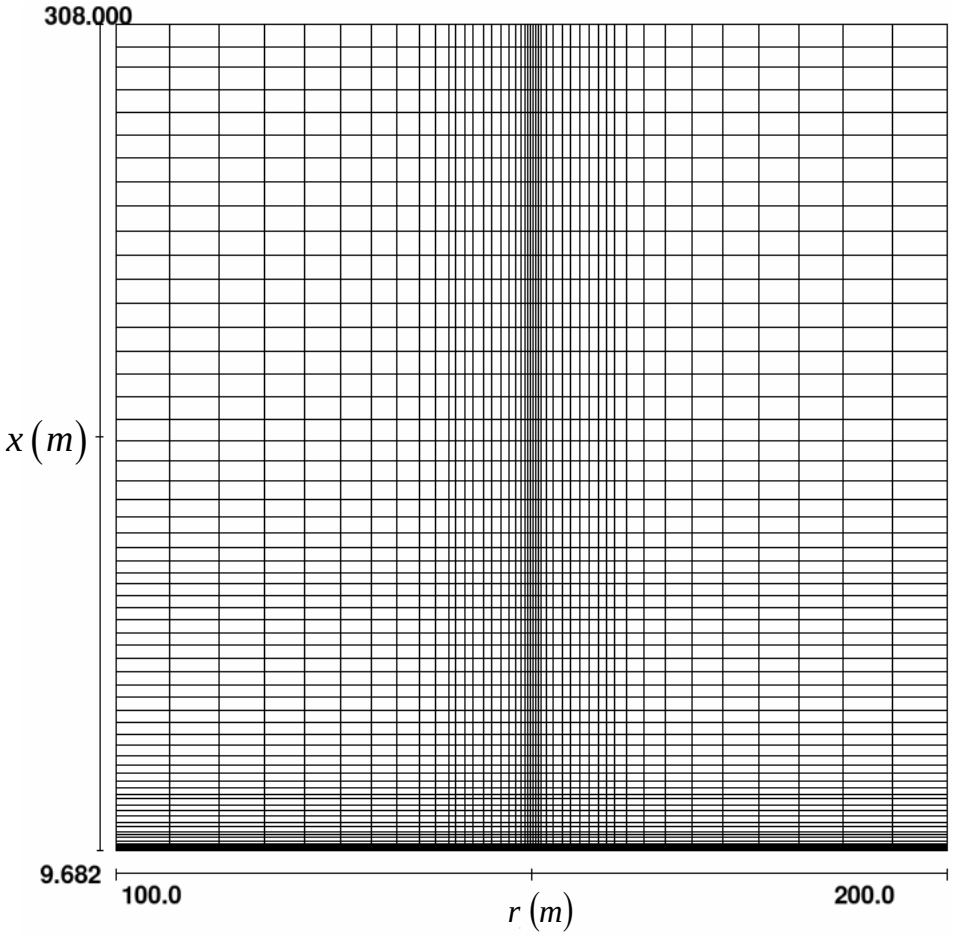

Computational Mesh for Circular Turbulent Jets

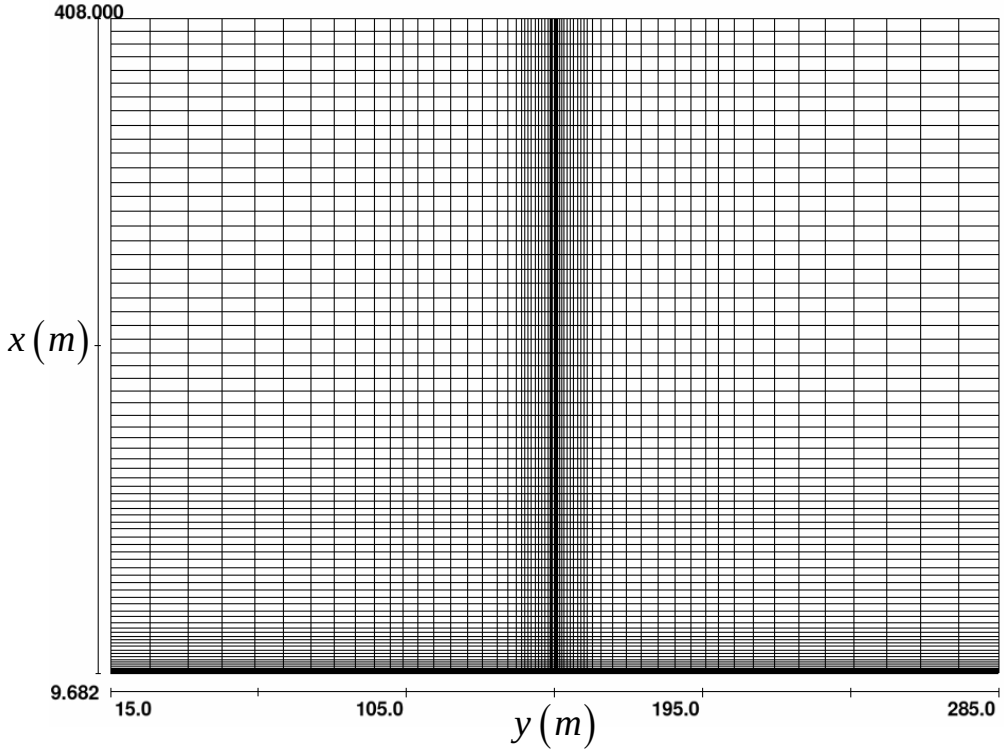

Computational Mesh for Circular Turbulent Jets

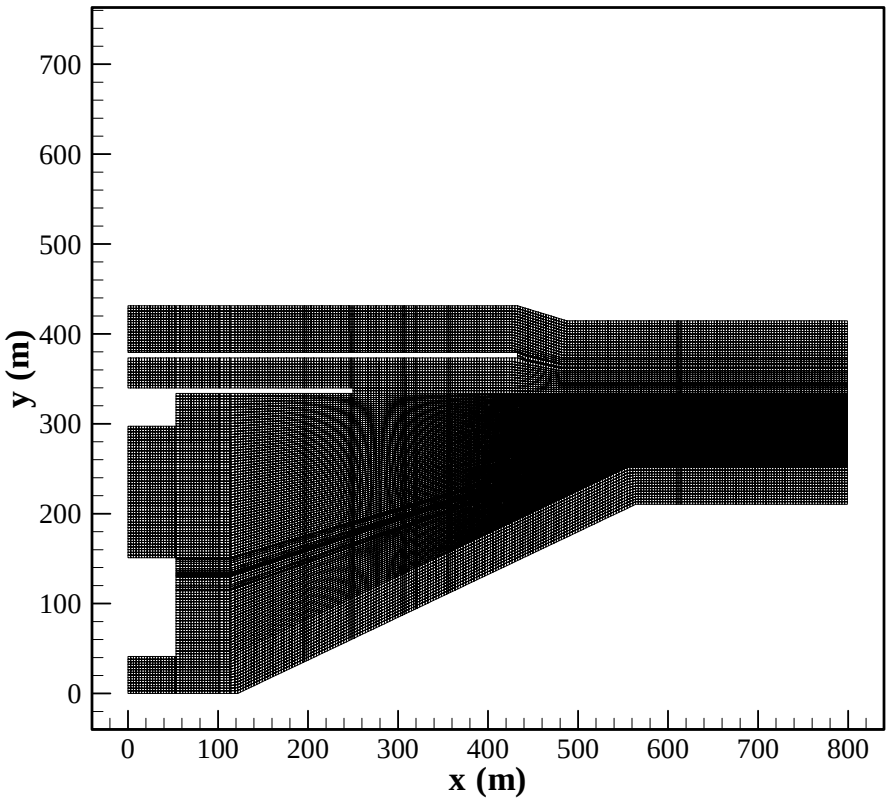

Computational Mesh for Lock and Dam

REFERENCES

A.S.C.E. Task Committee on Turbulence Models in Hydraulic Computations (1988). "Turbulence Modeling of Surface Water Flow and Transport." Journal of Hydraulic Engineering, Vol. 14, No. 9, 969-1152.

Abrahamsson, H., Johansson, B., and Löfdahl, L. (1997). "The Turbulence Field of a Fully Developed Three-dimensional Wall Jet." Internal Rep. No. 9/1, Department of Thermo and Fluid Dynamics, Chalmers Univ. of Technology, Göteborg, Sweden.

Abramovich, G. N. (1963). The Theory of Turbulent Jets. M.I.T. Press (English Translation), Massachusetts, 671 pp.

Albertson, M. L., Dai, Y. B., Jensen, R. A. and Rouse, H. (1950). "Diffusion of Submerged Jets," Trans. ASCE, 115, pp. 639-697.

Anthony, D. G., and Willmarth, W. W. (1992). "Turbulence Measurements in a Round Jet beneath a Free Surface." J. Fluid Mech., 243, pp. 699-720.

Bischof, C. H., Bucker, H. M., and Rasch, A. (2004). "Sensitivity Analysis of Turbulence Models Using Automatic Differentiation." J. Sci. Comput., Vol. 26, No. 2, 510-522.

Bravo, H. R. (1989). "Flow Fields in Navigation Installations Induced by Hydropower Releases," Ph.D. Thesis, University of Iowa, Iowa City, Iowa, p 160.

Bravo, H. R., and Holly, F. M. (1996). "Turbulence Model for Depth-Averaged Flows in Navigation Installation," Journal of Hydraulic Engineering, ASCE, Vol. 122, No. 12, 718-727.

Davis, M. R., Winarto, H. (1980). "Jet Diffusion from a Circular Nozzle above a Solid Plane. J. Fluid Mech., .Vol. 101, Part 1, 201-221.

Ead, S. A. and Rajaratnam, N. (2002). "Plane Turbulent Wall Jets in Shallow Tailwater." J. Engr. Mech., Vol. 128, No. 2, 143-155. Gunal, M., and

Narayanan, R. (1998). "$k-\varepsilon$ Turbulence Modeling of Submerged Hydraulic Jumps using Boundary-Fitted Coordinates," Proc. Instn Civ. Engrs Wat., Marit. & Energy, 130, 104-114.

Heskestad, G. (1965). "Hot-wire Measurements in a Plane Turbulent Jet." Trans. A.S.M.E., J. Appl. Mech., 1-14.

Jia, Y., and Wang, S. S. Y. (1999). "Numerical Model for Channel Flow and Morphological Change Studies," Journal of Hydraulic Engineering, ASCE, Vol. 125, No. 9, 924-933.

Johnston, A. J. (1985), "Aspects of Buoyant and Non-buoyant Jets Entering Shallow Tailwaters." Proc. Intl. Assoc. for Hydraulic Research, 21st Congress, Melbourne, Australia.

Johnston, A. J. and Halliwell, A. R. (1986). "Jet Behavior in Shallow Receiving Water." Proc. Instn Civ. Engrs, Part 2, 81, 549-568.

Johnston, A. J. and Volker, R. E. (1993). "Round Buoyant Jet Entering Shallow Water." J. of Hydr. Res., Vol. 32, No. 1, 121-138.

Khan, A. A., and Wang, S. S. Y. (2001). "Application of CCHE2D Model to Flow Simulation in Lock and Dam," *Proceedings of the 7th Federal Interagency Sedimentation Conference*, Reno, Nevada.

Law, W-K., and Herlina (2002). "An Experimental Study on Turbulent Circular Wall Jets." Journal of Hydraulic Engineering, ASCE, Vol. 120, No. 2, 161-174.

Long, D. (1991). "An Experimental Investigation and $k-\varepsilon$ Turbulence Modeling of Submerged Hydraulic Jumps," Dept. of Civil Engineering, University of Alberta, Edmonton.

Madnia, C. K., and Bernal, L. P. (1994). "Interaction of a Turbulent Round Jet with the Free Surface." J. Fluid Mech., 261, 305-332.

Madsen, P. A., and Svendsen, I. A. (1983). "Turbulent Bores and Hydraulic Jumps," J. Fluid Mechanics, 129, 1-25.

Miller, D. R. and Comings, E. W. (1957). "Static Pressure Distribution in the Free Turbulent Jet." J. Fluid Mech., Vol. 3, 1-16.

Padmanabham, G., and Gowda, B. (1991). "Mean and Turbulence Characteristics of a Class of Three-Dimensional Wall Jets – Part 2: Turbulence Characteristics," Journal of Fluids Engineering, Vol. 113, 629-634.

Rajaratnam, N. (1965). "The Hydraulic Jump as a Wall Jet," Journal of the Hydraulic Division, ASCE, 91(5), 107-132.

Rajaratnam, N. and Humphries, J. A., (1984). “Turbulent Non-Bouyant Surface Jets.” J. Hydr. Res., Vol. 22, No. 2, 103-115.

Rajaratnam, N., and Pani, B. (1974). “Three-Dimensional Turbulent Wall Jets.” Journal of Hydraulic Engineering, *ASCE*, Vol. 100, No. HY1, 69-82.

Rajaratnum, N. (1976). Turbulent Jets. Elsevier Scientific, New York, 304 pp.

Rodi, W. (1984). “Turbulence Models and Their Application in Hydraulics,” IAHR Monograph.

Rodriguez, J. F., Bombardelli, F. A., Garcia, M. H., Frothingham, K. M., Thoads, B. L., and Abad, J. D. (2003). “High-resolution Numerical Simulation of Flow Through a Highly Sinuous River Reach,” Water Resources Management, 18, 177-199.

Rodriguez, J. F., Bombardelli, F. A., Garcia, M. H., Frothingham, K. M., Thoads, B. L., and Abad, J. D. (2003). “High-resolution Numerical Simulation of Flow Through a Highly Sinuous River Reach.” Water Resources Management, 18, 177-199.

Rouse, J., Siao, T. T. and Nagaratnam, R. (1958). “Turbulence Characteristics of the Hydraulic Jump,” Journal of the Hydraulics Division, ASCE, 84(1), Pro. Paper 1528, 1-30.

Schneider, W. (1985), “Decay of Momentum Flux in Submerged Jets,” J. Fluid Mech., Vol. 154, pp. 91-110.

Swean, T. F., Ramberg, S. E., Plesniak, M. W. and Stewart, M. B. (1989). “Turbulent Surface Jet in Channel of Limited Depth.” J. Hydr. Engr., Vol. 115, No. 12, 1587-1606.

Tachie, M. F., and Balachandar, R. (2004). “Roughness Effects on Turbulent Plane Wall Jets in an Open Channel.” Experiments in Fluids, Vol. 37, 281-292.

Wang, S. S. Y., and Hu, K. K. (1992). “Improved Methodology for Formulating Finite-Element Hydrodynamic Models,” Finite Element in Fluids, T. J. Cheng, Edition, Vol. 8, Hemisphere Publishing Corp., 457-478.

Wu, S. and Rajaratnam, N. (1990). “Circular Turbulent Wall Jets on Rough Boundaries.” J. Hydr. Res., Vol. 28, No. 5, 581-589.

Wygnanski, I. and Fiedler, H. (1969). “Some Measurements in the Self-preserving Jet.” J. Fluid Mech., 38, 577-612.